Non-Perturbative Studies of QCD at Small Quark Masses

Dissertation
zur Erlangung des Doktorgrades
des Departments Physik
der Universität Hamburg

vorgelegt von
Jan Wennekers
aus Münster

Hamburg
2006

Gutachter der Dissertation:	Prof. Dr. Hartmut Wittig, Prof. Dr. Joachim Bartels
Gutachter der Disputation:	Prof. Dr. Hartmut Wittig, Prof. Dr. Bernd Kniehl
Datum der Disputation:	27. Juni 2006
Vorsitzender der Prüfungsausschusses:	Prof. Dr. Caren Hagner
Vorsitzender der Promotionsausschusses:	Prof. Dr. Günter Huber
MIN-Dekan:	Prof. Dr. Arno Frühwald

Non-Perturbative Studies of QCD at Small Quark Masses

We investigate the quenched approximation of lattice QCD with numerical simulations of Ginsparg-Wilson fermions, which are a fermion discretisation with exact chiral symmetry. We compute the renormalisation constant of the scalar density, which allows to extrapolate the chiral condensate to the continuum limit. Furthermore we match lattice results of matrix elements describing hadronic kaon decays to Chiral Perturbation Theory in finite volume and at almost vanishing quark mass. The resulting low-energy constants in the considered SU(4)-flavour symmetric case indicate a substantial contribution of low scale QCD effects to the $\Delta I = 1/2$ rule.

Nichtperturbative Untersuchungen der QCD bei kleinen Quarkmassen

Wir untersuchen die Valenzquarknäherung der Gitter-QCD mit numerischen Simulationen von Ginsparg-Wilson Fermionen, die eine Fermiondiskretisierung mit exakter chiraler Symmetrie darstellen. Wir berechnen den Renormierungsfaktor der skalaren Dichte für mehrere Gitterabstände, was eine Extrapolation des chiralen Kondensats zum Kontinuumslimes erlaubt. Weiterhin vergleichen wir Gitterresultate für Matrixelemente, die hadronische Kaonzerfälle beschreiben, mit chiraler Störungstheorie in endlichem Volumen und bei fast verschwindender Quarkmasse. Die resultierenden Niederenergiekonstanten im betrachteten SU(4)-Flavour-symmetrischen Fall deuten auf einen erheblichen Beitrag zur $\Delta I = 1/2$-Regel von QCD-Effekten an einer niedrigen Skala hin.

Contents

Contents

1 Introduction

Today's understanding of the fundamental forces of nature is gathered in the *Standard Model* (SM) which incorporates the strong and electroweak interactions but not gravity. Despite the clear evidence of new physics beyond the SM such as neutrino oscillations and non-baryonic dark matter, little doubt remains that *Quantum Chromodynamics* (QCD), which is one pillar of the SM, really describes the strong interaction. QCD is a quantum field theory which couples N_f flavours of fermions ψ_f — called *quarks* — to a non-Abelian SU(3) gauge theory. In this context, *colour* is the charge of the quarks to which the *gluons* (gauge fields A_μ^a) couple. The QCD Lagrangian, here written in its Euclidean version, is remarkably simple,

$$\mathcal{L}_\mathrm{QCD} = \sum_{f=1}^{N_\mathrm{f}} \overline{\psi}_f \left(\gamma_\mu D_\mu + m_f\right) \psi_f - \frac{1}{2} F_{\mu\nu}^a F_{\mu\nu}^a. \tag{1.1}$$

The covariant derivative is defined as $D_\mu = \partial_\mu - \mathrm{i} g_0 A_\mu^a T^a$, where T^a are the generators of SU(3) with $\mathrm{Tr}\, T^a T^b = \frac{1}{2}\delta^{ab}$ and $[T^a, T^b] = \mathrm{i} f^{abc} T^c$. For the field strength this convention implies $F_{\mu\nu}^a = \partial_\mu A_\nu^a - \partial_\nu A_\mu^a + g_0 f^{abc} A_\mu^b A_\nu^c$.

Perturbative QCD is very successful in explaining the outcome of high-energy experiments. Some of the more prominent examples are the running of the strong coupling and scaling violations at small Bjorken-x. At high energies the theory exhibits *asymptotic freedom*, which means that quarks and gluons become quasi-free particles. Different from the electroweak sector of the SM the perturbative treatment of QCD fails at low energy scales. The observation that only colour-neutral particles exist in nature[1] is called *confinement*. The fundamental degrees of freedom form bound states called *hadrons*. Together with the steeply rising gauge coupling this makes a *non-perturbative* approach unavoidable.

The *lattice* offers a fully non-perturbative regularisation of quantum field theories. The main idea is to approximate the Euclidean path integral by restricting spacetime to a finite lattice of points [1]. An introduction to the basic concepts of lattice QCD is given in Chapter 2. In the regularised theory it is possible to renormalise observables without referring to perturbation theory. Therefore the approach allows to "understand" quantum field theories in a new way. An example for a completely analytical result in lattice field theory is the proof of *triviality bounds* for ϕ^4-theory by Lüscher and Weisz [2].

To a large extent the impact of lattice results on particle phenomenology is due to computer simulations. The discretised version of the theory can be evaluated with Monte Carlo methods [3]. The sketch of a stereotypical lattice QCD simulation is shown in Figure 1.1. One fixes the

[1] At least below the QCD phase transition and the top quark mass.

bare parameters in the Lagrangian with input from, for instance pseudoscalar meson masses. After the computation one obtains results for several physical quantities like particle masses and decay constants.

$$\begin{array}{ccccc} \text{input} & & \text{simulation} & & \text{results} \\ & & & & m_q \\ m_\pi & \Rightarrow & \left\{ \mathcal{L}(g_0, m_f) \right\} & \Rightarrow & F_\pi,\, F_K \\ m_K & & & & n_N \\ & & & & \Lambda_{\text{QCD}} \end{array}$$

Figure 1.1: Possible input parameters and results of a lattice QCD simulation.

The performance of lattice QCD programs has improved enormously through new and better algorithms and the development of larger and faster computers.

The biggest conceptual development in lattice QCD over the last decade has been the construction of chiral fermions in the regularised theory. This came as a surprise, as it was believed that fermion discretisations were incompatible with chiral symmetry since the work of Nielsen and Ninomiya in 1981 [4]. Today regularisations which circumvent the no-go theorem go under the name of *Ginsparg-Wilson fermions* [5].

The use of Ginsparg-Wilson fermions in simulations is very demanding compared to more conventional lattice fermions. Therefore they are most useful in parameter regimes where other approaches fail and the exact chiral symmetry simplifies the computation significantly. In this work two advantages of chiral lattice fermions are exploited. In principle it is possible to simulate Ginsparg-Wilson fermions at arbitrarily small quark masses. Of course one is limited through practical considerations, but still one has the opportunity to go directly to the chiral limit. The other important aspect of the preserved chiral symmetry is the possibility to match directly to Chiral Perturbation Theory (ChPT). ChPT is an effective field theory which describes low-energy QCD in terms of meson fields. A special corner of parameter space where the matching can be performed is the *ϵ-regime* of QCD. The quark mass in this regime is very small while the volume is kept constant. The pions cannot propagate in this situation. For the effective description in CHPT this means that the path integral is dominated by zero-momentum modes. Even though the ϵ-regime is rather artificial, it is possible to extract physical information via a matching of ChPT to lattice QCD in a small volume. The low-energy constants — free parameters in ChPT — which result from the matching are the same as in infinite volume. The interplay of lattice QCD and ChPT is a main topic in this work.

The thesis is organised as follows. Chapter 2 contains a short introduction to lattice QCD with an emphasis on Ginsparg-Wilson fermions. Chapter 3 covers the basic concepts of Chiral Perturbation Theory. Then the ϵ-regime of QCD, which is reached in the limit of vanishing quark mass at fixed volume, is introduced and its description in Chiral Perturbation Theory is given. In Chapter 4 we summarise the numerical techniques to deal with the Dirac operator in the chosen discretisation. Here the main novelty is the use if the *generalised minimal residual* algorithm, an inversion algorithm and *low mode preconditioning*, a method to reduce

the slowing down of the inversion of the Dirac operator for small quark masses. In Chapter 5 a non-perturbative computation of the renormalisation constant of the scalar density is described, which allows a continuum extrapolation of the chiral condensate, the low-energy constant which signals spontaneous chiral symmetry breaking. Further scaling tests for the pseudoscalar decay constant and the vector meson mass show that Ginsparg-Wilson fermions have very small lattice artefacts. The next project in Chapter 6 is a study on non-leptonic kaon decays in the ϵ-regime. Here the numerical results for $K \to \pi$ matrix elements are matched to Chiral Perturbation Theory. Then the resulting low-energy constants are related to the physical $K \to \pi\pi$ decays. The aim is to disentangle several possible contributions to the $\Delta I = 1/2$ rule which states that the decay into the isospin zero state for the two pions is preferred over the decay into the isospin two state. First results indicate a large contribution from QCD effects at a low scale. The Chapter 7 is a brief account of recent work on correlators saturated with fermionic zero modes. The idea is to match correlators which diverge in the chiral limit to Chiral Perturbation Theory and thereby obtain estimates for the occurring low-energy constant with a method that has completely different systematic uncertainties. The last chapter contains concluding remarks and speculation about possible future developments.

2 Lattice QCD with Ginsparg-Wilson Fermions

In this chapter a short introduction to lattice QCD is given. In the first section the idea of lattice regularisation is introduced. The second section deals with the discretisation of the gauge field and the third one with fermions on the lattice. The fourth section contains a brief review of discretisations preserving chiral symmetry. The last section deals with the so called *quenched approximation*.

2.1 General Remarks

The idea of regularising a Euclidean quantum field theory — and specifically QCD — with a lattice was proposed by Wilson in 1974 [1]. Space-time is approximated by a hypercubical grid Γ of points with separation a,

$$\Gamma \equiv \Big\{ x \in a \cdot \mathbb{Z}^4 \Big| x_\mu = 0, a, \ldots, (N_\mu - 1)a \Big\}. \tag{2.1}$$

The fermionic (or scalar) fields "live" only on these points. Their behaviour under a gauge transformation $\Lambda(x)$ is equivalent to the one in the continuous theory,

$$\psi(x) \to \Lambda(x)\psi(x), \quad \overline{\psi}(x) \to \overline{\psi}(x)\Lambda^{-1}(x). \tag{2.2}$$

The gauge fields are parameterised by so called *link variables* U_μ which connect neighbouring points. They are elements of the Lie group — SU(3) in the case of QCD — and transform as

$$U_\mu(x) \to \Lambda(x) U_\mu(x) \Lambda^{-1}(x + \hat{\mu}). \tag{2.3}$$

The link variable can be seen as *parallel transporters* from x to $x + \hat{\mu}$. For a given continuum gauge field A_μ^b the link variable

$$U_\mu = \exp\left(\mathrm{i} g a T^b A_\mu^b \right), \tag{2.4}$$

reproduces the gauge field on the lattice up to higher orders in the lattice spacing. The gauge field A_μ cannot be used directly on the lattice since its gauge transformation cannot be formulated consistently with a discretised derivative.

Since the lattice is finite by definition it is necessary to impose boundary conditions. Often they are chosen to be periodic, but there are several alternatives. The restriction of the theory on a lattice introduces a momentum cut-off in analogy to the spectrum of vibrations in a finite crystal. The possible values of lattice momenta are

$$p_\mu = 2\pi \frac{n_\mu}{L_\mu}, \quad \text{with} \quad n_\mu = 1, \ldots, N_\mu - 1, \quad L_\mu = a N_\mu, \tag{2.5}$$

where L_μ is the linear extension in μ-direction. The interval for the first *Brillouin zone* can of course also be chosen symmetrically from $-\pi/L_\mu$ to π/L_μ. The cut-off is inversely proportional to the lattice spacing. It is also necessary to define a *lattice derivative* which takes the minimal length a into account. The *forward* and *backward* covariant lattice derivatives are defined as,

$$\nabla_\mu \psi(x) \equiv \frac{1}{a}\big[U_\mu(x)\psi(x+\hat{\mu}) - \psi(x)\big], \tag{2.6a}$$

$$\nabla^*_\mu \psi(x) \equiv \frac{1}{a}\big[\psi(x) - U^\dagger_\mu(x-\hat{\mu})\psi(x-\hat{\mu})\big], \tag{2.6b}$$

where $\hat{\mu}$ is a vector of length a in direction μ.

The lattice regularisation is the only known, non-perturbative way to regularise quantum field theories. Its substantial impact also on particle phenomenology is mainly founded on the use of computer simulations. The lattice is quite obviously the right choice to be put on a computer. The discretised theory has only a finite number of degrees of freedom and in the Euclidean the term e^{-S} is the analogue of the Boltzmann factor in statistical mechanics where numerical methods are also widely used.

Observables in a lattice simulation are defined like in any quantum field theory as expectation values of operators. Such an expectation value in the regularised theory is given by

$$\langle \mathcal{O} \rangle = \frac{1}{Z} \int \sum_f \big[\mathrm{d}U \mathrm{d}\overline{\psi}_f \mathrm{d}\psi_f\big]\, \mathcal{O} \exp\Big\{-\Big(S_\mathrm{g}\big[U\big] + S_\mathrm{f}\left[U, \overline{\psi}_f, \psi_f\right]\Big)\Big\}, \tag{2.7}$$

with the partition function

$$Z = \int \sum_f \big[\mathrm{d}U \mathrm{d}\overline{\psi}_f \mathrm{d}\psi_f\big] \exp\Big\{-\Big(S_\mathrm{g}\big[U\big] + S_\mathrm{f}\left[U, \overline{\psi}_f, \psi_f\right]\Big)\Big\}. \tag{2.8}$$

The fermionic variables can be integrated out formally,

$$Z = \int \big[\mathrm{d}U\big] \prod_f \left(\det Q_f[U]\right) \exp\Big\{-S_\mathrm{g}\big[U\big]\Big\}, \tag{2.9}$$

where Q is called the *fermion matrix*. The determinant is then absorbed into an effective action,

$$Z = \int \big[\mathrm{d}U\big] \exp\Big\{-S_\mathrm{eff}\big[U\big]\Big\}, \quad S_\mathrm{eff} \equiv S_\mathrm{g} - \ln\left(\prod_f \det Q_f\right). \tag{2.10}$$

In order to obtain a numerical result the path integral is approximated using a finite number ($\mathrm{O}(100-1000)$) of representatives of the gauge field usually called configurations. They are generated with Monte Carlo algorithms, for details see Appendix A.1.

2.2 Wilson Gauge Action

A possible lattice gauge action must reproduce the Euclidean version of the Yang-Mills action in the *continuum limit*, $a \to 0$. By building the action from closed curves, gauge invariance is

automatically ensured. The simplest choice is the *Wilson gauge action* [1],

$$S_{\mathrm{g}}[U] = \beta \sum_{x} \sum_{\substack{\mu,\nu=0 \\ \mu<\nu}}^{3} \left(1 - \frac{1}{3} \operatorname{Re}\, \operatorname{Tr} U_{\mu\nu}(x)\right), \tag{2.11}$$

which is also called *plaquette action* as the basic building block is the plaquette,

$$U_{\mu\nu}(x) \equiv U_{\mu}(x) U_{\nu}(x+\hat{\mu}) U_{\mu}^{\dagger}(x+\hat{\nu}) U_{\nu}^{\dagger}(x), \tag{2.12}$$

the smallest lattice Wilson loop. It reproduces the Yang-Mills action in the limit $a \to 0$ if the parameter β is chosen as

$$\beta = \frac{2N}{g_0^2}, \tag{2.13}$$

for SU(N) gauge theory with bare coupling g_0.

Since only the continuum limit of the action is fixed, it is possible to add further terms to the action which come with higher powers of the lattice spacing a. Several of these *improved gauge actions* are used today [6–8]. The main reason for this is to reduce lattice artefacts. They are also used to improve algorithms on the fermionic side of the calculation. Here the gauge field enters via the covariant derivative (2.6). It is generally believed that simulations with improved gauge actions lead to "smoother" gauge fields. That means the behaviour is closer to the estimate in lattice perturbation theory. But is is also seen in several computations that the distribution of the topological charge can be influenced by the higher terms in the gauge action. In our numerical studies always the Wilson gauge action (2.11) is used.

2.3 Fermions and Species Doubling

Discretising the fermionic part of the action in a naïve way leads to the unwanted phenomenon of *fermion doubling*. The pole of the fermion propagator defines the mass of the quark. But on the lattice one gets a pole for every corner of the Brillouin zone, i.e. $k_\mu = 0, 2\pi$. That means there are sixteen mass degenerate quarks in this formulation. The number of flavours is doubled for every space-time dimension. Considering the free fermion propagator in momentum space, one can see the doublers explicitly,

$$S(k)^{-1} = \sum_{\mu=0}^{3} \mathrm{i}\gamma_\mu s_\mu + m, \tag{2.14}$$

$$S(k) = \frac{m - \mathrm{i}\sum_{\mu=0}^{3} \gamma_\mu s_\mu}{m^2 + s^2}, \tag{2.15}$$

where $s_\mu \equiv \sin k_\mu$. The multiple poles arise from the periodicity of the sine.

The first solution[1] of the doubling problem was to introduce an additional term in the action which gives the doublers a mass which goes to infinity when approaching the continuum limit.

[1] Again it was Wilson's idea [9].

They decouple from the physical spectrum and only the fermion with $k_\mu = 0, ; \mu = 0 - 3$ survives. The resulting fermion action for one flavour reads,

$$S_{\mathrm{f}}[U, \overline{\psi}, \psi] = \sum_{x,y} \overline{\psi}(y) Q(y, x; U) \psi(x), \tag{2.16}$$

with the fermion matrix Q,

$$Q \equiv \gamma_5 \left(D_{\mathrm{W}} + m_0 \right), \tag{2.17}$$

and the Wilson Dirac operator D_{W},

$$D_{\mathrm{W}} \equiv \frac{1}{2} \left[\gamma_\mu \left(\nabla^*_\mu + \nabla_\mu \right) - ra \nabla^*_\mu \nabla_\mu \right]. \tag{2.18}$$

Inserting the derivatives explicitly leads to

$$\begin{aligned} Q\psi(x) = \frac{1}{2a} \gamma_5 \Bigg\{ (8r + 2m_0)\psi(x) - \sum_{\mu=0}^{3} \Big[& U_\mu(x)(r - \gamma_\mu)\psi(x + \hat{\mu}) \\ & + U^\dagger_\mu(x - \hat{\mu})(r + \gamma_\mu)\psi(x - \hat{\mu}) \Big] \Bigg\}. \end{aligned} \tag{2.19}$$

The parameter r can be tuned from -1 to 1. For $r = 1$ the combination $1 \pm \gamma_\mu$ is a projection on the fermion fields without the doublers. Introducing an explicit term which removes the doublers comes at a price. The quark mass acquires an additive renormalisation. The Wilson term also breaks chiral symmetry. This translates into a violation of the continuum chiral Ward identities [10], which leads to more complicated renormalisation patterns. Nevertheless Wilson fermions are still widely used, because of they are relatively easy to simulate and the mentioned issues pose no unsurmountable obstacles.

The lattice artefacts of Wilson fermions are of order a. It is possible to improve the scaling with a procedure called *Symanzik's improvement programme*. The idea of Symanzik [6] was to treat lattice artefacts with the help of an effective field theory. Then the terms can be cancelled order by order in an iterative procedure. To cancel the leading term for QCD with Wilson fermions it is enough to introduce one further term in the fermion action, the Sheikholeslami-Wohlert term [11]. Also an "improvement" of operators built from quark fields is necessary.

A special case of Wilson fermions are *twisted mass fermions* [12]. Here the $\mathrm{O}(a)$-improvement is reached in an indirect way. The theory consists of a doublet of fermion fields with a chirally rotated mass term. If the *twist angle* is set to $\pi/2$, the relevant observables automatically scale with a^2, [13].

The second "traditional" approach to discretised fermions are *staggered fermions* introduced by Kogut and Susskind in 1975 [14, 15]. The four Dirac components of the fermion field are distributed over a small square of lattice sites. These four points are then identified as one site on a second and coarser lattice. The method has the advantage of an additional discrete symmetry which prevents additive mass renormalisation. However the number of physical flavours always appear in a four-fold degeneracy. To be able to consider two or three light

quarks one uses the so called *fourth root trick* [16]. One identifies the four mass-degenerate *tastes*[2] with one physical flavour and takes the fourth root of the fermion determinant in the effective action (2.10). Large scale simulation with staggered quarks have found no discrepancy with experiment so far, see for example [17]. But there is still doubt about the field theoretical foundation of the fourth root trick [18–21].

2.4 Ginsparg-Wilson Fermions

Already more than twenty years ago Ginsparg and Wilson published a paper with the main ingredient for chiral symmetry on the lattice [5]. The massless Dirac operator in the continuum anticommutes with γ_5. They relaxed this requirement and proposed an additional local term to define a lattice Dirac operator with chiral symmetry. The *Ginsparg-Wilson relation*,

$$\gamma_5 D + D\gamma_5 = aD\gamma_5 D, \tag{2.20}$$

offers a possibility to define chiral symmetry in the discretised theory.

The Nielsen-Ninomiya no-go theorem [4] states that the following four requirements to the Dirac operator cannot be fulfilled at the same time:

- locality, $\|D(x-y)\| < C\,\mathrm{e}^{-\kappa\|x-y\|}$, with κ constant,
- continuum limit goes as $\widehat{D}(p) = \mathrm{i}\gamma_\mu p_\mu + \mathrm{O}\big(ap^2\big)$,
- $\widehat{D}(p)$ is always invertible for $p \neq 0$, hence no doublers,
- chiral symmetry, $\gamma_5 D + D\gamma_5 = 0$.

Wilson fermions fail to be chirally symmetric and staggered fermions still have some kind of doublers. But the notion of chiral symmetry has to be changed on the lattice. By defining an infinitesimal chiral rotation on the lattice as,

$$\delta\tilde{\psi} = \lambda^a \gamma_5 \tilde{\psi}, \qquad\qquad \delta\overline{\psi} = \overline{\psi}\gamma_5 \lambda^a, \tag{2.21}$$

where $\tilde{\psi} = \big(1 - \frac{1}{2}\overline{a}D\big)\,\psi$, it is possible to introduce a lattice version of on infinitesimal chiral rotation and thereby circumvent the no-go theorem [22].

2.4.1 Index Theorem on the Lattice

The definition (2.21) implies a shift in the fermion integration measure which reproduces the flavour-singlet chiral anomaly [22]. The expectation value of an arbitrary product of fermion fields $\mathcal{O}$ is shifted by

$$\langle \delta\mathcal{O} \rangle_{\mathrm{F}} = -a\,\mathrm{Tr}\,[\gamma_5 D]\,\langle \mathcal{O} \rangle_{\mathrm{F}}\,. \tag{2.22}$$

[2] *Taste* is just a name for one of the four mass-degenerate staggered quark flavours.

The correction vanishes for flavour non-singlet chiral rotations for which the generators are traceless, but not the flavour-singlet case. In [23] it has been shown that the trace is equal to the topological charge of the gauge field and that an analogous *index theorem* to the Atiyah-Singer index theorem [24] holds for lattice Dirac operators satisfying the Ginsparg-Wilson relation. The topological charge ν of a background gauge field is determined from the number of fermionic zero modes,

$$\nu = n_+ - n_-. \tag{2.23}$$

Since the zero modes always appear with fixed chirality, one gets $\nu = \pm n_\pm$. Thus the topological charge of a gauge configuration can be determined by just counting the number of these fermionic zero modes.

2.4.2 Neuberger's Operator

Neuberger's explicit construction of an operator satisfying the Ginsparg-Wilson relation allows to treat Ginsparg-Wilson fermions numerically. He found a solution using the *overlap formalism* [25, 26].

In the form used in the following the Neuberger operator reads

$$D = \frac{1}{\overline{a}}\left(1 - \frac{A}{\sqrt{A^\dagger A}}\right), \qquad A = 1 + s - aD_{\mathrm{W}}, \tag{2.24}$$

with a constant $\overline{a}$ which is proportional to the lattice spacing a,

$$\overline{a} = \frac{1}{1+s}a, \quad -1 < s < 1, \tag{2.25}$$

where D_{W} denotes the Wilson-Dirac operator (2.18) and the inverse square root is defined via a power series. The parameter s is tunable from -1 to 1 and allows to improve the locality properties of the operator.

The fact that the overlap operator is a local operator is not as obvious as for the Wilson Dirac operator which acts only on nearest neighbours. In the case of sufficiently smooth gauge fields locality with exponentially decaying tails can be shown analytically [27]. There it was also shown numerically that the range of the operator goes with $\mathrm{e}^{-\kappa r/a}$, where κ is a constant. The mass scale corresponding to the range should not interfere with the physical scales. A way to quantify this was proposed in [28]. There it is found that it might be impossible to define the Neuberger operator on very coarse lattices.

At finite lattice spacing the locality properties of the operator can be optimised by tuning the parameter s introduced in Eq. (2.25) for different bare couplings β. The optimal value at $\beta = 6.0$ was found to be $s = 0.4$ [27], which we will use also at other bare couplings to allow a joint continuum extrapolation.

The spectrum of the overlap operator, as it is also called, is a circle in the complex plane, Figure 2.1. This is a general statement for Ginsparg-Wilson fermions since it follows directly

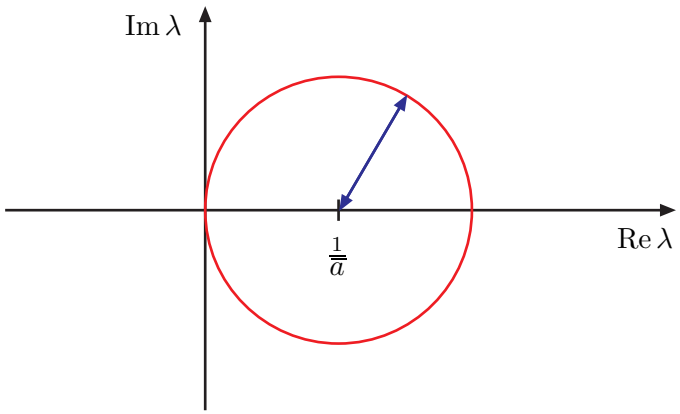

Figure 2.1: The "Ginsparg-Wilson circle" on which the eigenvalue spectrum of the massless Neuberger operator is confined. The radius of the circle is $1/\overline{a}$.

from the Ginsparg-Wilson relation (2.20) and γ_5-hermiticity. For an eigenvector ψ with $D\psi = \lambda\psi$ one gets

$$\left(D^\dagger + D\right)\psi = (\gamma_5 D + D\gamma_5)\,\gamma_5\psi = \overline{a}D\gamma_5 D\gamma_5\psi = \overline{a}DD^\dagger\psi = \overline{a}\lambda\lambda^*\psi, \tag{2.26}$$

and therefore

$$\lambda^* + \lambda = 2\,\mathrm{Re}\,\lambda = \overline{a}|\lambda|^2, \tag{2.27}$$

which defines a circle in the complex plane with origin $(0, 1/\overline{a})$ and radius $1/\overline{a}$. All eigenvalues come in complex conjugated pairs except for the vanishing ones, which are related to the topology of the gauge field.

For the massive operator which is defined as

$$D_m \equiv \left(1 - \frac{1}{2}\overline{a}m\right) D + m, \tag{2.28}$$

the circle is deformed and its centre shifted from $1/\overline{a}$ to $1/\overline{a} + m$. Thereby the smallest eigenvalues also aquire a real part of order m and arbitrarily small eigenvalues which would be responsible for so called *exceptional configurations* cannot occur.

2.4.3 Approximate Ginsparg-Wilson Fermions

It is possible to construct fermionic discretisations which preserve chiral symmetry up to a certain degree. They have the advantage to be significantly faster in computer simulations, while keeping most of the good properties of Ginsparg-Wilson fermions.

Domain Wall Fermions [29–31] are constructed as four-dimensional boundaries from a five dimensional theory. In the massless case the construction leads to two Weyl fermions with opposite chirality on the two opposite four-dimensional "branes". Their interaction is exponentially suppressed. For finite extent of the fifth dimension the remaining explicit chiral

symmetry breaking leads to a residual mass scale m_{res}. One way to quantify the size of m_{res} are anomalous contributions to axial Ward identities [32]. It was found that m_{res} can also depend on the choice of the gauge action [33].

The *Fixed Point Action* is a completely different approach [34]. It is an approximation of a perfect lattice action, where *perfect* means that it is totally free of lattice artefacts. The method to construct the action is based on renormalisation group transformations. The trajectory through the fixed point at $\beta = \infty$ defines the perfect action. The hope is now, that the known fixed point action, which coincides with the unknown perfect action at $\beta = \infty$ stays close to the trajectory at finite β.

A general problem of approximate Ginsparg-Wilson fermions is that their scaling with the lattice spacing is not known a priori. It depends on the quality of the approximation. Still their obvious advantage is that they seem to be feasible in simulations with dynamical fermions [35, 36].

2.5 The Quenched Approximation

Including the determinant of the fermion matrix Q (2.17) in the simulation is numerically very demanding. The scaling of best available algorithms with the quark mass is drastic [37]. Although there have been very encouraging developments for staggered fermions [38] (and references therein), and Wilson fermions [39, 40], dynamical simulations of Ginsparg-Wilson fermions are still in their infancy [41–43].

So the quenched approximation is a necessary evil in this context. It consists of setting the fermion determinant to a constant. Then it drops out of all expectation values. The procedure amounts to neglecting quark-anti-quark loops in the computation.

Of course the resulting theory is no longer "real" QCD. But the effect of the determinant is not always large. The general folklore is that the quenched approximation introduces a systematic uncertainty of the order of ten percent. This estimate is the usual size of the *scale ambiguity* of the quenched approximation. Using different quantities to convert to physical units leads to different, sometimes incompatible results. Often quenched results are published with different physical input parameters to make the ambiguity visible. In Figure 2.2 the results of a large-scale lattice simulation with O(a)-improved Wilson fermions are displayed. Two different input quantities — the K and the Φ meson mass — are used. There are strong indications that the effect disappears in *dynamical simulations* where the determinant is included [45].

The quenched approximation always has an unquantifiable systematic error. Of course this limits the precision that can be reached. Its use throughout this thesis is justified because the aim of the projects are qualitative. Especially in the case of the $\Delta I = 1/2$ rule the right order of magnitude is sufficient to draw conclusions of consequence. Since the quenched theory can also be described in Chiral Perturbation Theory the same low-energy constants can be obtained if it is possible to disentangle them from the new-appearing quenched ones.

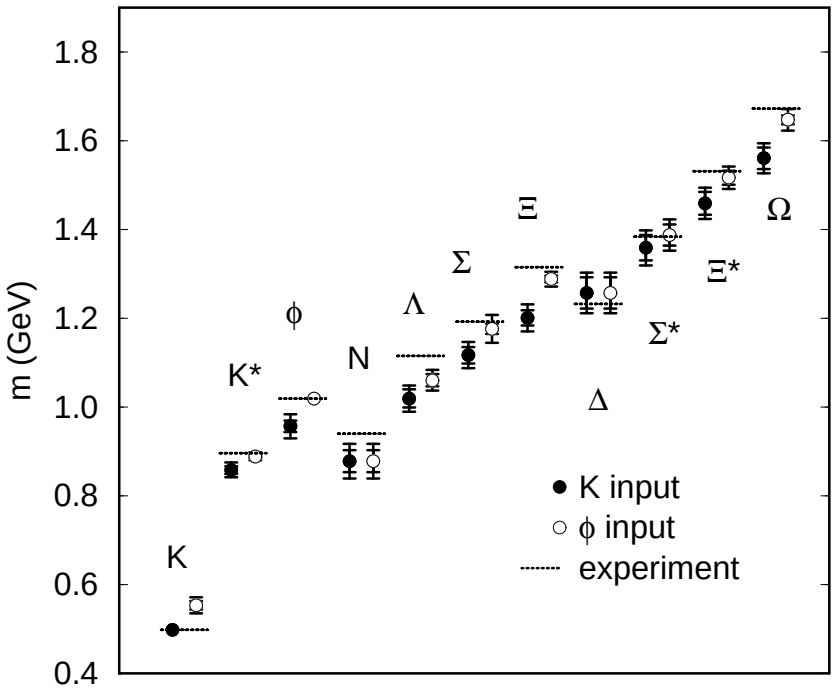

Figure 2.2: Quenched computation of the low-lying hadron spectrum by the CP-PACS collaboration. The plot has been published in [44].

3 Effective Theories for Low-Energy QCD

The treatment of QCD at low scales is still far from being fully understood. Lattice simulations provide numerical results from first principles, but they lack the intuitive understanding of analytic methods. Effective field theories (EFT) can be useful in this context since it is possible to use the adequate degrees of freedom for a certain setting. A prominent example is Chiral Perturbation Theory (ChPT) which is an EFT of pseudoscalar meson fields which incorporates chiral symmetry breaking.

The chapter is organised as follows. The first section introduces the standard version of Chiral Perturbation Theory. The second section deals with the interplay of ChPT and lattice QCD, especially with the determination of low-energy constants. In Section 3.3 the formulation of ChPT in a specific kinematical regime, namely the ϵ-regime is summarised. The last section contains a short description of a Random Matrix Model and its application to QCD in a small volume.

3.1 Chiral Symmetry Breaking

In addition to gauge symmetry the QCD Lagrangian (1.1) has an additional $\mathrm{SU}(N_\mathrm{f})_\mathrm{V}\times\mathrm{SU}(N_\mathrm{f})_\mathrm{A}$ global symmetry. It is softly broken through the non-degenerate quark masses. But the symmetry is also spontaneously broken to the $\mathrm{SU}(N_\mathrm{f})_\mathrm{V}$ subgroup. This means the apparent symmetry is not realised on the quantum level. According to Goldstone's theorem [46] this leads to a massless bosonic particle for every "broken" generator. Considering two-flavour QCD one finds three very light particles in the spectrum: the pions. They are not exactly massless because the symmetry is not exact. The mesons with strangeness are still relatively light considering the strange quark mass of the order of 100 MeV.

An elegant way to describe the effective degrees of freedom of QCD with spontaneously broken axial symmetry is Chiral Perturbation Theory [47, 48]. This effective theory is constructed to contain the same global symmetries as QCD and describes the low-energy degrees of freedom in a non-renormalisable field theory of pion fields U. It can be extended to contain the full pseudoscalar octet of mesons. Chiral Perturbation Theory is an asymptotic expansion in the meson momentum p_μ and the quark mass m which counts as $\mathrm{O}(p^2)$. Within the ChPT-Lagrangian

$$\mathcal{L}_\mathrm{ChPT} = \sum_i \mathcal{L}_{2i}, \tag{3.1}$$

new counterterms have to be included at every order to cancel divergent loop contributions from lower order terms. Since the theory is non-renormalisable the coefficients in front of

the counterterms cannot be expressed through the existing parameters. Therefore one gets new free parameters, which are also called *low-energy constants* (LECs), at every order in the expansion.

The lowest order Lagrangian of the Euclidean version of ChPT reads

$$\mathcal{L}_2 = \frac{1}{4}F^2 \operatorname{Tr}\left[\partial_\mu U^\dagger \partial_\mu U\right] - \frac{1}{2}\Sigma \operatorname{Tr}\left[U\mathcal{M} + \mathcal{M}^\dagger U^\dagger\right]. \tag{3.2}$$

The two LECs appearing at this order are F, the pseudoscalar decay constant in the chiral limit and the chiral condensate,

$$\Sigma = -\frac{1}{3}\left\langle \overline{u}u + \overline{d}d + \overline{s}s \right\rangle, \tag{3.3}$$

for QCD with three flavours of dynamical fermions.

Since the expansion is asymptotic one cannot assign a strict convergence radius to it. Also higher order which require additional counterterms do not automatically increase the range of validity.

Within the *quenched approximation*, Section 2.5, it is also possible to define an effective field theory named Quenched Chiral Perturbation Theory (QChPT). In this framework it is not possible to decouple the flavour-singlet fields. While in ChPT the η' can be treated as heavy and therefore be neglected, it has to be included in QChPT [49].

The flavour-singlet field is denoted by Φ_0 and its contribution is a kinetic and a mass term in the lowest order Lagrangian,

$$\mathcal{L}_2^{\text{quenched}} = \mathcal{L}_2 + \frac{m_0^2}{2N_\text{c}}\Phi_0^2 + \frac{\alpha_\Phi}{2N_\text{c}}(\partial_\mu \Phi_0)^2. \tag{3.4}$$

Two new low-energy constants appear, the flavour-singlet mass m_0 and α_Φ, which multiplies the kinetic term. The most obvious effect of the new terms is the appearance of new logarithmic contributions which diverge in the chiral limit. The pseudoscalar mass becomes dependent on the new parameters,

$$m_\text{P}^2 = \frac{2m\Sigma}{F^2}\Big\{1 - \delta\left[\ln(y) + 1\right]\Big\} + \mathrm{O}\Big(m^2, m^2\ln(m)\Big), \tag{3.5}$$

where

$$\delta = \frac{m_0^2}{\Lambda^2 N_\text{f}}, \quad y = \frac{2m\Sigma}{\Lambda^2 F^2}, \quad \Lambda = 4\pi F. \tag{3.6}$$

Now the parameter Σ cannot be identified with the slope of m_P as a function of the quark mass, because of the logarithmic terms. Nevertheless the low-energy constant Σ is still occasionally called condensate.

3.2 Low-Energy Constants from Lattice Simulations

The unknown low-energy constants can be fixed by experimental input. For a recent review including estimates of the NLO coefficients, see [50]. Obviously the experimental results are

confined to the physical quark masses. In lattice QCD simulations the quark masses are free parameters within certain practical limits. Thus the predicted mass dependence within ChPT can be tested from first principles [51]. The basic procedure is simple, one computes a certain physical observable at various quark masses and compares directly to the estimate in ChPT. This can be a powerful method, but several aspects have to be taken into account.

- The quark masses must be small enough so that ChPT is valid.
- Lattice artefacts amount to a hard breaking of chiral symmetry. Strictly speaking one cannot compare lattice results directly to ChPT unless the regularisation preserves chiral symmetry.
- There is no proof that ChPT is the right low-energy description for QCD, or that ChPT at fixed order can reproduce a certain quark mass behaviour in QCD.

The first point is crucial and the main problem in simulations with dynamical quarks. For Wilson fermions even quenched simulations cannot go to very small quark masses because exceptional configurations appear which render the Monte Carlo algorithms inefficient.

The fact that it is impossible to define an exact range of validity for ChPT leads to further complications. An example here is the quark mass dependence of the pseudoscalar mass. The ratio m_{P}^2/m stays constant — as predicted from LO ChPT — up to m_{P} of the order of 700MeV where ChPT is clearly no longer applicable [39]. There is also the questions whether a good agreement with the leading order behaviour points to a small NLO effect or is just an accidental cancellation of higher orders.

The second point can be circumvented by including lattice artefact as additional terms in the chiral Lagrangian. The so-called lattice ChPT has been developed for several fermions actions. There is Wilson ChPT [52], twisted mass ChPT [53] and staggered ChPT [54, 55]. Of course the number of free parameters in these theories grows rapidly. It is possible to use *partially quenched* simulations to constrain them. Here one generates gauge configurations with a certain quark mass in the determinant and then simulates with several additional masses on this gauge background.

The third point can in principle be tested with lattice QCD computations. A clear discrepancy between QCD and ChPT would falsify ChPT. But in a case where it is possible to fit the data with the ChPT formula, but the resulting LEC does not reproduce the experimental value it is less obvious.

Our strategy when determining LECs is to use the standard ChPT without lattice terms. Since we use Ginsparg-Wilson fermions which preserve chiral symmetry the results can be directly compared with continuum ChPT. There is simply no need to add further term to account for symmetry breaking due to the lattice regularisation.

3.3 The ϵ-Regime of QCD

The limit of almost vanishing quark mass m at fixed volume V is called the *ϵ-regime* of QCD. In this rather peculiar situation the Compton wavelength of the pions, which are the lightest particles in the spectrum, becomes larger than the box size, Figure 3.1. For the dimensionless quantity $\mu = m\Sigma V$, where Σ is the chiral condensate, one gets $\mu \ll 1$ in the ϵ-regime. For the formulation of ChPT in large volume one assumes $\mu \gg 1$.

ChPT with finite volume effects (FVE) was first considered by Gasser and Leutwyler [56]. They showed how to treat FVE in the p-regime where the volume is still large enough to allow for mesons which "feel" the finite volume. Later Leutwyler and Smilga [57] noticed the importance of topological zero modes in small physical volume. The scheme governing the setting of ChPT in the *ϵ-regime* with its own specific power counting has been developed by Hansen [58]. As will be explained in more detail, the scheme assumes that the path integral of the effective field theory is dominated by zero-momentum modes of the pion fields.

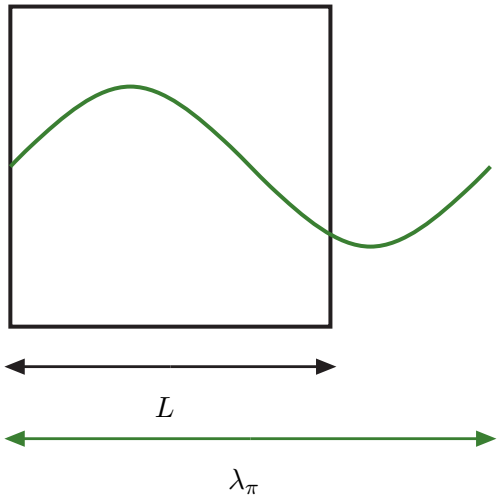

Figure 3.1: Illustration of length scales in the ϵ-regime. The Compton wave length of the pion is larger than the box length.

With chiral fermions on the lattice it has become possible to access the ϵ-regime numerically, with the caveat that numerical instabilities can occur in the computation of correlation functions. So far (nearly) all of these studies [59–61] have been quenched due to the extreme cost of dynamical Ginsparg-Wilson fermions. We will summarise the basic concepts of ϵ-regime ChPT in the following.

The leading order Lagrangian which is modified with respect to Eq. (3.2) by the vacuum angle θ,

$$\mathcal{L}_2 = \frac{1}{4}F^2 \operatorname{Tr}\left[\partial_\mu U^\dagger \partial_\mu U\right] - \frac{1}{2}\Sigma \operatorname{Tr}\left[\mathrm{e}^{\mathrm{i}\theta/N_\mathrm{f}}\mathcal{M}U + \mathrm{e}^{-\mathrm{i}\theta/N_\mathrm{f}}U^\dagger\mathcal{M}^\dagger\right]. \tag{3.7}$$

For small quark mass m the path integral is dominated by the zero-momentum modes U_0. Therefore one splits the pion field U into U_0 and a (small) fluctuation $\xi(x)$,

$$U(x) = U_0 \exp\left(\frac{2\,\mathrm{i}\xi(x)}{F}\right), \tag{3.8}$$

with $U_0 \in \mathrm{SU}(N_\mathrm{f})$ and $\xi(x)$ a traceless and Hermitian matrix without constant mode,

$$\int_V \mathrm{d}^4x\, \xi(x) = 0. \tag{3.9}$$

Setting $\mathcal{M} = m\mathbb{1}$ the partition function in the effective theory now becomes,

$$\mathcal{Z}_\theta = \int_{\mathrm{SU}(N_\mathrm{f})} \mathrm{d}U_0[\mathrm{d}\xi] \exp\left[\int \mathrm{d}^4x\, \mathrm{Tr}\,(\partial_\mu\xi\partial_\mu\xi) + \frac{m\Sigma V}{2}\,\mathrm{Tr}\left(\mathrm{e}^{\,\mathrm{i}\theta/N_\mathrm{f}}U_0 + \mathrm{e}^{-\,\mathrm{i}\theta/N_\mathrm{f}}U_0^\dagger\right)\right]. \tag{3.10}$$

Here the measure has to be split similarly into,

$$[\mathrm{d}U] \to \mathrm{d}U_0[\mathrm{d}\xi], \tag{3.11}$$

where $\mathrm{d}U_0$ is the Haar measure for $\mathrm{SU}(N_\mathrm{f})$. We neglect additional terms appearing through the factorisation of the measure. In principle one gets [58],

$$[\mathrm{d}U] \to \mathrm{d}U_0[\mathrm{d}\xi](1 + A(\xi)). \tag{3.12}$$

The leading contribution to $A(\xi)$ is given by

$$A(\xi) = -\frac{N_\mathrm{f}}{6V}\int \mathrm{d}^4x\, \langle\xi^2\rangle, \tag{3.13}$$

Now one can see that for $\mu \equiv m\Sigma V \ll 1$ the assumption to treat $\xi(x)$, the modes with non-zero momentum, perturbatively in the path integral (3.10) is justified.

As mentioned before, it is necessary to introduce specific counting rules for the expansion in ϵ [58],

$$\begin{gathered}\int \mathrm{d}^4x = V \sim \mathrm{O}\big(\epsilon^{-4}\big), \quad \delta(x) \sim \mathrm{O}\big(\epsilon^4\big), \qquad \partial_\mu \sim p_\mu \sim \frac{1}{L} \sim \mathrm{O}(\epsilon), \\ m \sim \mathrm{O}\big(\epsilon^4\big), \qquad \xi \sim \mathrm{O}(\epsilon), \qquad F \sim \mathrm{O}(1).\end{gathered} \tag{3.14}$$

The counting has to be compared to the p-regime which sets the rules for ChPT in large physical volumes. There one has $m_\pi \cdot L \sim \mathrm{O}(1)$ and thus $m_\pi \sim \mathrm{O}(p)$.

The difficulty of a calculation in the ϵ-regime comes from the need to evaluate the integral over U_0 exactly. The remaining ξ integration is done perturbatively which is justified by $\xi \sim \mathrm{O}(\epsilon)$.

It is also relevant to restrict the partition function to individual topological sectors. This is done by a Fourier-transform with respect to θ,

$$\mathcal{Z}_\theta = \sum_{\nu=-\infty}^{\infty} \mathrm{e}^{-\,\mathrm{i}\nu\theta}\mathcal{Z}_\nu, \qquad\qquad \mathcal{Z}_\nu = \frac{1}{2\pi}\int_0^{2\pi} \mathrm{d}\theta\, \mathrm{e}^{\,\mathrm{i}\theta\nu}\mathcal{Z}_\theta. \tag{3.15}$$

The factor $\mathrm{e}^{\mathrm{i}\theta\nu}$ is written as

$$\mathrm{e}^{\mathrm{i}\theta\nu} = U_\theta^{N_\mathrm{f}\nu}, \quad \text{with} \quad U_\theta = \mathrm{e}^{\mathrm{i}\theta/N_\mathrm{f}}, \tag{3.16}$$

and then absorbed into the determinant of $U_0' = U_\theta U_0 \in \mathrm{U}(N_\mathrm{f})$,

$$\mathcal{Z}_\nu = \int [\mathrm{d}\xi] \int\limits_{\mathrm{U}(N_\mathrm{f})} \mathrm{d}U_0' (\det U_0')^\nu \exp\left[\int \mathrm{d}^4x \,\mathrm{Tr}\,(\partial_\mu\xi\partial_\mu\xi) + \frac{m\Sigma V}{2}\,\mathrm{Tr}\left(U_0' + U_0'^\dagger\right)\right]. \tag{3.17}$$

The time dependence of correlation functions of local densities or currents is qualitatively different in the ϵ-regime from the well known behaviour of exponential decays. Here the correlators depend polynomially on t and have an explicit ν-dependence as well. As an example we want to compare the ϵ- and p-regime expressions for the correlator of the left-handed current,

$$C^{ab}(t) = \int \mathrm{d}^3x \left\langle J_0^a(x) J_0^b(0)\right\rangle, \quad J_\mu^a = \overline{\psi}\gamma_\mu P_- T^a \psi, \quad P_- = \frac{1}{2}(1-\gamma_5), \tag{3.18}$$

where T^a is a generator of $\mathrm{SU}(N_\mathrm{f})$ in flavour space.

In the effective theory the current is built from the ChPT equivalent of the axial and vector current which are found via a Noether procedure,

$$\mathcal{J}_\mu^a = \frac{F^2}{2}\,\mathrm{Tr}\left[T^a U \partial_\mu U^\dagger\right]. \tag{3.19}$$

The LO p-regime expression for $\mathcal{C}(t)$, defined by $\mathcal{C}^{ab}(t) = \mathrm{Tr}[T^a T^b]\mathcal{C}(t)$ reads [61],

$$\mathcal{C}(t) = \frac{1}{2} m_\mathrm{P} F_\mathrm{P}^2 \frac{\cosh\left[\left(\frac{T}{2} - |t|\right) m_\mathrm{P}\right]}{2\sinh\left[T\frac{m_\mathrm{P}}{2}\right]}. \tag{3.20}$$

In the ϵ-regime one gets

$$\mathcal{C}(t) = \frac{F^2}{2T}\left[1 + \frac{N_\mathrm{f}}{F^2}\left(\frac{\beta_1}{\sqrt{V}} - \frac{T^2 k_{00}}{V}\right) + \frac{\mu T^2}{F^2 V}\sigma_\nu(\mu)\left(\frac{t}{T} - \frac{1}{12}\right)^2\right], \tag{3.21}$$

with $\mu = m\Sigma V$ and

$$\begin{aligned}\sigma_\nu(\mu) &= \mu\Big\{I_\nu(\mu)K_\nu(\mu) + I_{\nu+1}(\mu)K_{\nu-1}(\mu)\Big\} + \frac{\nu}{\mu}, \\ &\approx \frac{|\nu|}{\mu}, \quad \text{for} \quad \mu \ll 1.\end{aligned} \tag{3.22}$$

where I_ν and K_μ are modified Bessel functions. The other coefficients depend on the aspect ratio T/L. For the choice $T/L = 32/12$, [62] quotes $\beta_1 = 0.00582$ and $k_{00} = 0.08333$. In Figure 3.2 the qualitative difference is apparent. In practice it may be difficult to judge whether one should use Eq. (3.20) or Eq. (3.21) to fit a numerical result in a certain range of quark masses. In the intermediate range both formulae may be applicable. Usually one assumes that for $\mu < 1$ the ϵ-regime is reached.

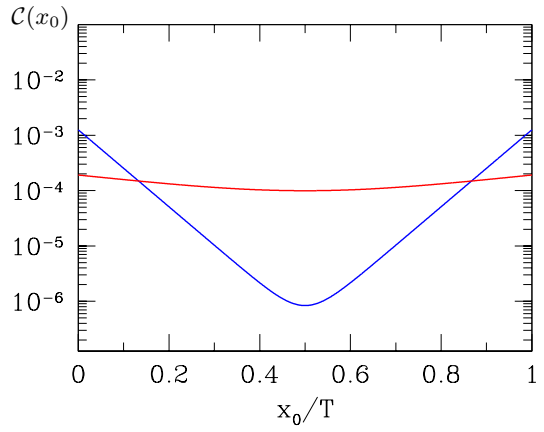

(a) Comparison of the ϵ-regime at $\nu = 3$ (red) and p-regime (blue) expressions for $\mathcal{C}$. The quark mass in the p-regime is of the order of 50 MeV. The ϵ-regime expression becomes mass independent in the limit $\mu \to 0$.

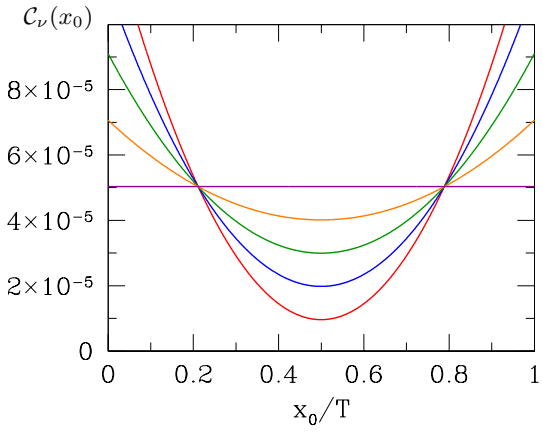

(b) Dependence on the topological index ν in the ϵ-regime. The slope increases with higher ν.

Figure 3.2: Illustration of the ChPT results for the two-point function $\mathcal{C}$.

3.4 The Chiral Condensate from Random Matrix Theory

The chiral condensate (3.3) can be extracted from lattice data via the Gell-Mann-Oakes-Renner relation (GMOR) [63],

$$-\left\langle \overline{\psi}\psi \right\rangle = \lim_{m\to 0} F_{\mathrm{P}}^2 \frac{m_{\mathrm{P}}^2}{2m}. \tag{3.23}$$

Several results in the quenched approximation [64–70] and also with dynamical fermions [71] have been published. The ratio on the r.h.s. is in principle well defined and goes to a constant for small m in full QCD. However it diverges in the quenched approximation since the ratio m_{P}^2/m acquires a logarithmic mass dependence. Therefore the result depends on the choice of the mass range and — in both cases — on a rather long extrapolation to the chiral limit.

Thus it is interesting to study other methods of estimating the LEC Σ which have different systematic uncertainties. Here we want to pursue an approach using a matching of QCD in small volume to Random Matrix Theory (RMT).

Matching to Random Matrix Theory

Random Matrix Theory (RMT) describes models of matrices with randomly distributed eigenvalues. In the ϵ-regime the Dirac operator is also dominated by constant zero modes. It was argued in [72–74] that QCD in small volume can be approximated by Random Matrix Models. The clearest correspondence can be seen in the distribution of the eigenvalues. In QCD they scale as $1/\Sigma V$. The size of the random matrix plays the role of the volume, the eigenvalues

scale as $1/N$. So assumption is that eigenvalues are distributed in the same way for QCD and the matrix model up to a scale factor.

The simplest model within the universality class of matrix models that can be used to describe the spectrum of the massless Dirac operator is the *Gaussian Chiral Unitary Random Matrix Model*. Considering $N \times N$ matrices of the type,

$$\hat{D} = \begin{pmatrix} 0 & W \\ -W^\dagger & 0 \end{pmatrix}, \tag{3.24}$$

with the complex $N_+ \times N_-$ matrix W ($N_+ + N_- = N$). By construction it has $|N_+ - N_-|$ zero modes, so $\nu = N_+ - N_-$ can be identified with the topological charge in QCD. An expectation value of an arbitrary operator in the quenched limit of this models is given by,

$$\langle \mathcal{O} \rangle_\nu = \frac{1}{\mathcal{Z}_\nu} \int [\mathrm{d}W] \mathcal{O} \exp\left\{ -\frac{1}{2} N \operatorname{Tr}\left[W^\dagger W \right] \right\}. \tag{3.25}$$

At fixed index the lowest non-zero eigenvalues scale with $1/N$ for large N [75]. Therefore one considers the *microscopic spectral density*,

$$\rho_\nu^{(k)}(\zeta) = \lim_{N\to\infty} \langle \delta(\zeta - \lambda_k N) \rangle_\nu \,, \tag{3.26}$$

which is of order one. The prediction for the combined distribution of the scaled eigenvalues in RMT in terms of the Bessel functions J_ν is [76]

$$\rho_\nu(\zeta) = \frac{\zeta}{2} \Big\{ J_\nu(\zeta)^2 - J_{\nu+1}(\zeta) J_{\nu-1} \zeta \Big\}. \tag{3.27}$$

The individual distributions for the lowest eigenvalue in different topological sectors reads [77]

$$\rho_\nu^{(1)} = \frac{\zeta}{2} \mathrm{e}^{-\zeta^2/4} \det(I_{2+i-j}(\zeta)), \quad i,j = 1, \dots \nu, \tag{3.28}$$

where I_k is again a modified Bessel function.

With numerical simulation using Ginsparg-Wilson fermions it is possible to test the predictions from RMT. The ratios of eigenvalues are compared in [75] because they are scale independent. Agreement was found for volumes of $(1.5\,\mathrm{fm})^4$ upwards.

To extract the low-energy constant we use the predictions for the mean value to match to results of our simulations. It is also possible to match the whole distribution. This requires larger statistics, but is potentially more accurate. Since our overall result is limited by the accuracy in the renormalisation factor Z_S, we refrain from using the more complicated method of matching the distributions. The matching condition for the scaled eigenvalue in RMT,

$$\langle \lambda_k \rangle_\nu^{\mathrm{QCD}} \, \Sigma V = \langle \zeta_k \rangle_\nu^{\mathrm{RMT}}, \qquad k = 1, 2, \dots \tag{3.29}$$

allows the determination of Σ for each eigenvalue k and topological sector ν. In practice one is restricted to a few eigenvalues and the lowest topological sectors.

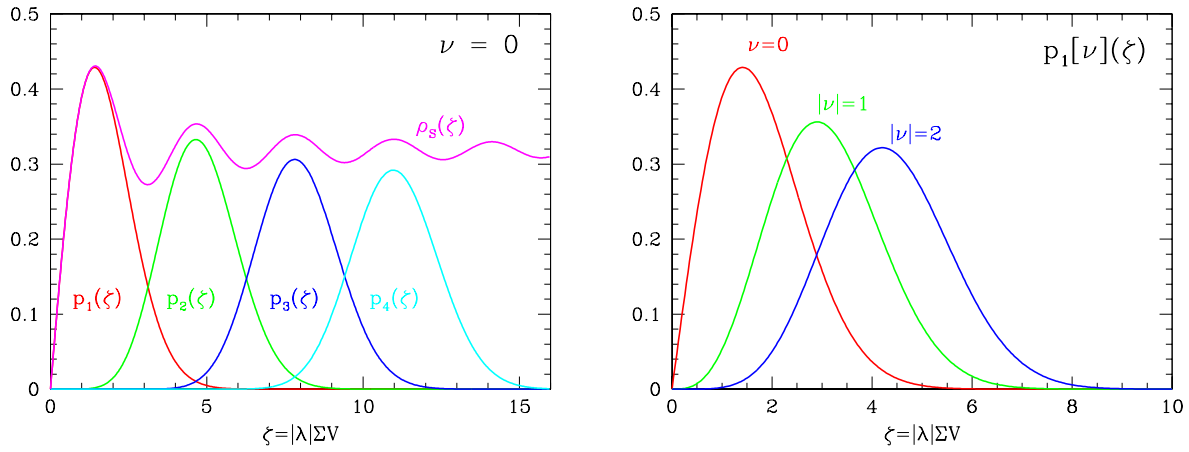

(a) The microscopic spectral density for $\nu = 0$ (upper curve) is built up from the individual eigenvalue distributions.

(b) The individual densities (3.28) for the lowest eigenvalue. The mean value moves to the right with increasing ν.

Figure 3.3: Illustration of Eqs. (3.27) and (3.28). The plots have been published in [61].

4 Numerical Techniques for the ϵ-Regime

Simulations of fermions with chiral symmetry — in this case overlap fermions — require involved numerical methods. In the first section of this chapter we summarise shortly the procedures published in [78] to tame the numerical cost of the overlap operator. In Section 4.2 the programmed inversion algorithm is described and tested with an existing efficient algorithm. The third section deals with the treatment of topological zero modes in the inversion process.

4.1 Approximation of the Neuberger Operator

The main ingredients developed [78] for an efficient numerical application of the Neuberger operator are

- separation of the lowest part of the spectrum of the kernel operator (2.18),
- min-max polynomial approximation of the remaining part of the overlap operator,
- adaptive precision in the iteration steps of the inversion,
- low-mode preconditioning of the inversion to reduce the mass dependence.

The need to evaluate the sign function of an operator — defined in Eq. (2.24) — makes it advantageous to separate the discrete part of the spectrum. This also ensures that it is always possible to define an approximate sign function via polynomials with a definite precision and at a relatively moderate cost.

Let $\mathcal{P}_-$ and $\mathcal{P}_+$ be the projectors on the space spanned by the lowest eigenvectors of Q with positive and negative eigenvalues, where Q is defined in (2.17). Then one can write the sign function as [78]

$$\operatorname{sign}(Q) = \mathcal{P}_+ - \mathcal{P}_- + (1 - \mathcal{P}_+ - \mathcal{P}_-) X P(X^2), \quad \text{with} \quad X = \frac{Q}{\|Q\|}. \tag{4.1}$$

The *optimal* polynomial approximation P of the sign function in an interval excluding a small neighbourhood of the origin can be found by minimising the error

$$\delta \equiv \max_{\epsilon \le y \le 1} \left| 1 - \sqrt{y} P(y) \right|. \tag{4.2}$$

Here ϵ is chosen smaller that the smallest eigenvalue of Q which has not been projected out. For $\epsilon > 0$ the sign function is approximated by $xP(x^2)$ in the whole interval with a maximal

deviation of δ. The minimisation has an unique solution [78] and it is helpful to expand $P(x)$ in the basis of the Chebyshev polynomials. The deviation of the approximate Neuberger operator $\tilde{D}_m$ from the exact operator D_m is bounded by

$$\|\tilde{D}_m - D_m\| \leq \frac{1}{a}\left(1 + s - \frac{1}{2}am\right)\left[2\left(\kappa_+ + \kappa_-\right) + \delta\right], \tag{4.3}$$

where κ_+ and κ_- parametrise the deviation of the projectors $\mathcal{P}_+$ and $\mathcal{P}_-$ from their exact form. Usually one has $\kappa_\pm \leq 10^{-8}$.

Once the overlap operator is constructed, one can begin the propagator calculation. The inversion is performed in an iterative procedure which is preferable for large sparse matrices [79]. Since we have control over the precision at which the operator is defined[1], in each step the residual of the inversion can be tuned to match this precision. This also makes it possible to start with fields in *single precision* (32bit) and switch to *double precision* (64bit) once the result is accurate enough to benefit from it. It is especially beneficial to use single precision because the program makes use of the so called *SSE registers* of modern processors.

The cost of the inversion of a large matrix is proportional to its *condition number*. In most relevant cases the condition number is dominated by a few very small eigenvalues of the matrix (or operator). Usually the eigenvalues of the massive Dirac operator are bounded from below by the bare mass. But once the lowest eigenvalues become of the same order as the mass parameter this is no longer true. It leads to a strong dependence of the condition number and thus of the inversion time on the mass. The cost of a simulation with overlap fermions explodes below a certain quark mass because of this effect. But there is hope: only a handful of eigenvalues are usually small enough to spoil the efficiency of the inversion algorithm. It is possible to compute the corresponding eigenvectors (low modes) at the needed precision explicitly using a Ritz functional iteration. The method to separate their contribution before the numerical inversion is be described in more detail in the following section.

4.2 Inversion Algorithms

There are several iterative algorithms for sparse matrices, c.f [79]. We choose to use the *generalised minimal residual* (GMRES) algorithm and compare it to the more conventional *conjugate gradient* (CG). An advantage of the GMRES algorithm is that it is possible to invert non-Hermitian matrices which is not possible with CG.

The GMRES algorithm is a *Krylov*-space method. That means the approximate solution ψ_d of the linear system

$$A\psi = \eta, \tag{4.4}$$

is determined from a d-dimensional affine subspace $\psi_0 + \mathcal{K}_d$ by imposing the orthogonality condition

$$\eta - A\psi_d \perp \mathcal{L}_d = A\mathcal{K}_d. \tag{4.5}$$

[1] Or more exactly on the degree of residual chiral symmetry breaking.

From an initial guess ψ_0 the Krylov space is constructed using $\rho_0 \equiv \eta - A\psi_0$,

$$\mathcal{K}_d \equiv \text{span}\left\{\rho_0, A\rho_0, A^2\rho_0, \ldots, A^{d-1}\rho_0\right\}. \tag{4.6}$$

Given an orthogonal basis $\{\phi_i\}$ of $\mathcal{K}_d$ the algorithm constructs the approximate solution by minimising the residue

$$J_d \equiv ||\eta - A(\psi_0 + Y_d)||, \tag{4.7}$$

where $Y_d \in \mathcal{K}_d$. The unique set of coefficients $\{y_i\}$ then characterises the solution,

$$Y_d = \sum_{i=1}^{d-1} y_i \phi_i. \tag{4.8}$$

In the following we want to explain in more detail how low mode preconditioning (LMP) is implemented in the inversion. One assumes a set of low modes $\{v_i\}$ corresponding to the N_{low} lowest eigenvalues of $A = D^\dagger D$ and P is a projector on the subspace spanned by the $\{v_i\}$. Then it is possible to write the original linear system as

$$PAP\psi = P\eta - PA(1-P)\psi, \tag{4.9a}$$

$$(1-P)\{A - AP(PAP)^{-1}PA\}(1-P)\psi = (1-P)\eta - PA(1-P)\psi. \tag{4.9b}$$

Now it is possible to solve Eq. (4.9b) and thereby obtain $(1-P)\psi$. Afterwards the missing part can be computed without much effort by just inserting the result in Eq. (4.9a). To make the solution explicit we introduce

$$\phi = (1-P)\psi \equiv \psi - \sum_{i=1}^{N_{\text{low}}} (v_i, \psi) v_i, \tag{4.10}$$

and rewrite Eq. (4.9b) as

$$(1-P)A\phi - \sum_{i=1}^{N_{\text{low}}} r_i \frac{1}{\lambda_i}(r_i, \phi) = (1-P)\eta - \sum_{i=1}^{N_{\text{low}}} r_i \frac{1}{\lambda_i}(v_i, \phi). \tag{4.11}$$

Here we use that v_i is an approximate eigenvector of A, i.e. $Av_i = \lambda_i v_i + r_i$ and $(,)$ denotes the scalar product. The explicit construction of the whole solution then reads

$$\psi = \phi + \sum_{i=1}^{N_{\text{low}}} r_i \frac{1}{\lambda_i}\left[(v_i, \eta) - (r_i, \phi)\right]. \tag{4.12}$$

The additional numerical effort is dominated by the determination of the low modes, while the linear algebra for the scalar products and projectors is negligible.

The aim of low-mode preconditioning is to reduce the growth in computer time for the inversion of the Dirac operator with decreasing mass. Since the computation of a few low

modes is already a substantial numerical effort[2], one has to ask whether it is beneficial to apply LMP in a certain project or not. The general finding here is that it helps already for quite heavy quark masses — around the strange quark mass — and is absolutely necessary when going below $m_s/2$. Of course the mass dependence of different algorithms is not the same. The algorithms GMRES with and without LMP are compared with the conjugate gradient (CG) at several bare quark masses. From Figure 4.1a one can infer that the mass dependence of the

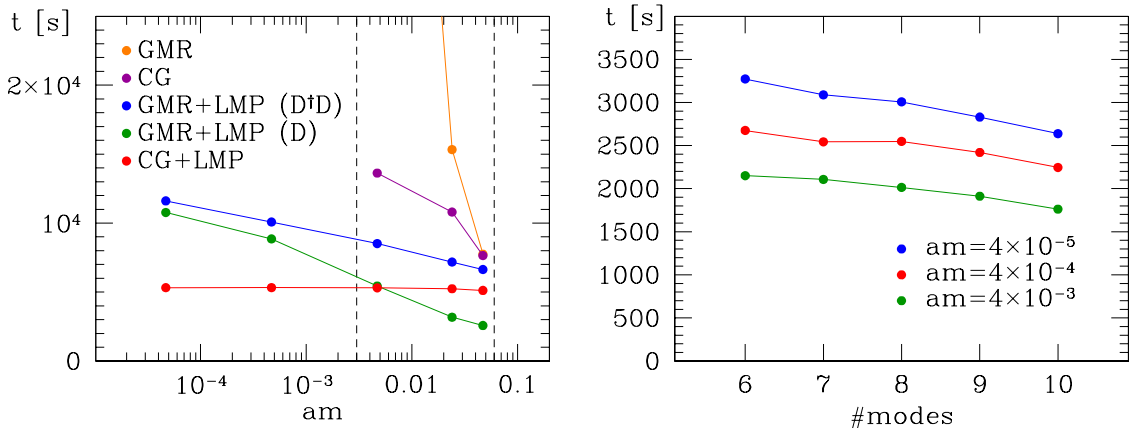

(a) Time for one inversion using several algorithms for a range of bare quark masses which cover several orders of magnitude at fixed coupling $\beta = 5.85$ and $N_{\text{low}} = 6$. The dashed lines indicate the upper and lower bounds for the quark masses, which are used in this thesis.

(b) Effects of the number of low modes used in LMP on the inversion time at $\beta = 6.0$. The scaling is roughly linear in the considered range for all three very small masses.

Figure 4.1: Tests of the GMRES algorithm with LMP on a 16^4 lattice (single processor).

CG algorithm with LMP is essentially flat while the GMRES shows an exponential behaviour with a small coefficient, however. The simulation which form the basis of this work include quarks with bare masses between 5 and 100 MeV. In this region both algorithms seem to be suitable, while at almost vanishing quark mass the CG has an advantage. And obviously LMP is beneficial over the whole range of "interesting" quark masses. Keeping the high cost for the determination of the low modes in mind, it is obviously unnecessary to use more a few low modes for the inversion. In Figure 4.1b it is shown that the time for an inversion is decreased by less than 20% when going from 6 to 10 low modes.

[2]The time used for the determination of the low modes is typically of the order of twenty percent of the time of the whole program.

4.3 Propagator in the Presence of Zero Modes and the Precision Issue

For the computation of the quark propagator it is necessary to perform an inversion in both chirality sectors[3]. The full propagator,

$$\begin{aligned} S(x,y) &\equiv \left[\left(1-\tfrac{1}{2}\overline{a}D\right) D_m^{-1}\right](x,y), \\ &= \frac{1}{1-\frac{1}{2}\overline{a}m}\left[D_m^{-1}-\tfrac{1}{2}\overline{a}\right](x,y), \end{aligned} \tag{4.13}$$

is then constructed in two steps from the chirality components of ψ ($= D_m^{-1}\eta$): $P_\sigma\psi$ and $P_{-\sigma}\psi$, ($\sigma = -\nu/|\nu|$, unless $\nu = 0$, where $\sigma = -1$). Here ν is the topological index of the gauge field determined via zero mode counting. After computing

$$P_\sigma\psi = P_\sigma(\gamma_5 D)^{-2}P_\sigma\gamma_5 D_m P_{-\sigma}\eta, \tag{4.14}$$

the opposite chirality sector is given by,

$$D_m P_{-\sigma}\psi = \eta - D_m P_\sigma\psi. \tag{4.15}$$

On a gauge background with vanishing topological index Eq. (4.15) is solved by

$$P_{-\sigma}\psi = (P_{-\sigma}D_m P_{-\sigma})^{-1}\left[P_{-\sigma}\eta - P_{-\sigma}D_m P_\sigma\psi\right]. \tag{4.16}$$

In the presence of exact zero modes Eq. (4.16) has to be modified. Let P_0 be a projector on the subspace of zero modes. Using P_0, the contribution of the zero modes can be subtracted from the source field and added after the inversion:

$$P_{-\sigma}\psi = \frac{1}{m}P_0 P_{-\sigma}\eta + (P_{-\sigma}D_m P_{-\sigma})^{-1}\left[(1-P_0)P_{-\sigma}\eta - P_{-\sigma}D_m P_\sigma\psi\right]. \tag{4.17}$$

Solving Eq. (4.17) numerically with low-mode preconditioning requires some more work due to the interplay of low and zero modes. The low modes of $P_\sigma D^\dagger D P_\sigma$ are computed in the sector without zero modes with a given relative precision. That means

$$P_\sigma D P_\sigma v_i = \lambda_i v_i + r_i, \qquad ||r_i|| < \delta, \tag{4.18}$$

with some given δ. The low modes in the other sector can be computed just by applying D to each of the v_i,

$$w_i \equiv P_{-\sigma}\gamma_5 D v_i. \tag{4.19}$$

The set $\{w_i\}$ are approximate eigenvectors of $P_{-\sigma}DP_{-\sigma}$ with the same eigenvalue. This can be easily seen using the Ginsparg-Wilson relation (2.20),

$$\begin{aligned} P_{-\sigma}DP_{-\sigma}w_i &= P_{-\sigma}DP_{-\sigma}\gamma_5 DP_\sigma v_i = \frac{\overline{a}}{2}P_{-\sigma}D^\dagger DP_{-\sigma}\gamma_5 DP_\sigma v_i, \\ &= \frac{\overline{a}}{2}P_{-\sigma}\gamma_5 D\gamma_5 D\gamma_5 DP_\sigma v_i == \frac{\overline{a}}{2}P_{-\sigma}\gamma_5 DD^\dagger DP_\sigma v_i, \\ &= P_{-\sigma}\gamma_5 DP_\sigma DP_\sigma v_i = \lambda_i P_{-\sigma}\gamma_5 DP_\sigma v_i = \lambda_i w_i. \end{aligned} \tag{4.20}$$

[3] Or to invert D directly without splitting into $P_\sigma DP_\sigma$, $\sigma = +, -$, of course.

But the residual term r_i in Eq. (4.18) has been ignored in this calculation. For w_i one gets

$$P_{-\sigma} D P_{-\sigma} w_i = \lambda_i w_i + s_i, \tag{4.21}$$

with $s_i = P_{-\sigma}\gamma_5 D r_i$. The term s_i is no longer strictly bounded and this can spoil the efficiency of low-mode preconditioning. One can improve the numerical precision of w_i in the same way as the original low modes v_i are computed[4]. Using the approximate w_i (4.19) as input reduces the computational effort for the minimisation of the Ritz functional. Here it is again necessary to take the topological zero modes into account. The operator has to be altered to $P_\sigma D^\dagger D P_\sigma P_0$ where P_0 is a projector on the subspace spanned by the zero modes. Otherwise it can happen that the iteration starts with an approximate low mode and then flips to a zero mode.

[4]This improvement is crucial for the inversion but does not affect the procedure described in Sect. 6.4 [80].

5 Chiral Condensate

The chapter contains the description of a computation of the renormalisation of the chiral condensate — the parameter that indicates spontaneous chiral symmetry breaking — with overlap fermions in the quenched approximation [81]. The main novelty of this work is the use of non-perturbative renormalisation together with the first sound continuum extrapolation for Ginsparg-Wilson fermions.

We describe the computation of the renormalisation factor of the scalar density in the first section. In the second section the corresponding factor for the axial current is determined. The continuum extrapolation of the chiral condensate is performed in Section 5.3. The last section contains scaling tests for the kaon decay constant and the K^* mass.

5.1 Renormalisation of the Scalar Density

The matching of QCD in small volume and Random Matrix Theory, Section 3.4, gives rise to an estimate of the chiral condensate. Since it is done in lattice regularisation the bare condensate requires renormalisation and is subject to lattice artefacts. Our main assumption here is that Σ in the quenched case still renormalises like the scalar density. The aim of renormalising the scalar density $\overline{\psi}\psi$ non-perturbatively in a chirally symmetric discretisation can in principle be reached with a Schrödinger Functional (SF) approach [82–84]. But the SF formalism for overlap fermions is still "under construction" [85–87]. Therefore we opted for a more indirect way first described in [88]. The result for a certain observable is matched to the same but renormalised quantity in the continuum limit. As input we use results from ALPHA and UKQCD [89] obtained with O(a)-improved Wilson fermions.

We match two quantities, the quark mass m and the matrix element

$$G_{\mathrm{P}}^{\mathrm{bare}} = \langle 0|P(0)|\mathrm{PS}\rangle\,, \quad P(x) = (\overline{\psi}_r\gamma_5\psi_s)(x). \tag{5.1}$$

The flavour indices r and s are chosen to be different to restrict the correlator to the flavour non-singlet contribution. For both observables the aim is to extract the renormalisation group invariant (RGI) Z-factor. It is beneficial to use RGI quantities for the matching since they are scale invariant by definition, see Appendix B.

Due to the chiral Ward identities the renormalisation factors of the scalar density (Z_{S}) and the pseudoscalar density (Z_{P}) are equal for chirally symmetric regularisations [90],

$$Z_{\mathrm{S}} = Z_{\mathrm{P}} = \frac{1}{Z_{\mathrm{m}}}. \tag{5.2}$$

Therefore both matching conditions should lead to compatible results [88],

$$\widehat{Z}_{\mathrm{S}} = \frac{r_0 m}{U_{\mathrm{M}}}\Big|_{(r_0 m_{\mathrm{P}})^2 = x_{\mathrm{ref}}}, \tag{5.3}$$

$$\widehat{Z}_{\mathrm{P}} = \frac{U_{\mathrm{P}}}{r_0 G_{\mathrm{P}}^{\mathrm{bare}}}\Big|_{(r_0 m_{\mathrm{P}})^2 = x_{\mathrm{ref}}}. \tag{5.4}$$

The hat denotes that the resulting Z-factors are the RGI ones, because the matching is done with quantities which have been computed in this scheme. Here U_{M} is the RGI quark mass in the continuum limit in units of the hadronic radius r_0. U_{P} is the RGI matrix element (5.1) also in the continuum and in units of r_0. The reference point is chosen at the physical kaon mass:

$$x_{\mathrm{ref}} = (r_0 m_{\mathrm{K}})^2 = 1.5736, \tag{5.5}$$

if one assumes $r_0 = 0.5\,\mathrm{fm}$. The values for quantities U_{M} and U_{P} at the reference point can be extracted from the data in [89]:

$$U_{\mathrm{M}} = 0.181(6), \qquad U_{\mathrm{P}} = 1.802(42). \tag{5.6}$$

The errors of three percent for U_{M} and two percent for U_{P} clearly show the limitations of this renormalisation procedure. The quoted error estimates restrict the precision that can be reached for $\widehat{Z}_{\mathrm{S}}$.

Using a physical quantity for the matching — in our case the RGI quark mass — also prevents us from obtaining a result for the physical strange quark mass in our calculation. If we were to use the Z_{S} obtained from condition (5.3) the resulting quark mass would always coincide with the result published in [89].

Another method to renormalise quark bilinear is the RI-MOM scheme [91], for an application to GW fermions, see [92].

5.1.1 Lattice Setup

As mentioned before the study is performed in the quenched approximation. The pure gauge background is simulated using heatbath and overrelaxation algorithms (Appendix A.1) which are well known and efficient algorithms for SU(N) gauge theories. We use the Wilson gauge action, Eq. (2.11), at four values of the bare coupling which correspond to lattice spacings ranging from 0.124 fm to 0.075 fm. Here results on the hadronic radius r_0 introduced by Sommer [93] and the fit of r_0/a as a function of β published in [94] are used. The conversion to physical units is just a rough estimate by setting $r_0 = 0.5\,\mathrm{fm}$.

Since our preferred reference point is at the kaon mass, three different quark masses are simulated which are used to built pseudoscalar mesons from degenerate quarks with masses around the kaon (495 MeV). On our smaller lattices a fourth (and heavier) mass is added for exploratory studies at higher masses.

β	L/a	r_0/a	a [fm]	#cfgs
5.8458	12	4.026	0.124	200
5.9256	14	4.697	0.106	174
6.0000	16	5.368	0.093	200
6.1366	20	6.710	0.075	100

Table 5.1: Simulation parameters for the determination of mesonic two-point functions

The physical volume for our four lattices is chosen to keep finite volume effects (FVE) in the relevant quantities small. For two-point functions at zero spatial momentum it is common to go to values of the spatial extent L such that

$$m_{\mathrm{P}} \cdot L > 3, \tag{5.7}$$

to restrict FVE to the percent level, which is sufficient for this work. The bare coupling is tuned to ensure that $L = 1.49\,\mathrm{fm}$ on all our lattices to satisfy Eq. (5.7) for all masses considered. The magnitude of possible FVE is also checked directly on one lattice, cf. Subsection C.2.3. The time extend T is doubled with respect to L, a convenient way to obtain a longer fit range as there is no need to enlarge also L.

As seen from Table 5.1 the number of configuration lies between 100 and 200. Here we have monitored the statistical error of the primary observables and kept running until the level of precision needed for $\widehat{Z}_{\mathrm{S}}$ has been reached. On the larger lattices, especially at $L/a = 20$ fewer configurations are needed because of beneficial "self-averaging". That means the sum over the spatial volume extends over far more points which averages out some of the fluctuations.

5.1.2 Numerical Results

The masses and matrix elements from the corresponding two-point functions are obtained from standard least-square fits. Details of the procedure are described in Section A.3. We emphasise that there is no possible contribution from topological zero modes, since we use the left-handed current to compute the pseudoscalar mass. The correlator defined in (3.18) contains chiral projectors of the form $\gamma_\mu P_-$, where $P_- = \frac{1}{2}(1 - \gamma_5)$. The contribution of the zero modes in the spectral decomposition of the propagator is completely cancelled by these projectors. The results for our primary observables are summarised in Table 5.2. For each value of the lattice spacing the squared pseudoscalar mass is interpolated linearly in the bare quark mass to the reference point. Here we allowed for a non-zero intercept, (5.8). The best fit value for the intercept was found to differ from zero by more than one standard deviation for three of our four lattices, Table 5.3. But still a fit forced through the origin yields a correlated χ^2/d.o.f. below one. At the masses and precision reached here, it is not possible to give a decisive answer on the chiral behaviour of the pseudoscalar mass.

β	am	am_{PCAC}	am_{P}	$aF_{\mathrm{P}}^{\mathrm{bare}}$	$a^2G_{\mathrm{P}}^{\mathrm{bare}}$	am_{V}
5.8458	0.040	0.02359(6)	0.262(9)	0.0417(10)	0.1185(61)	0.532(37)
	0.053	0.03134(7)	0.294(8)	0.0424(9)	0.0889(39)	0.537(31)
	0.067	0.03973(8)	0.327(8)	0.0434(8)	0.0718(28)	0.556(24)
	0.113	0.06769(11)	0.421(6)	0.0469(7)	0.0488(14)	0.631(14)
5.9256	0.034	0.02120(13)	0.235(7)	0.0389(10)	0.0877(39)	0.502(21)
	0.046	0.02875(14)	0.266(6)	0.0397(10)	0.0657(26)	0.515(15)
	0.057	0.03569(15)	0.292(6)	0.0405(9)	0.0547(19)	0.529(12)
	0.097	0.06120(17)	0.377(4)	0.0433(9)	0.0378(11)	0.579(7)
6.0000	0.030	0.01927(7)	0.217(6)	0.0346(7)	0.0814(42)	0.424(15)
	0.040	0.02576(7)	0.247(5)	0.0356(6)	0.0612(27)	0.445(11)
	0.050	0.03229(7)	0.273(5)	0.0366(6)	0.0501(20)	0.462(9)
	0.085	0.05543(9)	0.352(3)	0.0403(5)	0.0342(10)	
6.1366	0.024	0.01638(6)	0.168(5)	0.0296(7)	0.0447(21)	0.360(28)
	0.032	0.02185(6)	0.195(4)	0.0301(6)	0.0356(14)	0.378(20)
	0.040	0.02734(6)	0.218(4)	0.0309(6)	0.0305(11)	0.389(15)

Table 5.2: Results for meson masses and decay constants computed at several values of quark masses at each lattice spacing. The results for am_{P} and $aF_{\mathrm{P}}^{\mathrm{bare}}$ were extracted from correlators of the left-handed current.

For $G_{\mathrm{P}}^{\mathrm{bare}}$ we decided to fit its inverse to m_{P}^2. Only the three mass values close to the kaon mass were used in both cases.

$$(r_0 m_{\mathrm{P}})^2 = A + B r_0 m, \tag{5.8}$$

$$\frac{1}{r_0^2 G_{\mathrm{P}}^{\mathrm{bare}}} = C + D(r_0 m_{\mathrm{P}})^2. \tag{5.9}$$

The resulting coefficients A-D are listed in Table 5.3.

β	A	B	C	D
5.8458	0.128(92)	6.02(16)	−0.117(25)	0.545(18)
5.9256	0.169(94)	6.49(20)	−0.019(20)	0.435(15)
6.0000	0.147(94)	7.49(18)	−0.082(22)	0.364(13)
6.1366	−0.031(81)	8.09(25)	0.150(24)	0.265(10)

Table 5.3: Best fit values for the mass interpolation of m_{P} (5.8) and $G_{\mathrm{P}}^{\mathrm{bare}}$ (5.9). The errors come from a jackknife procedure.

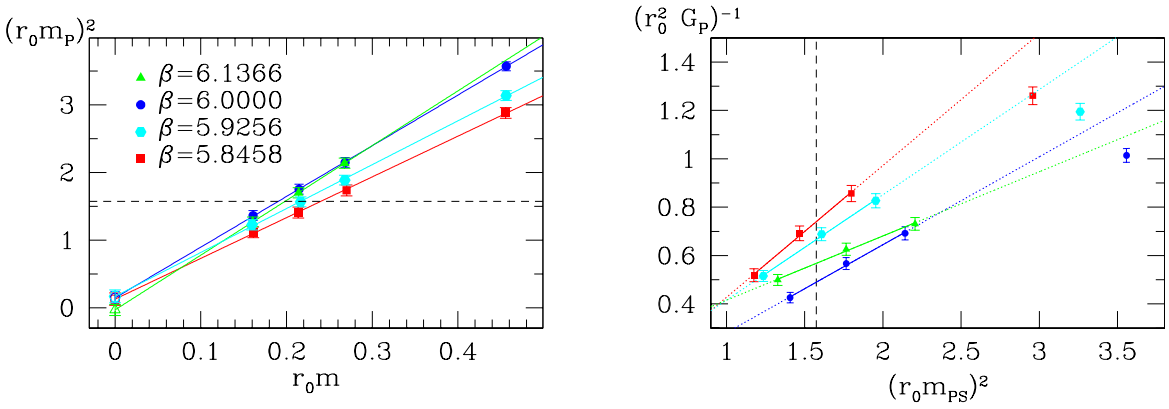

(a) $(r_0 m_{\mathrm{P}})^2$ as a function of $r_0 m$.

(b) $1/(r_0 G_{\mathrm{P}}^{\mathrm{bare}})^2$ as a function of $(r_0 m_{\mathrm{P}})^2$.

Figure 5.1: Linear interpolations for m_{P} and $G_{\mathrm{P}}^{\mathrm{bare}}$. The dashed lines represent the reference point $(r_0 m_{\mathrm{P}})^2 = 1.5736$.

β	$\widehat{Z}_{\mathrm{S}}$	$\widehat{Z}_{\mathrm{P}}$	Z_{A}
5.8458	1.28(6)	1.33(4)	1.710(5)
5.9256	1.19(7)	1.20(4)	1.611(3)
6.0000	1.05(5)	0.88(6)	1.553(2)
6.1366	1.01(4)	1.02(5)	1.478(2)

Table 5.4: Non-perturbative determinations of $\widehat{Z}_{\mathrm{S}}$, $\widehat{Z}_{\mathrm{P}}$ and Z_{A}.

After we have obtained a fit through the data points for both observables, we interpolate to the reference point, which is alluded to by the dashed lines in Figure 5.1. Only the three lighter masses have been used to obtain the results at the reference point, because they are distributed closely around x_{ref}. Then the values for $r_0 m|_{x_{\mathrm{ref}}}$ and $r_0 G_{\mathrm{P}}^{\mathrm{bare}}|_{x_{\mathrm{ref}}}$ are inserted into Eqs.(5.3) and (5.4) to infer the renormalisation factors in the RGI scheme.

The values for $\widehat{Z}_{\mathrm{S}}$ and $\widehat{Z}_{\mathrm{P}}$ (Table 5.4) agree within errors, except for one lattice spacing. The discrepancy at $\beta = 6.0$ is most likely a statistical fluctuation. We choose the values from the matching of the RGI quark mass as our final result [81]. To simplify the comparison with other results an interpolating curve over the considered range of the bare coupling is computed, which describes $\widehat{Z}_{\mathrm{S}}$ with a precision of 5%,

$$\widehat{Z}_{\mathrm{S}}(\beta) = 1.045 - 0.899(\beta - 6) + 4.36(\beta - 6)^2. \tag{5.10}$$

The formula is of course only valid for the overlap parameter $s = 0.4$.

Some of the possible sources of systematic errors of the results have been investigated and it was found that their effect is well within the quoted uncertainty, see Appendix C.2.3 for

details.

5.1.3 Comparison with Lattice Perturbation Theory

The curve (5.10) can directly be compared with results from lattice perturbation theory. The

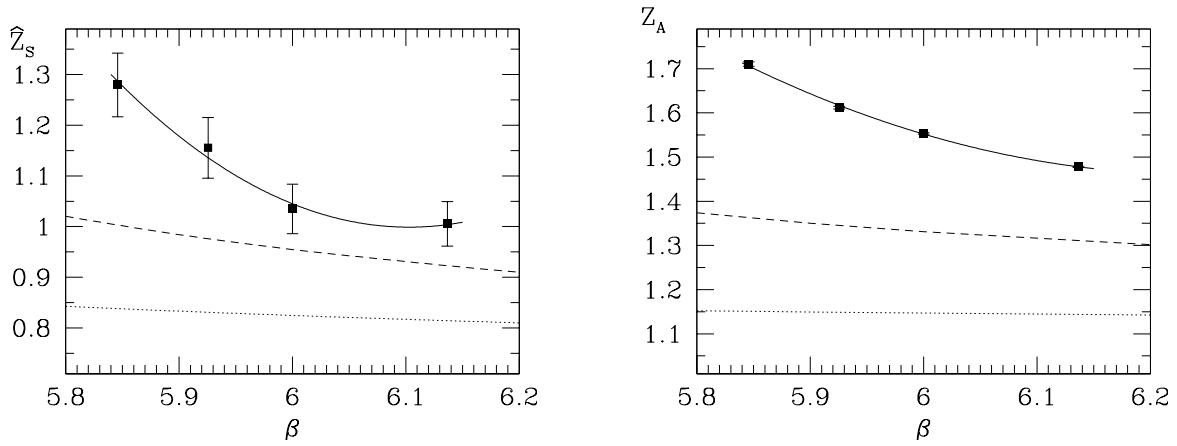

(a) $\widehat{Z}_S$ as a function of β

(b) Z_A as a function of β

Figure 5.2: The solid line denotes the fit of eq. (5.10), eq. (5.17) respectively. The dotted and dashed curves represent the results of bare and mean-field improved perturbation theory at one loop order.

one-loop expansion for $\widehat{Z}_S$ has been computed in [90, 95],

$$\widehat{Z}_S^{\rm pt}(g_0) = \frac{\overline{m}_{\overline{\rm MS}}(\mu)}{M}\left\{1 + g_0^2\left[\frac{1}{2\pi^2}\ln(a\mu) + z_S^{(1)}\right] + {\rm O}(g_0^4)\right\}, \tag{5.11}$$

with $z_S^{(1)} = 0.147107$ for our choice of $s = 0.4$. The conversion factor from the $\overline{\rm MS}$-scheme to the RGI-scheme at 4-loop level has been computed in [89],

$$\frac{\overline{m}_{\overline{\rm MS}}}{M}(\mu = 2{\rm GeV}) = 0.72076. \tag{5.12}$$

It is known that bare lattice perturbation theory converges very slowly. A way to improve on this is the idea of mean field improvement [96]. The bare coupling g_0 is replaced with a more "continuum like" coupling $\tilde{g}$ defined by

$$\tilde{g}^2 = \frac{g_0^2}{\langle u_0^4\rangle}. \tag{5.13}$$

The average plaquette $\langle u_0^4\rangle$ supplies a non-perturbative input for the *boosted* coupling $\tilde{g}$. The mean field improved version of the perturbative renormalisation factor reads

$$\widehat{Z}_S^{\rm mf}(g_0) = \frac{\overline{m}_{\overline{\rm MS}}(\mu)}{M}\left(\frac{1+s}{1+\tilde{s}}\right)\left\{1 + \tilde{g}^2\left[\frac{1}{2\pi^2}\ln(a\mu) + z_S^{(1)} + u_0^{(1)}\left(\frac{3-s}{1+s}\right)\right]\right\}, \tag{5.14}$$

where $\tilde{s} = 3 + (s-3)/u_0$ [88] and $u_0^{(1)} = -1/12$. For $\beta \geq 6.0$ the mean field improved results comes quite close to the non-perturbative one, cf. Fig. 5.2a. But there is still a 20% discrepancy below $\beta = 6.0$. The bare perturbation theory gives a much lower result for the whole range of considered lattice spacings.

5.2 Renormalisation Factor of the Axial Current

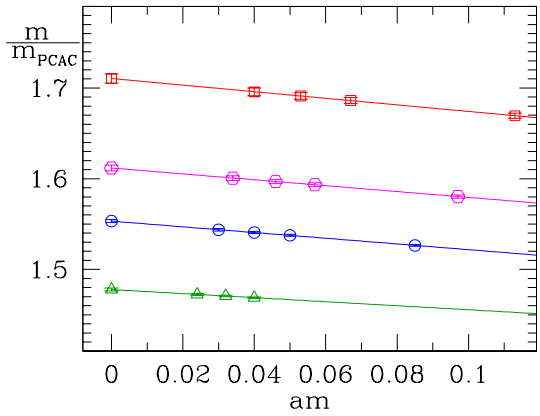

Figure 5.3: The quark mass dependence of $\frac{m}{m_{\mathrm{PCAC}}}$. The value of β increases from top to bottom. Z_{A} is defined as the value of this ratio in the limit of vanishing quark mass.

The other relevant renormalisation factor for quark bilinears with Ginsparg-Wilson fermions is Z_{A}. It is straightforward to calculate it from the PCAC relation. The current quark mass can be defined as,

$$am_{\mathrm{PCAC}} = \frac{1}{2}\frac{\frac{1}{2}(\partial_0 + \partial_0^*)C_{\mathrm{JP}}(x_0)}{C_{\mathrm{PP}}(x_0)}, \tag{5.15}$$

where ∂_0, ∂_0^* denote the forward and backward lattice derivatives, respectively. The numerical results (Table 5.2) are obtained by averaging over the central third of the time direction, $x_0 \in [T/3, 2T/3]$.

Since m_{PCAC} and the bare quark mass m are both proportional to the renormalised quark mass[1], the chiral limit of the ratio,

$$\lim_{m\to 0}\frac{m}{m_{\mathrm{PCAC}}} = \frac{Z_{\mathrm{A}}}{Z_{\mathrm{m}}Z_{\mathrm{P}}} = Z_{\mathrm{A}}, \qquad \text{using} \qquad Z_{\mathrm{m}} = \frac{1}{Z_{\mathrm{P}}}, \tag{5.16}$$

is just the ratio of renormalisation factors. The mass ratio is found to depend only weakly on m, Fig. 5.3. Therefore it is justified to perform a linear extrapolation to the chiral limit. Further details can be found in Appendix C.1.

[1] There is no additive mass renormalisation due to chiral symmetry.

Again a polynomial fit is performed to make it possible to use the result for other values of β,

$$Z_{\mathrm{A}}(\beta) = 1.552(2) - 0.756(14)(\beta - 6) + 1.57(14)(\beta - 6)^2. \tag{5.17}$$

The fit describes the data with a precision of 0.5%.

In [97] Dürr, Hölbling and Wenger compared our result with determinations of Z_{A} for other gauge actions. The main outcome of their study is that Z_{A} is significantly smaller for improved gauge actions and thus closer to the perturbative estimate which clearly underestimates the non-perturbative value, Figure 5.2b.

5.3 Continuum Extrapolation

The bare low-energy constant Σ is obtained from a matching of eigenvalues in QCD and Random Matrix Theory. The approach has been described in Section 3.4. For three of the relevant bare couplings there are published results, specifically the lattices labelled B_1, B_2 and B_3 of reference [75]. We added a fourth lattice at $\beta = 5.9256$ to get better control over the continuum extrapolation. The detailed numerical results for this data point can be found in Appendix C.2. The statistical error of the bare condensate is of the order of one percent.

The procedure to estimate Σ leads to ambiguities, since we consider several eigenvalues and topological sectors. The full results for all twelve considered cases can be found in Appendix C.2. The spread within the results is illustrated in Figure 5.4b. All twelve points lie within the error band of our chosen result. We choose the second lowest eigenvalue in the sector with $\nu = 1$ as our final result,

$$r_0^3 \widehat{\Sigma} = 0.293 \pm 0.021. \tag{5.18}$$

An estimate for Σ from an average over all twelve results yields a consistent results with a much small errors,

$$r_0^3 \widehat{\Sigma}_{\mathrm{av}} = 0.2871 \pm 0.0061. \tag{5.19}$$

Since the individual results are not totally uncorrelated and considering sources of systematic errors as quenching and the limited applicability of RMT we keep (5.18) as a final result with a conservative error estimate.

It is notable that the continuum value differs from the one at $a = 0.124\,\mathrm{fm}$ ($\beta = 5.8458$) only by four percent which is well within the statistical uncertainty. Thus the lattice artefacts for this quantity are practically absent. Comparing the non-perturbative result for $\widehat{Z}_{\mathrm{S}}$ with the one from mean-field improved perturbation theory yields a value which is practically identical, Figure 5.4a. The difference becomes visible at finite lattice spacing and is significant on the coarser lattices. This should serve as a warning to quote results at finite lattice spacing especially with perturbative renormalisation.

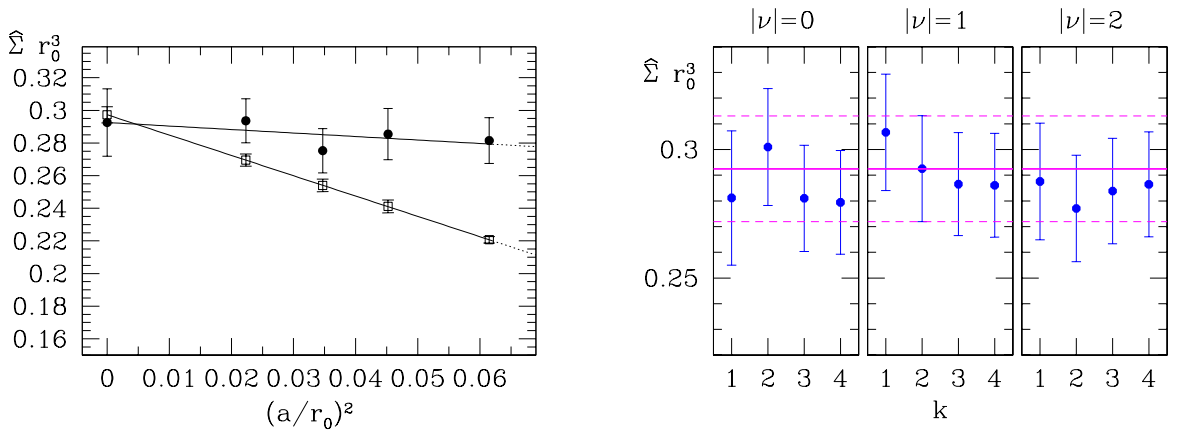

(a) Continuum extrapolation of $r_0^3\widehat{\Sigma}$. Full circles denote the results obtained using non-perturbative renormalisation factors, while open squares represent values resulting from applying mean-field improved perturbation theory.

(b) The variation of $r_0^3\widehat{\Sigma}$ in the continuum limit, arising from choosing different eigenvalues and topological sectors in the determination of the bare condensate. The solid and dashed lines represent the result for $k = 2$, $|\nu| = 1$ which is used for our main result.

Figure 5.4: Result for the renormalised scalar density.

Furthermore, it is interesting to compare our results with determinations from other lattice actions [64, 66, 67, 71], Figure 5.5. Though one has to be careful because of different systematic uncertainties in the approaches. To allow a comparison we convert our result to the $\overline{\text{MS}}$-scheme at 2GeV and divide therefore by the factor $\overline{m}_{\overline{\text{MS}}}/M = 0.72076$ which was obtained in [89],

$$r_0^3\Sigma_{\overline{\text{MS}}}(2\,\text{GeV}) = 0.406 \pm 0.029. \tag{5.20}$$

A conversion to physical units for a quenched result is always ambiguous. To set the value for r_0 we use two quenched results in the continuum limit: the kaon decay constant,

$$r_0 F_\text{K}\sqrt{2} = 0.415 \pm 0.009, \qquad F_\text{K} = 113\,\text{MeV}, \tag{5.21}$$

obtained by ALPHA/UKQCD [89] and the nucleon mass,

$$r_0 m_\text{N} = 2.670 \pm 0.042, \qquad m_\text{N} = 939.6\,\text{MeV}, \tag{5.22}$$

from the CP-PACS collaboration [44]. The resulting condensate is

$$\Sigma_{\overline{\text{MS}}}(2\text{GeV}) = \begin{cases} (285 \pm 9\,\text{MeV})^3, & \text{scale set by } F_K \\ (261 \pm 8\,\text{MeV})^3, & \text{scale set by } m_N \end{cases}. \tag{5.23}$$

5.4 Further Scaling Tests

The scaling of basic observables with the lattice spacing in simulations with Ginsparg-Wilson (GW) fermions is of interest, because it allows an estimate of the region in β where results

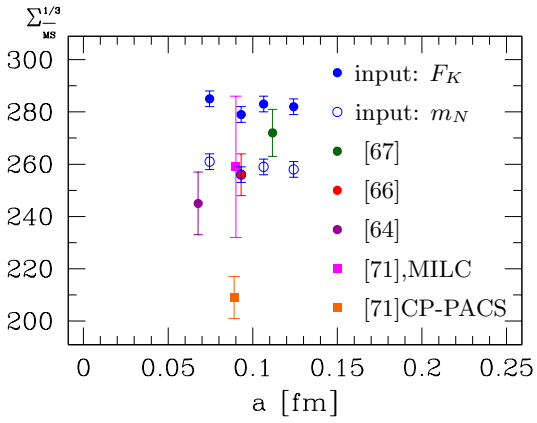

Figure 5.5: Comparison of our value for Σ with published results as a function of the lattice spacing. Circles denote quenched results while the only available unquenched data are from McNeile [71] who used two different data sets and the GMOR formula. The scale ambiguity in our data is of the order of the spread between the different results.

can be obtained reliably. The most direct criterion here is, how well the results scale with the square of the lattice spacing[2] and of course the absolute size of the lattice artefacts. The results for the condensate in the previous section already indicate that the $\mathrm{O}(a^2)$ contribution is small.

Now we want to extend the scaling test to further observables, namely the kaon decay constant and the $K^\star$ mass. To define the physical point, we assume again $(r_0 m_K)^2 = x_{\mathrm{ref}} = 1.5736$.

5.4.1 Kaon Decay Constant

The pseudoscalar decay constant can be obtained from a matrix element of the left-handed current (A.12). The results for the bare decay constant at four different lattice spacings and quark masses have already been given in Table 5.2. The interpolation to the physical point — the kaon — is again done linearly in the square of the pseudoscalar mass. The renormalised decay constant is then obtained by multiplying with our result on Z_{A} listed in Table 5.4. In Table 5.5 we summarise the coefficients of the following fits,

$$r_0 F_{\mathrm{P}}^{\mathrm{bare}} = A + B(r_0 m_{\mathrm{P}})^2 \tag{5.24}$$

$$r_0 m_{\mathrm{V}} = C + D(r_0 m_{\mathrm{P}})^2 \tag{5.25}$$

The values for $r_0 F_{\mathrm{K}} = r_0 F_{\mathrm{P}}|_{x_{\mathrm{ref}}}$ are then extrapolated to the continuum limit (CL) using the ansatz

$$r_0 Z_{\mathrm{A}}(a) F_{\mathrm{K}}^{\mathrm{bare}}(a) = (r_0 F_{\mathrm{K}})_{\mathrm{CL}} + \mathrm{O}(a^2)\,. \tag{5.26}$$

Similar to the case of the condensate one can compare this fully non-perturbative result with

[2] GW-fermions are automatically "O(a)-improved".

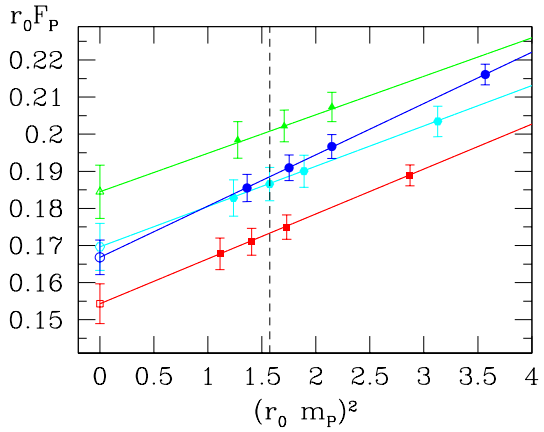

(a) Mass interpolation of $F_{\mathrm{P}}^{\mathrm{bare}}$. The dashed line shows our reference point $x_{\mathrm{ref}} = 1.5736$. The value of β decreases from top to bottom.

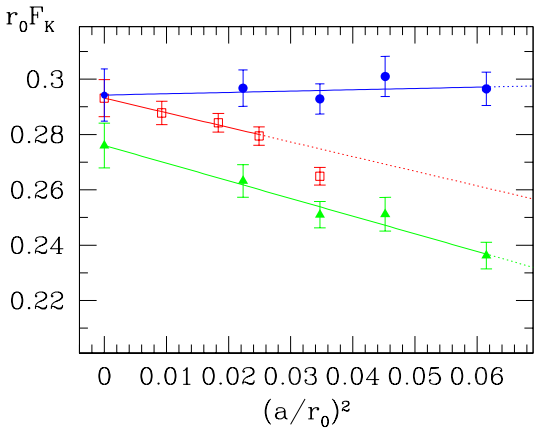

(b) Continuum extrapolation of $r_0 F_{\mathrm{K}}$. Full circles denote our results, while the open squares are the data of [89], employing O(a) improved Wilson fermions. The full triangles are our data with Z_{A} from mean-field improved perturbation theory.

Figure 5.6: Results for the kaon decay constant.

β	A	B	C	D
5.8458	0.154(5)	0.0121(16)	1.95(43)	0.16(26)
5.9256	0.169(6)	0.0108(19)	2.10(24)	0.19(10)
6.0000	0.167(5)	0.0138(10)	2.09(13)	0.20(5)
6.1366	0.184(7)	0.0104(24)	1.75(31)	0.36(10)

Table 5.5: Best fit values for the mass interpolation of $F_{\mathrm{P}}^{\mathrm{bare}}$ (5.24) and m_{V} (5.25). The errors come from a jackknife procedure.

β	$r_0 F_{\mathrm{K}}$	$r_0 m_{\mathrm{K}^*}$
5.8458	0.296(6)	2.209(89)
5.9256	0.301(7)	2.403(95)
6.0000	0.293(5)	2.413(66)
6.1366	0.297(7)	2.328(165)
∞	*0.294(9)*	*2.32(29)*

Table 5.6: Kaon decay constant and K^*-mass, in units of r_0. $\beta = \infty$ denotes the continuum limit.

perturbative renormalisation. The green points in Fig. 5.6b are a combination of our result for $F_{\mathrm{P}}^{\mathrm{bare}}$ and the perturbative Z_{A} from [90] with mean field improvement. One can see that this procedure is rather dangerous. Even though the results are compatible in the CL, the difference at finite lattice spacing is again large. For comparison we also include the result on F_{K} from [89] in the plot. It agrees very nicely with ours and the scaling region for overlap fermions seems to extend to much coarser lattice spacings than for Wilson fermions at least in the quenched approximation. The slope of our continuum extrapolation is again consistent with zero.

5.4.2 Vector Meson Mass

The vector meson mass is computed from the exponential decay of the correlator defined in (A.13). On the relatively small lattices it is not easy to get a signal for the correlator. Therefore we apply a technique called *Jacobi smearing* [98] to enhance the signal. The point source of the inversion is replaced by a spatially extended object. In an iterative procedure a so called *smearing kernel* is applied to the source field. It contains of a three dimensional covariant derivative operator and leads to a broadening of the source in a gauge invariant way. We postpone a more detailed description of Jacobi smearing to Appendix A.4.

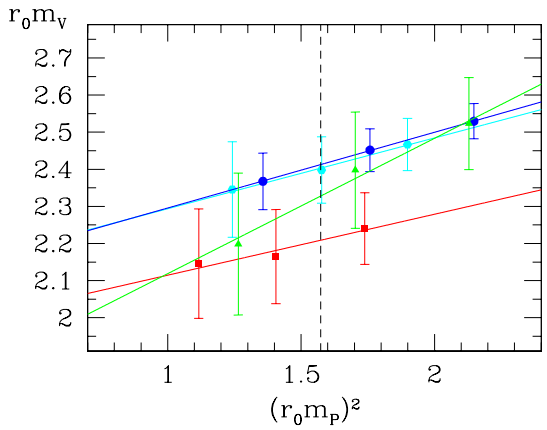

(a) Mass interpolation of m_{V}. The dashed line is the reference point $r_0 m_{\mathrm{P}}^2 = 1.5736$.

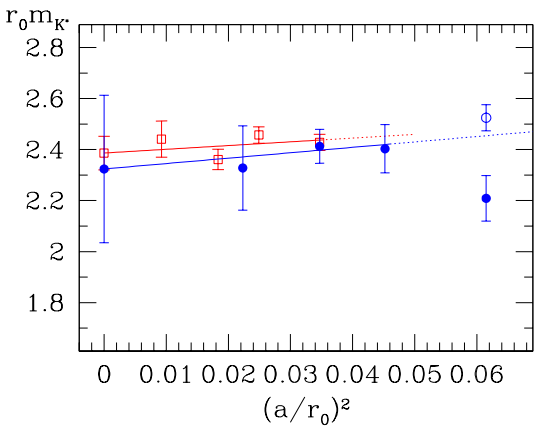

(b) Scaling behaviour of $r_0 m_{\mathrm{K}^*}$. The blue points are our data where the rightmost point has been excluded from the extrapolation. The red points are published in [89] and given for comparison.

Figure 5.7: Results for m_{K^*}.

Despite the gain in accuracy through the use of smearing, it was still difficult to establish a reliable result on the coarsest lattice. The value for m_{V} at $\beta = 5.8458$ depends strongly on the fit range. In Figure 5.7b we include two values for m_{K^*} at this lattice spacing. The filled circle corresponds to a fit interval of $x_0/a \in [7, 11]$, while the open circle stems from a fit including $x_0/a \in [5, 11]$. Therefore the continuum extrapolation is done excluding the data

point at $\beta = 5.8458$. This leads to a much larger error on the value of the vector meson mass in the continuum limit, Table 5.6. The results are once again consistent with the data from O(a)-improved Wilson fermions published in [89].

6 Non-Leptonic Kaon Decays

The chapter comprises a study of hadronic weak matrix elements at practically vanishing quark mass. The key ingredients of the study are the use of Ginsparg-Wilson fermions, the new technique called low-mode averaging and the matching to ϵ-regime Chiral Perturbation Theory. The strategy of the computation was introduced in [62]. The aim of the project is to extract the low-energy constants g_1^+ and g_1^- which parametrise the kaon decays in the framework of ChPT.

In the first section basic concepts and notations are introduced. Section 6.2 is a brief account of the effective weak Hamiltonian that contains the relevant four-quark operator. The third section summarises the concept of using a SU(4) flavour symmetry. Section 6.4 describes the numerical technique called *low- mode averaging* which is crucial for obtaining results at very small quark masses. The fourth section contains the numerical results at different values of the topological index. In the fifth section a brief summary of the renormalisation of four fermion operators is given. Section 6.7 lists the relevant quantities in Chiral Perturbation Theory in finite volume. In the last section the results are related to the corresponding low energy constants and amplitudes.

6.1 Phenomenology of $K \to \pi\pi$ Decays

Kaon decays offer the opportunity to test non-perturbative QCD results with very accurate data in a regime where no long extrapolation in the quark mass is needed. Some very simple experimental observations are still far from being understood. A prominent example is the $\Delta I = 1/2$ rule for the decay of a neutral kaon into two pions.

The relevant decays with their corresponding partial decay rates are [99]

$$K^+ \to \pi^+\pi^0, \qquad \Gamma_{\pi^+\pi^0} = 1.13 \times 10^{-14}\,\text{MeV}, \tag{6.1a}$$

$$K_S^0 \to \pi^+\pi^-, \qquad \Gamma_{\pi^+\pi^-} = 5.06 \times 10^{-12}\,\text{MeV}, \tag{6.1b}$$

$$K_S^0 \to \pi^0\pi^0, \qquad \Gamma_{\pi^0\pi^0} = 2.31 \times 10^{-12}\,\text{MeV}. \tag{6.1c}$$

Only the CP-even combination of K^0 and $\overline{K}^0$ denoted by K_S^0 can decay into two pions. Using the definition for the transition amplitude

$$T(K^0 \to \pi\pi)_I \equiv \mathrm{i} A_I \, \mathrm{e}^{\mathrm{i}\delta_I} \quad I = 0, 2, \tag{6.2}$$

the decay rates can be written as

$$\Gamma_{\pi^+\pi^0} = \frac{3}{4} \frac{p}{16\pi m_K^2} A_2^2, \tag{6.3a}$$

$$\Gamma_{\pi^+\pi^-} + \Gamma_{\pi^0\pi^0} = \frac{p}{16\pi m_K^2}\left[A_0^2 + A_2^2\right], \tag{6.3b}$$

$$\Gamma_{\pi^0\pi^0} = \frac{1}{3}\frac{p}{16\pi m_K^2}\left[A_0^2 + 2A_2^2 - 2\sqrt{2}A_0A_2\cos(\delta_0^0 - \delta_0^2)\right], \tag{6.3c}$$

where $p = \sqrt{m_K^2 - 4m_\pi^2} = 413\,\mathrm{MeV}$ is the total three-momentum of the two pions if the kaon decays at rest. This yields a phenomenological value for the absolute values of the decay amplitudes of

$$A_0 = 4.69 \times 10^{-4}\,\mathrm{MeV}, \tag{6.4a}$$

$$A_2 = 2.12 \times 10^{-5}\,\mathrm{MeV}, \tag{6.4b}$$

which are real by definition. The unexpectedly large ratio $A_0/A_2 = 22.1$ is known as the $\Delta I = 1/2$ rule. The decay into the isospin zero state ($\Delta I = 1/2$) is preferred over the decay into the isospin two state ($\Delta I = 3/2$).

Since many years it is know that the main source of the enhancement must come from long distance contributions at a rather low scale. A simple perturbative estimate of the ratio is of O(1). Although lattice QCD seems to be ideal to attack this problem, there are many technical difficulties. The main obstacle arises from the Maiani-Testa no-go theorem [100], which states that decay amplitudes for two-body decay cannot be obtained from Euclidean correlation functions in large volume. A way to circumvent the issue is to use Chiral Perturbation Theory to relate the $K \to \pi\pi$ amplitudes to simpler $K \to \pi$ and $K \to vacuum$ amplitudes [101].

Another problem is the mixing with lower dimensional operators. It appears for Wilson fermions and leads to power divergencies through the dimensionful prefactors that come with the additional operators [102]. This problem is absent for Ginsparg-Wilson fermions [62].

6.2 Effective Weak Hamiltonian

$K \to \pi\pi$ decays occur via the exchange of a W-boson. The process can be described in terms of an effective $V - A$ current-current interaction,

$$S_\mathrm{w} = \frac{1}{2}g_\mathrm{w}^2(V_{us})^*V_{ud}\int \mathrm{d}^4x\mathrm{d}^4y\Big\{(\overline{s}\gamma_\mu P_- u)(x)D_{\mu\nu}(x-y)(\overline{u}\gamma_\mu P_- d)(y) - [u \to c]\Big\}, \tag{6.5}$$

where $g_\mathrm{w} = 4\sqrt{2}G_\mathrm{F}M_W^2$ and $V_{qq'}$ are elements of the CKM-matrix. The symbolic notation $\big[u \to c\big]$ means the same expression is repeated but the flavour assignment is changed from u to c. The top quark contribution has been neglected as it is suppressed by three orders of magnitude.

Since the dominant contribution to the W-propagator $D_{\mu\nu}(x-y)$ comes from the region around $x = y$, it is possible to use the operator product expansion (OPE) to evaluate the integral,

$$S_\mathrm{w} \approx \int \mathrm{d}^4x H_\mathrm{w}. \tag{6.6}$$

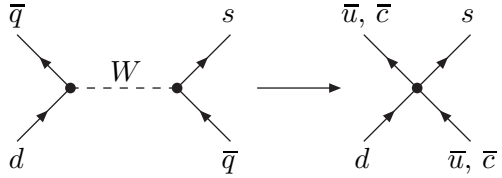

Figure 6.1: Illustration of the construction of the four-fermion vertex. The W "shrinks" to a point.

To lowest order the resulting effective Hamiltonian,

$$H_{\mathrm{w}} = \frac{g_{\mathrm{w}}^2}{4M_W^2} V_{us}^* V_{ud} \sum_{i=1}^{2} \Big\{ k_i^+ Q_i^+ + k_i^- Q_i^- \Big\}, \tag{6.7}$$

contains the operator $Q_1^\pm$, where

$$Q_1^\pm \equiv \Big\{ (\overline{s}\gamma_\mu P_- u)(\overline{u}\gamma_\mu P_- d) \pm (\overline{s}\gamma_\mu P_- d)(\overline{u}\gamma_\mu P_- u) - \big[u \to c\big] \Big\}. \tag{6.8}$$

Unsurprisingly the operator $Q_1^\pm$ has the $V-A$ structure of Fermi theory.

In principle there is a second operator one has to consider, which is given by

$$Q_2^\pm = (m_u^2 - m_c^2)(m_d \overline{s} P_+ d + m_s \overline{s} P_+ d), \tag{6.9}$$

for a diagonal mass matrix. But it does not contribute to physical matrix elements, since it vanishes for equal final and initial state momentum [62]. Nevertheless both operators mix under renormalisation for $m_c \neq m_u$.

The final step in this project will be to match the lattice QCD results to Chiral Perturbation Theory and thereby extract the relevant low-energy constants. It is straightforward to include the effective four-fermion interaction in the low-energy theory. The interaction Hamiltonian,

$$\mathcal{H}_{\mathrm{w}} = \frac{g_{\mathrm{w}}^2}{4M_W^2} V_{us}^* V_{ud} \left\{ g_1^+ \mathcal{Q}_1^+ + g_1^- \mathcal{Q}_1^- \right\}, \tag{6.10}$$

is of the same structure[1] as the one in QCD (6.7). The operator has to be expressed in terms of the degrees of freedom of ChPT:

$$\mathcal{Q}_1^\pm = \frac{F^2}{4} \Big\{ (U\partial_\mu U^\dagger)_{us} (U\partial_\mu U^\dagger)_{du} \pm (U\partial_\mu U^\dagger)_{ds} (U\partial_\mu U^\dagger)_{uu} - \big[u \to c\big] \Big\}. \tag{6.11}$$

Now one can construct correlation functions in QCD and in the effective theory which contain the operator Q_1 and its analogue $\mathcal{Q}_1$ and compare them. In the next sections we will give a detailed description of the QCD side of the calculation. The results in ChPT are summarised in Section 6.7.

[1] We use calligraphic letters for ChPT expressions.

A matrix element of a similar operator with a different flavour assignment can be used to describe $\Delta S = 2$ transitions, namely the effect of K_0–$\overline{K}_0$-mixing. It is common practice to define the B-parameter as the matrix element normalised by its value in the vacuum saturation approximation $\frac{8}{3}F_K^2 m_K^2$,

$$\left\langle \overline{K}_0 | \mathcal{O}_{\Delta S=2} | K_0 \right\rangle = \frac{8}{3} B_K F_K^2 m_K^2, \tag{6.12}$$

where

$$\mathcal{O}_{\Delta S=2} \equiv (\overline{s}\gamma_\mu P_- d)(\overline{s}\gamma_\mu P_- d) \tag{6.13}$$

There are several published results, most of them in the quenched approximation. The latest result by the Alpha collaboration [103] for the RGI matrix element is

$$\hat{B}_K = 0.789 \pm 0.046. \tag{6.14}$$

See also the recent review by Dawson [104], where he quotes $B_K(\overline{\mathrm{MS}}, 2\,\mathrm{GeV}) = 0.58(3)(6)$ as a world average. The second error covers an estimate of the effects of the non-degeneracy of the quark masses and quenching. The Kaon B-parameter is also relevant for ratio of direct and indirect CP-violation in $K \to \pi\pi$ decays, parametrised by the ratio ϵ'/ϵ.

6.3 The Chiral SU(4)-Symmetric Limit

In the following section we want to describe the basic strategy for our computation of the low-energy constants $g_1^\pm$ for $K \to \pi$ transitions. The simpler (and unphysical) matrix elements with one hadron in the final state yield the same low-energy constants as the $K \to \pi\pi$ matrix elements and can thus be used to extract meaningful results [101].

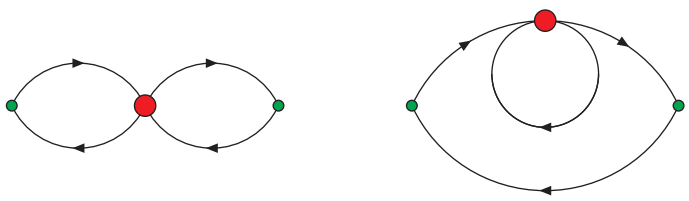

(a) "Figure eight" diagram (b) "Eye" diagram

Figure 6.2: Relevant diagrams for $K \to \pi$ decays. The small circle denote current insertions and the bigger circles the four-fermion operator.

Contributions to the $\Delta I = 1/2$ rule can originate at several different physical scales. Besides genuine QCD effects at the scale around 250MeV and final state (pion) interaction at

even lower scales also the charm quark mass with roughly 1GeV can contribute to the observed enhancement [105]. The final state interaction cannot easily be addressed in a lattice computation due to the Maiani-Testa no-go theorem for multiple particle states in Euclidean space-time [100]. In the future it may be possible to circumvent it with a *finite-size scaling* technique proposed by Lellouch and Lüscher [106], but the required volumes do not allow this with today's (super-) computers.

To disentangle the other two scales E_{QCD} and m_c a possible way was proposed in [62]. Simulations with Ginsparg-Wilson fermions (Subsection 2.4) of correlation function containing four-quark operators are conceptually much simpler due to the restricted operator mixing. Considering the relevant three-point functions as a function of the charm quark mass allows to check whether one of the possible contribution dominates or if the enhancement is built up from several smaller effects.

The first step is to set the charm quark mass equal to the up-quark mass to cancel contributions from the *eye diagram*, Figure 6.2 completely. The unphysical assumption $m_c = m_u = m_d = m_s$ exhibits a SU(4) chiral symmetry. The contact with the low energy constant is made through a matching with ChPT results which are reviewed in Section 6.7.

The three-point function describing the kaon decay reads,

$$C_1^{\pm}(x_0, y_0) \equiv \sum_{\vec{x},\vec{y}} \Big\langle \left[J_0(x)\right]_{du} \left[Q_1^{\pm}(0)\right] \left[J_0(y)\right]_{us} \Big\rangle, \tag{6.15}$$

with Q_1 defined in Eq. (6.8). Again the use of the left-handed current J_μ ensures that there is no contribution from topological zero modes to the observable. To compute the correlation function C_1, it is expressed through the quark propagator S, which consists of the fields $\overline{\psi}$ and $\tilde{\psi} = (1 - \frac{1}{2}\overline{a}D)\psi$. In the SU(4) case the Wick contraction of C_1 leads to

$$\begin{aligned} C_1^{\pm}(x_0, y_0) = \sum_{\vec{x},\vec{y}} \Big\{ &\Big\langle \mathrm{Tr}\left[\gamma_\mu P_- S(x,0)^\dagger \gamma_0 P_- S(x,0)\right] \mathrm{Tr}\left[\gamma_\mu P_- S(y,0)^\dagger \gamma_0 P_- S(y,0)\right] \Big\rangle \\ &\pm \Big\langle \mathrm{Tr}\left[\gamma_\mu P_- S(x,0)^\dagger \gamma_0 P_- S(x,0) \gamma_\mu P_- S(y,0)^\dagger \gamma_0 P_- S(y,0)\right] \Big\rangle \Big\}, \end{aligned} \tag{6.16}$$

where the first line contains the *colour-disconnected* and the second line the *colour-connected* contribution.

The ratio of the two correlators C_1^+ and C_1^- is the main observable of our study,

$$R_1^-/R_1^+ \equiv \frac{C_1^-(x_0, y_0)}{C_1^+(x_0, y_0)}. \tag{6.17}$$

In practice the inverse ratio R_1^+/R_1^- is statistically better behaved and is used to extract the results. We also consider the ratio of each three-point function with two-point functions of the left-handed current defined in Eq. (6.22),

$$R_1^\tau \equiv \frac{C_1^\tau(x_0, y_0)}{C(x_0) \cdot C(y_0)}, \quad \tau = +/-, \tag{6.18}$$

which allow the to extract the individual low-energy constants.

6.4 Low-Mode Averaging

In a conventional lattice QCD simulation the quark mass m is much larger than the smallest eigenvalues of the Dirac operator. That means the propagator cannot be dominated by a few low lying eigenmodes, since all eigenmodes are approximately given the same weight — $1/m$ — in the spectral representation,

$$S(y,x) = \sum_i \frac{\phi_i(x) \otimes \phi_i^*(y)}{\lambda_i + m}, \qquad \text{with} \qquad D\phi_i = \lambda_i \phi_i. \tag{6.19}$$

In the ϵ-regime $m \gg \lambda_i$ is no longer true. The mass can be of the same order or even smaller than the lowest eigenvalues. Fluctuations in the local density of the eigenmodes thus can be amplified significantly for individual eigenvalues. This leads to spikes in the Monte Carlo history of suitable observables which exceed the average fluctuations by two orders of magnitude. A way to cure these large fluctuations is low-mode averaging (LMA). It was independently introduced in [60] and [61]. If one is able to compute the eigenmodes of the Dirac operator with the smallest eigenvalues — a.k.a. low modes — explicitly, one can exploit translational invariance to reduce the statistical noise dramatically. The spectral representation of the propagator (6.19) is split into a "light" and a "heavy" part S_h, which is still computed through a numerical inversion:

$$S(y,x) = \sum_{i=1}^{N_\mathrm{low}} \frac{\phi_i(x) \otimes \phi_i^*(y)}{\lambda_i + m} + S_\mathrm{h}(y,x). \tag{6.20}$$

In practice the eigenvectors ϕ_i are constructed from eigenvectors of $P_\sigma D_m^\dagger D_m P_\sigma$,

$$\phi_i \equiv \begin{pmatrix} v_i \\ P_{-\sigma}\gamma_5 D P_\sigma v_i \end{pmatrix}, \tag{6.21}$$

where $P_\sigma D_m^\dagger D_m P_\sigma v_i = \alpha_i v_i$. To allow for such a procedure the eigenvectors must be computed with high precision beforehand. This is done via a Ritz functional minimisation. Details of the method can be found in [78].

6.4.1 A First Example: Two-Point Correlation Functions

The two-point function

$$C(x_0) = \sum_{\vec{x}} \left\langle J_\mu^\mathrm{l}(x) J_\mu^\mathrm{l}(0) \right\rangle, \tag{6.22}$$

of the left-handed current $J_\mu^\mathrm{l} = \overline{\psi}\gamma_\mu P_- \psi$ is considered, because it is free of zero-mode contributions. Applying LMA to C leads to three terms,

$$C(x_0) = C^\mathrm{ll}(x_0,0) + C^\mathrm{hl}(x_0,0) + C^\mathrm{hh}(x_0,0). \tag{6.23}$$

The "light-light" contribution only requires the knowledge of the low modes of the Dirac

(a) light-light (b) heavy-light (c) light-heavy (d) heavy-heavy

Figure 6.3: Diagrammatic illustration of the different contributions to the two-point function with LMA. The thick, black lines denote the subtracted propagator S_h and the thin, red lines the propagator from the spectral decomposition of the low modes.

operator,

$$C^{\mathrm{ll}}(x_0, y_0) = \frac{1}{V} \sum_{i,j=1}^{N_{\mathrm{low}}} \sum_{\vec{x},\vec{y}} \left\{ \left[\phi_i^\dagger(x) \gamma_0 P_- \phi_j(x) \right] \left[\phi_i^\dagger(y) \gamma_0 P_- \phi_j(y) \right] \right\}. \tag{6.24}$$

The mixed contribution consists of two different pieces, cf. Figure 6.3. The diagram of type (b) is built from a subtracted propagator from 0 to x and a "low-mode propagator" from x to 0. The second diagram (c) contains a propagator from x to 0 and it is necessary to compute it with the low modes — restricted to one timeslice t_{fix} — as a source to be able to sum over $\vec{x}$. These additional $2 \times N_{\mathrm{low}}$ inversions are the most expensive part of the LMA procedure in terms of computer time. Their result is denoted by ζ_i. For the "heavy-heavy" contribution the usual subtracted propagators S_h are sufficient,

$$\zeta_i(x) \equiv \sum_y P_- S_\mathrm{h}(x, y) P_+ \gamma_0 P_- \phi_i(y) \delta(y_0 - t_{\mathrm{fix}}), \tag{6.25}$$

$$C^{\mathrm{hl}}(x_0) = \frac{1}{L^3} \sum_{i=1}^{N_{\mathrm{low}}} \sum_{\vec{x}} \left\{ \left[\phi_i^\dagger(x) \gamma_0 P_- \zeta_i(x) \right] + \left[\zeta_i^\dagger(x) \gamma_0 P_- \phi_i(x) \right] \right\}, \tag{6.26}$$

$$C^{\mathrm{hh}}(x_0) = \sum_{\vec{x}} \left[(P_- S_\mathrm{h}(x, 0) P_+)^\dagger \gamma_0 P_- S_\mathrm{h}(x, 0) P_+ \right]. \tag{6.27}$$

These subtracted propagators are the solutions of Eq. (4.9b) and are computed during the inversion with low-mode preconditioning anyway.

We stress that the decomposition (6.23) does not lead to identical results configuration by configuration. The low-mode averaged correlation function gives a statistically independent estimate and both results should agree in the limit of large statistics, that means,

$$\langle C(x_0) \rangle = \langle C(x_0)_{\mathrm{LMA}} \rangle. \tag{6.28}$$

An instructive way to visualise the benefits of LMA are plots of the Monte Carlo history of the observable — in this case the two point function C at a fixed timeslice — with and without

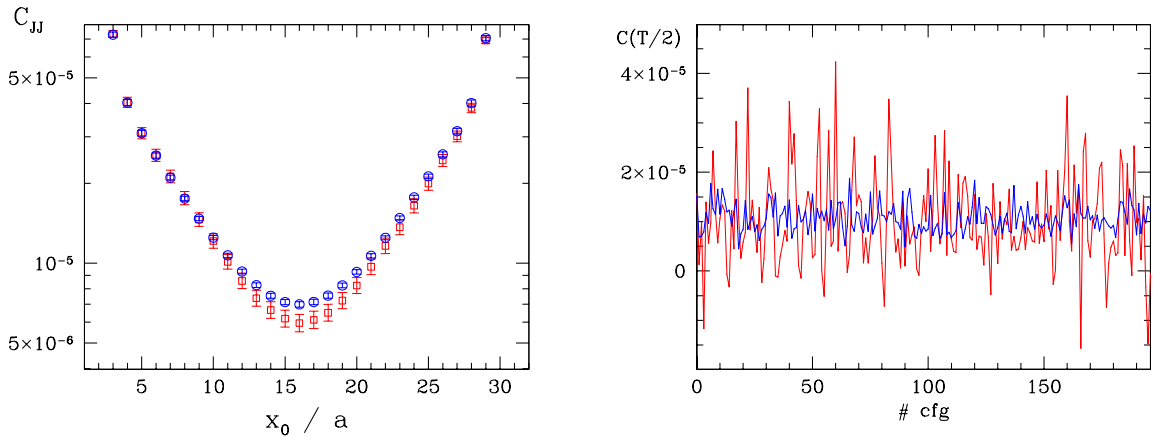

(a) Two-point function with (circles) and without LMA (squares).

(b) Monte Carlo history of $C(x_0 = T/2)$ with (blue) and without (red) LMA. The "spikyness" is clearly reduced.

Figure 6.4: Illustration of the benefits of LMA for a two-point function at a typical p-regime mass.

LMA, Figure 6.4. The effect is clearly visible, especially in the ϵ-regime where the intrinsic fluctuations are large. Results of two-point functions with LMA have been published by Giusti et al. [61] and DeGrand and Schaefer [60].

6.4.2 Three-Point Functions: Figure Eight Diagram

In studies of non-leptonic kaon decays, correlation functions of the form of C_1 (6.15) are computed on the lattice. The procedure of low-mode averaging for the corresponding diagrams is a straightforward but lengthy extension of the previous subsection. However in this case only a subset of the several contributions can be computed efficiently including a summation over the spatial coordinates at the timeslice of the four-fermion operator.

The three-point function C_1 contains a *colour-disconnected* ($C_{1\mathrm{d}}$) and a *colour-connected* contribution ($C_{1\mathrm{c}}$) corresponding to the first and second line of Eq. (6.16). We split $C_{1\mathrm{d}}$ and $C_{1\mathrm{c}}$ independently,

$$C_{1\mathrm{d/c}} = C^{\mathrm{llll}}_{1\mathrm{d/c}} + C^{\mathrm{hlll}}_{1\mathrm{d/c}} + C^{\mathrm{hhll}}_{1\mathrm{d/c}} + C^{\mathrm{hhhl}}_{1\mathrm{d/c}} + C^{\mathrm{hhhh}}_{1\mathrm{d/c}}. \tag{6.29}$$

The contribution built from low modes only are given by

$$\begin{aligned} C^{\mathrm{llll}}_{1\mathrm{d}}(x_0, y_0) = \frac{1}{V} \sum_{\vec{x},\vec{y},\vec{z}} \sum_{i,j,k,l=1}^{N_{\mathrm{low}}} \sum_{\mu=0}^{3} \Big\{ & \left[\phi_i^\dagger(x)\gamma_0 P_- \phi_j(x)\right] \left[\phi_j^\dagger(z)\gamma_\mu P_- \phi_i(z)\right] \\ & \times \left[\phi_l^\dagger(z)\gamma_\mu P_- \phi_k(z)\right] \left[\phi_k^\dagger(y)\gamma_0 P_- \phi_l(y)\right] \Big\}, \end{aligned} \tag{6.30a}$$

$$C_{1c}^{llll}(x_0,y_0) = \frac{1}{V}\sum_{\vec{x},\vec{y},\vec{z}}\sum_{i,j,k,l=1}^{N_{low}}\sum_{\mu=0}^{3}\Big\{\left[\phi_i^\dagger(x)\gamma_0 P_-\phi_j(x)\right]\left[\phi_j^\dagger(z)\gamma_\mu P_-\phi_k(z)\right] \times\left[\phi_l^\dagger(z)\gamma_\mu P_-\phi_i(z)\right]\left[\phi_k^\dagger(y)\gamma_0 P_-\phi_l(y)\right]\Big\}, \tag{6.30b}$$

where $z = (0,\vec{z})$ is the position of the operator. The mixed contributions consist of several terms,

$$C_{1d/c}^{hlll} = \frac{1}{L^3}\left[a_{1d/c}^{hlll} + b_{1d/c}^{hlll} + c_{1d/c}^{hlll} + d_{1d/c}^{hlll}\right], \tag{6.31a}$$

$$C_{1d/c}^{hhll} = a_{1d/c}^{hhll} + b_{1d/c}^{hhll} + a_{1d/c}^{hlhl} + b_{1d/c}^{hlhl} + c_{1d/c}^{hlhl} + d_{1d/c}^{hlhl}, \tag{6.31b}$$

$$C_{1d/c}^{hhhl} = \frac{1}{L^3}\left[a_{1d/c}^{hhhl} + b_{1d/c}^{hhhl} + c_{1d/c}^{hhhl} + d_{1d/c}^{hhhl}\right]. \tag{6.31c}$$

The definitions of the coefficients a–d are rather involved and given in Appendix D.1. The hhhh-term is identical to the original three-point function after exchanging S with S_h.

6.4.3 Testing the Efficiency of Low-Mode Averaging

From the experience with two-point functions in the ϵ-regime [61] it was expected that a few low modes used in LMA would be sufficient to increase the signal of the three-point functions substantially. However tests on a small lattice show that it is necessary to include more low modes in this case [107, 108]. In the p-regime $N_{low} = 5 - 10$ gives a substantial improvement, while in the ϵ-regime twenty low modes were needed to improve the signal.

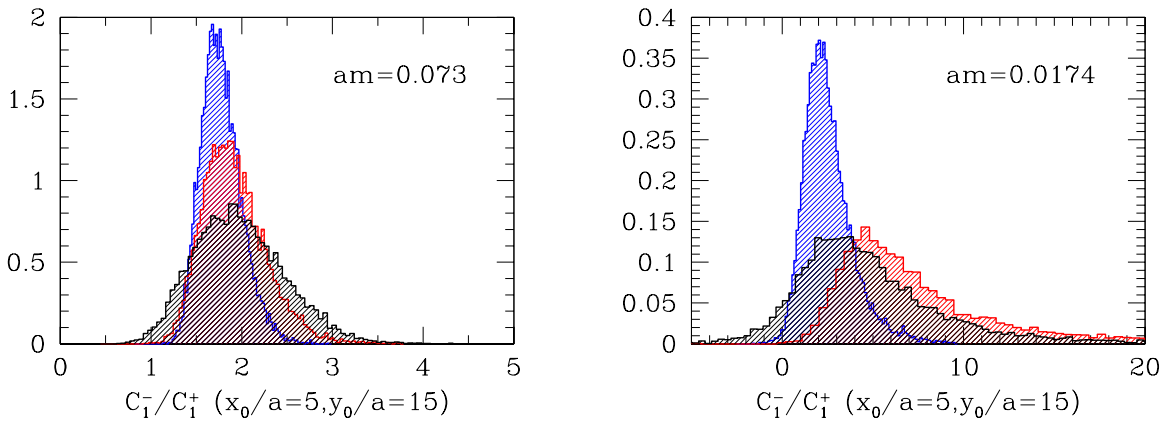

(a) C_1^-/C_1^+ for a p-regime mass.

(b) C_1^-/C_1^+ for an ϵ-regime mass.

Figure 6.5: Bootstrap distributions of the ratio of three-point functions with different numbers of low-modes used for LMA. The data sets are from a test run on a small and coarse lattice, $L/a = 8$, $T/a = 20$, $\beta = 5.8$. In the p-regime there is a monotonic gain going from 0 (black), to 8 (red) and then to 20 (blue) low modes. In the ϵ-regime there is no apparent gain for $N_{low} = 8$.

In Figure 6.5 the effect is illustrated for both kinematical regimes using bootstrap distributions of one of the three-point functions. A bootstrap distribution is generated from the original data as an estimate of the underlying probability distribution. It has the advantage to allow for non-Gaussian statistics since no assumption on the distribution is made.

With limited computational resources it is not possible to find an optimal number of low modes, but the choice $N_{\text{low}} = 20$ is an acceptable compromise between the gain in accuracy and the additional numerical effort. The results in the following sections convincingly show the need to employ LMA in an ϵ-regime calculation.

In the course of the study also the possible effect of the limited precision of the low-modes in the chirality sector with zero modes was checked. As stated in Section 4.3 it has an effect on the inversion, but here it turned out to be irrelevant.

6.4.4 Mass Dependence of the Individual Contributions

It is also helpful to consider the bootstrap distributions of the individual terms of the low-mode averaged quantity. The individual contributions to C_1 defined in Eq. (6.29) and following can also be analysed independently even though they are no physical observables. Using again bootstrap distributions to visualise the statistical signal, one can for instance compare the relative size of the llll-contributions for different numbers of low-modes and/or for quark masses in different kinematical regimes.

In a short preview of the numerical results of the next section the data sets from two lattices with $L/a = 12, 16$, $T/a = 32$ at $\beta = 5.8485$ are analysed. The relative importance of the contributions changes with the mass. In Figure 6.6 the statistical signal on the larger lattice of the terms contributing to C_{1d} is studied for a rather heavy quark mass (l.h.s.) and an almost vanishing quark mass (r.h.s). The dominating contribution in the ϵ-regime is — as expected — the pure low-mode contribution. In the p-regime all five terms are significantly different from zero and the mixed contributions are even larger than the llll-term. The hhhh-term is not shown for the ϵ-regime plot because it is two orders of magnitude smaller than the other terms and therefore does not contribute to the signal.

The explicit dependence on the topological charge, which is a unique feature of the ϵ-regime, can also be made visible. In Figure 6.7 the bootstrap distribution of the llll-term is plotted for several ensembles with fixed topological index. The signal is clearly getting better with increasing $|\nu|$ even though the number of configurations is decreasing. The probability to generate configurations with higher topological charge is suppressed, because it follows a Gaussian distribution as will be explained in more detail in Subsection 6.5.3. The influence of ν on the signal is more pronounced on the smaller lattice and can be understood by considering the distributions of the lowest eigenvalues. For larger $|\nu|$ they are pushed further away from the origin, [75].

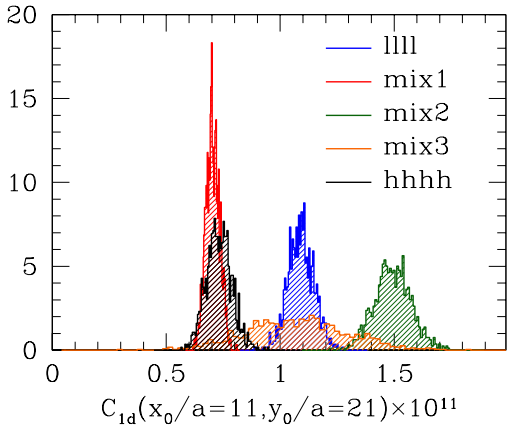

(a) Distributions for a p-regime quark mass. The topological charge is unrestricted.

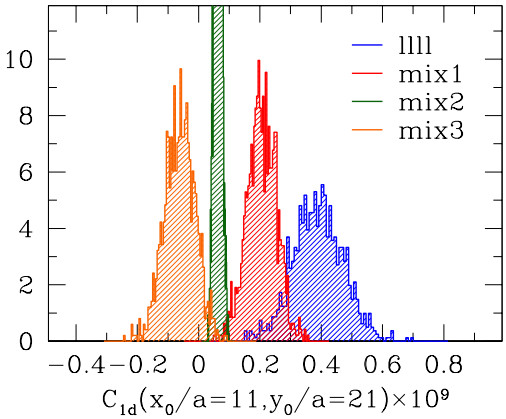

(b) Distributions for an ϵ-regime quark mass and $|\nu| = 3$.

Figure 6.6: Bootstrap distributions of the different terms contributing to the low-mode averaged three-point function C_{1d} at fixed (x_0, y_0). The relative size of the contributions changes in different kinematical regimes.

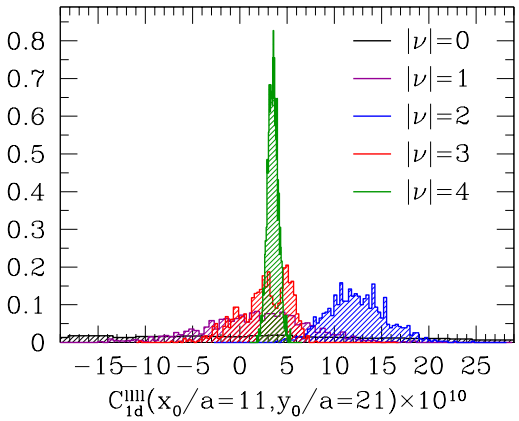

(a) C_{1d}^{llll} for different values of the index on the $12^3 \times 32$ lattice.

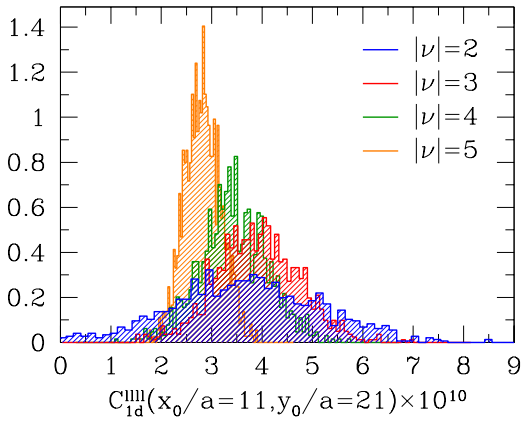

(b) C_{1d}^{llll} for different values of the index on the $16^3 \times 32$ lattice.

Figure 6.7: Bootstrap distributions of the llll-contribution to the low-mode averaged three-point function C_{1d} at fixed (x_0, y_0) and quark masses in the ϵ-regime. The $|\nu|$-dependence is clearly visible in both volumes, but the effect is stronger in the smaller volume (left). The sectors $|\nu| = 0, 1$ have not been considered on the larger lattice because of the experience gained at $L/a = 12$.

6.5 Numerical Results

6.5.1 Lattice Setup

The general setup for the numerical computation is similar to the one described in Section 5.1. Since the observables require a larger physical volume the project is limited to one bare coupling ($\beta = 5.8485$) which corresponds to a lattice spacing of 0.125 fm. Two different spacial volumes are considered, $L/a = 12$ and 16 at fixed $T/a = 32$. The ϵ-regime formulae depend explicitly on the aspect ratio $\rho = T/L$ and show better convergence for $\rho \sim 1$. The quark

label	β	L/a	T/a	a [fm]	#cfgs	quark mass am
A	5.8485	12	32	0.124	681	0.003, 0.005, 0.007, 0.040
B	5.8485	16	32	0.124	827	0.002, 0.003, 0.020, 0.030, 0.040, 0.060

Table 6.1: Simulation parameters for the study of non-leptonic kaon decays.

masses are picked to lie safely in both regimes. In the ϵ-regime only a few values are needed because the results are basically independent of the quark mass once it is small enough, where "small" means essentially $\mu \equiv m\Sigma V < 1$. In the first run on lattice A we checked that the results are constant for the three lower masses and scaled two of them to keep the same μ on lattice B. For the p-regime we concentrate on lattice B where the finite volume effects are smaller and added four heavier quark masses which reach from kaon mass downwards.

6.5.2 Fitting Ratios of Three-Point Functions

Since both data sets have the same time extent, we pick one of them (lattice B) to investigate the dependence of the results on the details of the fitting procedure.

The ChPT expectation for the ratios R^- and R^+ is that they approach a constant sufficiently far away from the insertion points of the currents (x_0, y_0) and the four-fermion operator at the origin. Following this assumption the fits to a constant are performed using all pairs (x_0, y_0) which satisfy

$$x_0, T - x_0, T - y_0, |y_0 - x_0|, \geq t_{\min}. \tag{6.32}$$

In Figure 6.8 the dependence of the results for the two ratios on $t_{\min}$ are shown. The effect is rather small in the p-regime. In the ϵ-regime the signal is lost for some topological sectors if $t_{\min}$ is decreased. The best value to allow which can be used in both regimes is $t_{\min}/a = 9$. For $T/a = 32$ this means that 42 points contribute to the fit, which leaves some room for reducing T/a in a future run to save computer time.

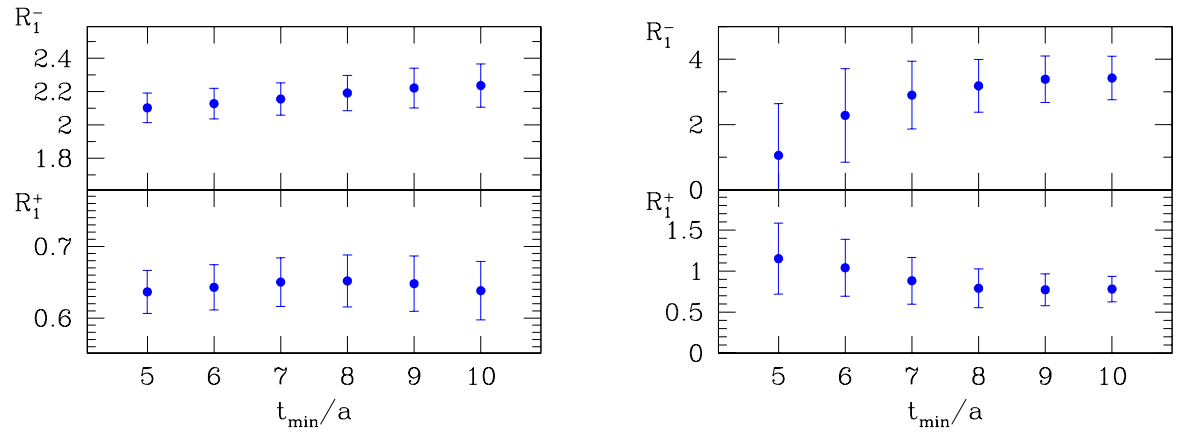

(a) p-regime data, $am = 0.02$.

(b) ϵ-regime data, $|\nu| = 3$, $am = 0.002$.

Figure 6.8: Comparison of different fit intervals used for the constant fits to the ratios R_1^+ and R_1^-. The value of t_{min} determines the minimal distance between operator insertions.

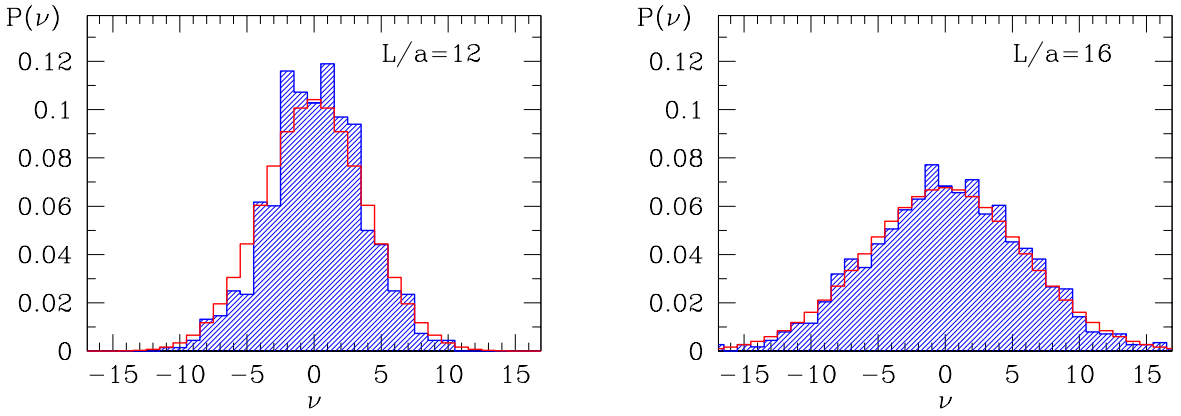

(a) L/a=12, 681 configurations

(b) L/a=16, 1127 configurations

Figure 6.9: Measured (blue) and expected (red) index distribution on the two lattices. The large volume limit describes the data well reasonably well in both cases.

6.5.3 ϵ-Regime: Weighted Averages

Chiral Perturbation Theory (ChPT) in a small volume depends explicitly on the constant zero mode field U_0 [57]. This leads to a dependence on the topological index ν, cf. Section 3.3. A matching of ChPT and QCD in a small volume therefore requires the computation of expectation values in QCD at fixed topology, denoted by $\langle \ldots \rangle_\nu$. The results for several νs can afterwards be combined in a joint fit. Our considered ratios of three- and two-point functions are independent of ν in NLO ϵ-regime CHPT [62] . So we fit the results as a constant constant against ν.

The interval of the *weighted averages* is restricted due to practical limitations. The lowest topological sectors suffer from extreme statistical fluctuations, as already seen in Subsection 6.4.4. It has been observed that index 0 and ±1 do not contribute to the weighted average at all, because the large fluctuation lead to a suppression of their weight in the fitting procedure. Therefore we exclude these sectors from the beginning on the larger lattice. For larger $|\nu|$ the number of configurations decreases rapidly since its probability distribution in the large volume limit reads [75]

$$P_\nu = \frac{1}{\sqrt{2\pi \langle \nu^2 \rangle}} \exp\left(-\frac{\nu^2}{2\langle \nu^2 \rangle}\right). \tag{6.33}$$

In Figure 6.9 the distribution of the topological charge is shown for the both lattices together with the predicted distribution (6.33) at $\beta = 5.8458$ using $r_0^4\chi = 0.00715(22)$ [109], which corresponds to $\sqrt{\langle \nu^2 \rangle} = 5.89$ on the larger lattice. We decided to use data up to $|\nu| = 8$ on both lattices for the final results. The results for one mass on lattice B are given in Table 6.2. The complete data sets which are summarised in Figure 6.10 can be found in Appendix D.2. It is not expected that the results on the two lattices agree because of different finite volume corrections which will be explained in Section 6.7.

$\lvert\nu\rvert$	# cfgs	R^+	R^-	R^-/R^+	R^+/R^-
2	151	0.54(17)(15)	2.14(73)(65)	4.0(2.3)(1.3)	0.25(14)(9)
3	130	0.80(12)(13)	3.53(56)(58)	4.4(1.1)(0.8)	0.227(52)(42)
4	125	0.68(12)(11)	3.35(42)(44)	5.0(1.4)(0.9)	0.204(48)(39)
5	101	0.67(11)(10)	1.99(65)(75)	3.0(1.0)(1.1)	0.35(20)(10)
6	87	0.608(93)(86)	2.15(30)(35)	3.56(73)(67)	0.286(73)(48)
7	86	0.55(10)(11)	2.61(25)(27)	4.8(1.4)(0.8)	0.212(48)(45)
8	66	0.53(13)(11)	2.14(29)(26)	4.1(1.4)(1.0)	0.250(75)(58)
9	32	0.36(11)(11)	2.63(60)(60)	7.7(5.2)(3.1)	0.142(83)(52)
10	29	0.57(10)(10)	1.89(41)(49)	3.4(1.1)(0.9)	0.31(14)(7)
2-8	w.a.	0.625(43)(45)	2.47(14)(14)	4.04(44)(44)	0.233(24)(24)
	χ^2	0.70	2.08	0.83	1.11

Table 6.2: Results for the ratio defined in Eq. (6.18) on the $16^3 \times 32$ lattice at $am = 0.003$. The first error is the upper and the second the lower bootstrap error.

The presented results show that it is possible to fit the ratios to a constant in ν on both lattices with a reasonable χ^2. But it is also clearly visible that the results on the larger lattice have less fluctuations. There is also less dependence on the choice of the procedure. The product of $R^\mp$ and $R^\pm$ is much closer to one than on lattice A where it is around 0.7.

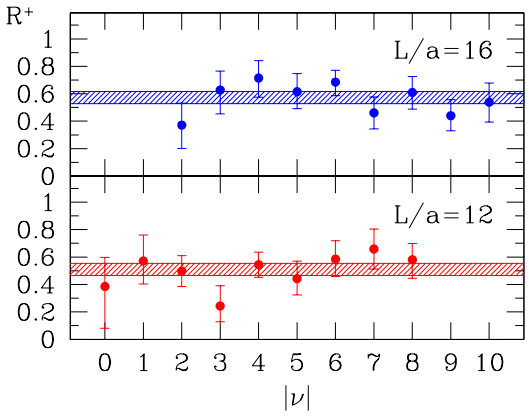

(a) R_+.

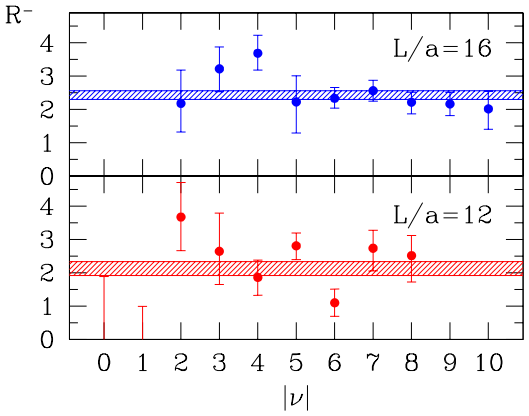

(b) R_-.

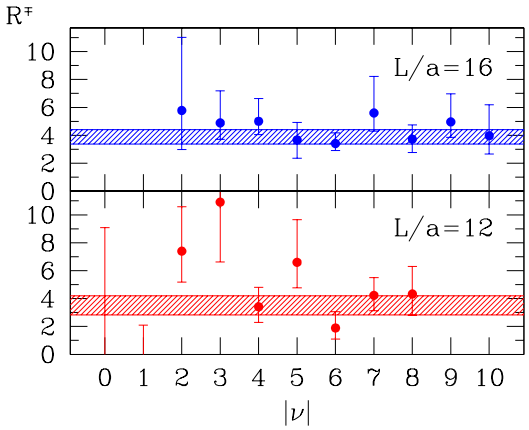

(c) R_-/R_+.

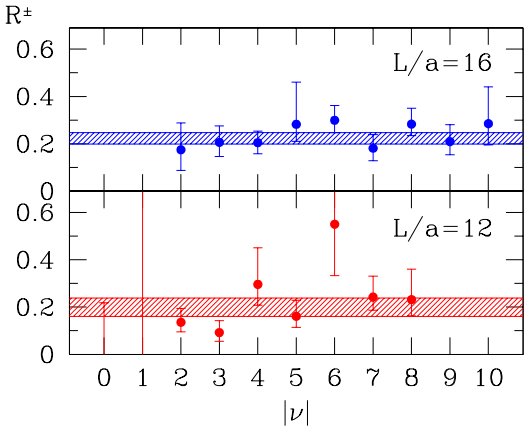

(d) R_+/R_-.

Figure 6.10: Weighted averages at $L/a = 12$ (red) and $L/a = 16$ (blue) in the ϵ-regime. The quark mass is in both cases such that $m\Sigma V \approx 1$.

6.5.4 p-Regime: Full Ensemble

The analysis of the p-regime data is done for the whole ensemble of configuration. The splitting according to the topological index is not necessary. The interesting feature here is the mass dependence. The ratios R^- and R^+ are relatively close to each other at the kaon mass. The enhancement appears towards the chiral limit where R^+ bends down and R^- bends up, Figure 6.11. One can see how nicely low-mode averaging helps to keep the fluctuations under control when going to smaller quark masses.

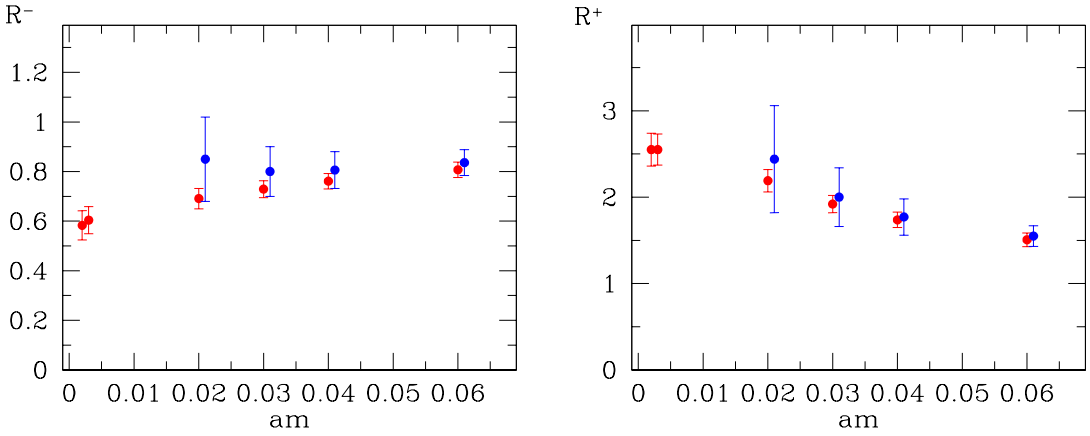

(a) The ratio R^+ as a function of the bare quark mass.

(b) The ratio R^- as a function of the bare quark mass.

Figure 6.11: Mass dependence of the bare ratios at $L/a = 16$. The physical Kaon mass coincides with the rightmost point. The red points denote the results with LMA while the blue points which are slightly displaced for better visibility show the results without LMA.

The numerical results with LMA for the ratios together with the result on the pseudoscalar mass from the two-point function are summarised in Table 6.3.

am	am_P	R^+	R^-	R^-/R^+	R^+/R^-
0.020	0.1970(25)	0.648(39)	2.22(12)	3.42(26)	0.291(22)
0.030	0.2309(23)	0.687(32)	1.949(95)	2.83(19)	0.352(23)
0.040	0.2603(23)	0.720(31)	1.760(84)	2.44(15)	0.409(25)
0.060	0.3111(24)	0.771(30)	1.516(75)	1.96(11)	0.509(28)

Table 6.3: Results in the p-regime on the $16^3 \times 32$ lattice. The reference point in lattice units corresponds to $am_\mathrm{K} = 0.310$ which agrees with the heaviest mass very well. The fitting procedure is described in Subsection 6.5.2.

6.6 Renormalisation of Four-Fermion Operators

The bare operators $Q_1^\pm$ (6.8) must be renormalised to relate their correlation functions to physical amplitudes. The numerical results of the following section will be published in [110].

In principle the operators $Q_1^\pm$ and $Q_2^\pm$ mix under renormalisation also in the continuum. Since the regularisation with Ginsparg-Wilson fermions preserves chiral symmetry the pattern stays the same on the lattice,

$$\begin{pmatrix} Q_1^\pm \\ Q_2^\pm \end{pmatrix} = \begin{pmatrix} Z_{11} & Z_{12} \\ Z_{21} & Z_{22} \end{pmatrix} \begin{pmatrix} Q_1^{\pm,\mathrm{bare}} \\ Q_2^{\pm,\mathrm{bare}} \end{pmatrix}. \tag{6.34}$$

But since the operator does not contribute to physical matrix elements[2] its effect is usually neglected [62] and in the SU(4) case Q_2 does not appear at all.

Two separate ways to renormalise Q_1 with an intermediate scheme S are described in the following. The renormalisation group invariant (RGI) operator is related to the bare one through,

$$\frac{\langle Q_1^- \rangle_{\mathrm{RGI}}}{\langle Q_1^+ \rangle_{\mathrm{RGI}}} = \frac{c_{\mathrm{x}}^-(\mu/\Lambda)}{c_{\mathrm{x}}^+(\mu/\Lambda)} \cdot \frac{\langle Q_1^-(\mu) \rangle_{\mathrm{x}}}{\langle Q_1^+(\mu) \rangle_{\mathrm{x}}} = \frac{c_{\mathrm{x}}^-(\mu/\Lambda)}{c_{\mathrm{x}}^+(\mu/\Lambda)} \cdot \frac{Z_{\mathrm{x}}^-(g_0, a\mu)}{Z_{\mathrm{x}}^+(g_0, a\mu)} \cdot \frac{\langle Q_1^-(a) \rangle_{\mathrm{bare}}}{\langle Q_1^+(a) \rangle_{\mathrm{bare}}}. \tag{6.35}$$

The notation will be explained in the following.

6.6.1 RG Running and Wilson Coefficients

The coefficients $c_{\mathrm{x}}^\pm(\mu/\Lambda)$ contain the RG evolution from the high scale M_W down to μ in the particular scheme. The factor $Z_{\mathrm{x}}^\pm(g_0, a\mu)$ relates the bare operator matrix element in the lattice regularised theory to the scheme x. Since the dependence on x and its scale μ drops out, it is convenient to define the overall renormalisation factor as,

$$\mathcal{Z}^{-+}(g_0) \equiv \frac{c_{\mathrm{x}}^-(\mu/\Lambda)}{c_{\mathrm{x}}^+(\mu/\Lambda)} \cdot \frac{Z_{\mathrm{x}}^-(g_0, a\mu)}{Z_{\mathrm{x}}^+(g_0, a\mu)}. \tag{6.36}$$

The exact solution of the RG equation for $c_{\mathrm{x}}^\pm$ yields,

$$c_{\mathrm{x}}^\pm(\mu/\lambda) = \left[2b_0\overline{g}^2(\mu)\right]^{\gamma_0^\pm/2b_0} \exp\left\{ -\int_0^{\overline{g}(\mu)} \mathrm{d}g \left[\frac{\gamma^\pm(g)}{\beta(g)} + \frac{\gamma_0^\pm}{b_0 g} \right] \right\}. \tag{6.37}$$

Here β is the renormalisation group function and γ the anomalous dimension of the operator defined in Appendix B. The solution (6.37) can be expanded in the scheme x and for the ratio at two loops one gets,

$$\frac{c_{\mathrm{x}}^-(\mu/\Lambda)}{c_{\mathrm{x}}^+(\mu/\Lambda)} = \left[2b_0\overline{g}^2(\mu)\right]^{\Delta\gamma_0/2b_0} \left\{ 1 + \frac{1}{2b_0^2} \left(b_0 \Delta\gamma_1^{\mathrm{x}} - b_1 \Delta\gamma_0 \right) \overline{g}^2 \mu + O\left(\overline{g}^4\right) \right\}, \tag{6.38}$$

[2] Correlation functions of $Q_2^\pm$ with the same total momentum in the initial and final state vanish.

where $\Delta\gamma_i^{\mathrm{x}} \equiv (\gamma_i^+)_{\mathrm{x}} - (\gamma_i^-)_{\mathrm{x}}$.

The matching between QCD and Chiral Perturbation Theory is done for the ratio of three-point functions,

$$\frac{g_1^-}{g_1^+} \cdot \frac{\mathcal{C}_1^-(x_0,y_0)}{\mathcal{C}_1^+(x_0,y_0)} = \frac{k_1^-}{k_1^+} \cdot \mathcal{Z}^{-+} \cdot \frac{C_1^-(x_0,y_0)}{C_1^+(x_0,y_0)}. \tag{6.39}$$

In order to extract the ratio of LECs g_1^-/g_1^+, the ratio of Wilson coefficients k_1^-/k_1^+ is needed. Since they are evaluated at the high scale M_W they are also perturbative quantities. The one-loop expression for the ratio of Wilson coefficients reads [111]

$$\begin{aligned}\frac{k_1^-(M_W/\Lambda)}{k_1^+(M_W/\Lambda)} = \left[2b_0\overline{g}^2(M_W)\right]^{-\Delta\gamma_0/2b_0} \Bigg\{ 1 - \frac{1}{2b_0^2}\left(b_0\Delta\gamma_1^{\mathrm{x}} - b_1\Delta\gamma_0\right)\overline{g}^2(M_W) \\ + \Delta h_1^{\mathrm{x}}\overline{g}^2(M_W) + \mathrm{O}\big(\overline{g}^4\big) \Bigg\},\end{aligned} \tag{6.40}$$

where the combination $(\gamma_1^\tau)_{\mathrm{x}} - 2b_0(h_1^\tau)_{\mathrm{x}}$ is scheme independent. The coefficients h_1^τ are also listed in Appendix B. Inferring the gauge coupling from the two-loop formula

$$\overline{g}^2(\mu) = \frac{1}{b_0 t} - \frac{b_1 \ln t}{b_0^3 t^2} + \mathrm{O}\big(t^{-3}\big), \quad t = \ln(\mu^2/\Lambda^2) \tag{6.41}$$

and using $\Lambda_{\overline{\mathrm{MS}}} = 238\,\mathrm{MeV}$ [89] for $N_{\mathrm{f}} = 0$ the numerical values for the NLO RG evolution factors $c^\pm$ in the RI-MOM scheme at $\mu = 2\,\mathrm{GeV}$ and the Wilson coefficients are

$$c_{\mathrm{RI}}^-(\mu/\Lambda) = 0.6259, \qquad c_{\mathrm{RI}}^+(\mu/\Lambda) = 1.2735, \qquad c_{\mathrm{RI}}^-/c_{\mathrm{RI}}^+ = 0.4889, \tag{6.42}$$

$$k^-(M_W/\Lambda) = 1.9775, \qquad k^+(M_W/\Lambda) = 0.7080, \qquad k_1^-/k_1^+ = 2.7918. \tag{6.43}$$

6.6.2 Perturbative Matching to the RI-MOM Scheme

The first considered scheme is the RI-MOM scheme, which was introduced in [91]. It is scheme for non-perturbative renormalisation, in which the renormalisation conditions are imposed on the quark and gluon Green functions between off-shell external states in a fixed gauge. The scheme can also be evaluated perturbatively. The quoted results can be found in [95].

The renormalisation factor for the four-fermion operator Q_1^τ in this scheme reads,

$$\begin{aligned}Z_{\mathrm{RI}}^\tau(g_0,a\mu) = 1 - \frac{g_0^2}{16\pi^2}\Bigg[\tau\frac{N_c-\tau}{N_c}3\ln(16(a\mu)^2) + \frac{(N_c-\tau)(N_c+2\tau)}{N_c}B_V \\ - \tau\frac{N_c-\tau}{N_c}B_S - 2C_F B_\psi\Bigg] + \mathrm{O}\big(g_0^4\big)\,.\end{aligned} \tag{6.44}$$

The coefficients B_S, B_V and B_ψ are tabulated in [95]. For the Neuberger operator with $s = 0.4$ one gets,

$$B_\psi = -18.97397, \quad B_S = 5.55135, \quad B_V = 1.55601. \tag{6.45}$$

The expressions for the ratios are simpler, the term stemming from the wave function renormalisation drops out,

$$\frac{Z^-_{\mathrm{RI}}(g_0, a\mu)}{Z^+_{\mathrm{RI}}(g_0, a\mu)} = 1 + \frac{g_0^2}{(4\pi)^2}\left[12\ln(4a\mu) - 2(B_S - B_V)\right] + \mathrm{O}\big(g_0^4\big)\,, \tag{6.46a}$$

$$\frac{Z^+_{\mathrm{RI}}(g_0, a\mu)}{Z_A^2(g_0,)} = 1 - \frac{g_0^2}{(4\pi)^2}\left[4\ln(4a\mu) - \frac{2}{3}(B_S - B_V)\right] + \mathrm{O}\big(g_0^4\big)\,, \tag{6.46b}$$

$$\frac{Z^-_{\mathrm{RI}}(g_0, a\mu)}{Z_2^2(g_0)} = 1 + \frac{g_0^2}{(4\pi)^2}\left[8\ln(4a\mu) - \frac{4}{3}(B_S - B_V)\right] + \mathrm{O}\big(g_0^4\big)\,. \tag{6.46c}$$

6.6.3 Mean Field Improvement

The idea of mean field improvement (MFI) has already been discussed briefly in Subsection 5.1.3. Its application to the perturbative renormalisation of the four quark operator $Q_1^\pm$ is summarised in the following.

For a general n-quark operator with a perturbative renormalisation factor

$$Z_{\mathcal{O}_n} = 1 + g_0^2 z^{(1)}_{\mathcal{O}_n} + \mathrm{O}\big(g_0^4\big)\,, \tag{6.47}$$

the MFI version reads [110]

$$Z^{\mathrm{mfi}}_{\mathcal{O}_n} = \left(\frac{\rho}{\tilde{\rho}}\right)^{n/2}\left\{1 + \tilde{g}^2\left[z^{(1)}_{\mathcal{O}_n} - \frac{n}{2}\frac{\rho - 4}{\rho}u_0^{(1)}\right] + \mathrm{O}\big(g_0^4\big)\right\}. \tag{6.48}$$

One can see that in the ratio Z_1^-/Z_1^+ the prefactor and the term proportional to $u_0^{(1)}$ drop out. Therefore it is sufficient to replace the bare coupling with $\tilde{g}^2$ which is set to $\overline{g}^2_{\overline{\mathrm{MS}}}$. As expected from these considerations the effect of MFI is smaller in this case than for Z_{S} in Chapter 5. The actual values for the renormalisation factors are given in Table 6.5 together with a non-perturbative estimate.

6.6.4 Non-Perturbative Renormalisation

The idea how to obtain $Z_1^\pm$ non-perturbatively follows the lines of Section 5.1. An independent lattice results is matched to the bare ratio $R_1^\pm$ at a reference scale. The relevant scale is again the kaon mass, $x_{\mathrm{ref}} = (r_0 m_K)^2 = 1.5736$. The ALPHA collaboration has published results on R_1^+ in a quenched study on the kaon B-parameter using two different twisted mass regularisations [103]. Since their final result is in the continuum limit, it is independent of the regularisation. The corresponding results for the ratio R_1^- will be published in [110].

The renormalisation procedure assumes that the scheme is mass independent. So that the Z-factor in the chiral limit coincides with the one at the reference point. The matching condition

$$Z_1^\pm = \frac{R_1^\pm\big|_{x_{\mathrm{ref}}}}{R^\pm_{\mathrm{tm,\,CL}}\big|_{x_{\mathrm{ref}}}}, \tag{6.49}$$

also implies, that our result for the renormalised quantities at the physical point will always coincide with the ALPHA result. Since our main result is the value of the considered ratios in the chiral limit the loss of predictivity is acceptable.

In Table 6.4 the bare overlap ratios and the renormalised continuum twisted mass ratios are summarised. Table 6.5 contains the resulting Z-factor from the matching together with

	β	$r_0 m_{\mathrm{P}}$	R_1^-	R_1^+	R_1^+/R_1^-
overlap	5.8485	1.259(10)	0.772(30)	1.514(73)	0.511(28)
twisted mass	∞	1.2544	0.954(52)	0.910(76)	0.925(79)

Table 6.4: Results for the ratios with overlap and twisted mass fermions [110].

the analogues from bare and mean field improved perturbation theory. The main observation here is that the difference between perturbative and non-perturbative renormalisations is very small, the values are almost consistent. This is in stark contrast to the case of the condensate (Chapter 5) and suggests that lattice artefacts are already small at this coarse lattice spacing due to cancellations in the ratios.

	Z^+/Z_A^2	Z^-/Z_A^2	Z^-/Z^+
bare P.T.	1.242	0.657	0.525
MFI P.T.	1.193	0.705	0.582
non-perturbative	1.236(83)	0.601(58)	0.552(56)

Table 6.5: Summary of the relevant renormalisation factors.

6.7 Chiral Corrections

The usual Chiral Perturbation Theory can be extended to include hadronic weak decays via an effective four-fermion vertex. For the standard formulation of ChPT this has been done Bernard et al. [101]. In the special case of the ϵ-regime we quote results from [62].

We repeat the definition of the effective Hamiltonian

$$\mathcal{H}_{\mathrm{w}} = \frac{g_{\mathrm{w}}^2}{4M_W^2} V_{us}^* V_{ud} \left\{ g_1^+ \mathcal{Q}_1^+ + g_1^- \mathcal{Q}_1^- \right\}, \tag{6.50}$$

which contains the operator

$$\mathcal{Q}_1^\pm = \frac{F^2}{4} \left\{ (U\partial_\mu U^\dagger)_{us} (U\partial_\mu U^\dagger)_{du} \pm (U\partial_\mu U^\dagger)_{ds} (U\partial_\mu U^\dagger)_{uu} - \left[u \to c \right] \right\}. \tag{6.51}$$

The basic concepts of the ϵ-regime calculation have been explained in Section 3.3. For the three-point function C_1^σ one gets at next-to-leading order,

$$\mathcal{C}_1^\sigma(x_0,y_0) = \frac{F^4}{8T^2}\Bigg\{1+\frac{\rho^3}{F^2T^2}\Big[2\sigma(\beta_1\rho^{-\frac{3}{2}}-k_{00}) + 2\mu C_\nu^{\text{quen}}(\mu)\big(h_1(x_0/T)+h_1(y_0/T)\big)\Big]\Bigg\}, \tag{6.52}$$

where $\rho = T/L$, $C_\nu^{\text{quen}} = 1/N\,\langle \operatorname{Re}\operatorname{Tr} U_0\rangle_\nu$ and h_1 defined in (E.4a). The *shape coefficients* which depend only on the *aspect ratio* ρ can be found in [58, 62]. For $\rho = 2$, one gets $\beta_1 = 0.08360$ and $k_{00} = 0.08331$. Together with the result for the two-point function $\mathcal{C}$,

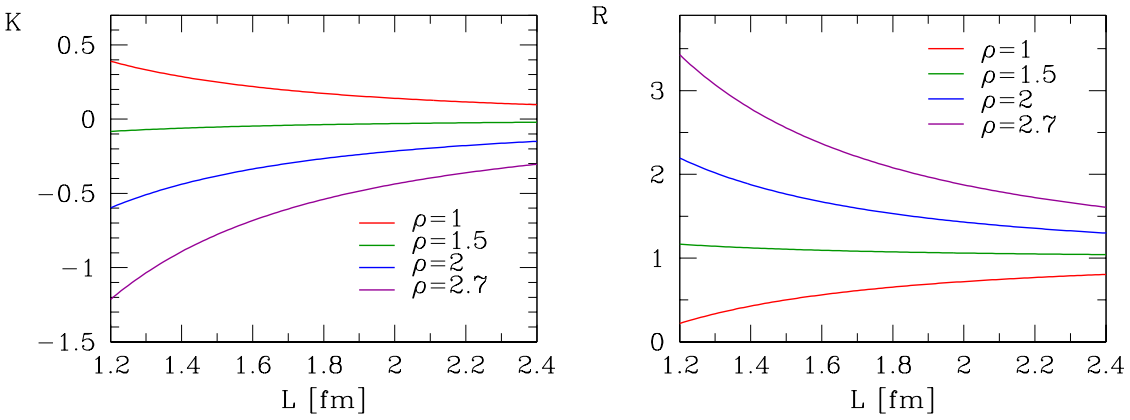

(a) Chiral correction factor K (6.57).

(b) Correction factor to the ratio of three-point functions.

Figure 6.12: Finite volume behaviour of NLO ChPT results for the normalised $K \to \pi$ matrix elements in the chiral limit. The dependence on the lattice size in physical units is plotted. ρ denotes the aspect ratio T/L.

$$\mathcal{C}(x_0) = \frac{F^2}{2T}\left[1+2\frac{\mu T^2}{F^2V}\sigma_\nu(\mu)h_1\left(\frac{x_0}{T}\right)\right], \tag{6.53}$$

the ratio

$$\mathcal{R}_\nu^\sigma \equiv \frac{\mathcal{C}_1^\sigma(x_0,y_0)}{\mathcal{C}(x_0)\cdot\mathcal{C}(y_0)}, \tag{6.54}$$

$$\to \frac{g_1^\sigma}{2}\left[1+\sigma\frac{2\rho^3}{F^2T^2}\left(\beta_1\rho^{-3/2}-k_{00}\right)\right], \tag{6.55}$$

goes to a constant sufficiently far away from the operator insertions at this order in ChPT. The subscript ν indicates that the above result holds at fixed topology. Finally one gets for the ratio of three-point functions

$$\frac{\mathcal{R}_\nu^-}{\mathcal{R}_\nu^+} = \frac{g_1^-}{g_1^+}\left\{1-\frac{4\rho^3}{F^2T^2}\left(\beta_1\rho^{-\frac{3}{2}}-k_{00}\right)\right\}. \tag{6.56}$$

The correction factors

$$K \equiv \frac{2\rho^3}{F^2T^2}\left(\beta_1\rho^{-3/2} - k_{00}\right), \qquad R \equiv 1 - 2K, \tag{6.57}$$

can be plotted as a function of the lattice size L for typical values of ρ, Figure 6.12. R is the chiral correction to $\mathcal{R}_\nu^-/\mathcal{R}_\nu^+$ and is of of the order of 40% for $T = 2\text{fm}$ and $\rho = 2$.

Clearly the result in ϵ-regime ChPT is only valid for aspect rations close to one. For very asymmetric lattices the underlying assumption that the zero mode dominates and modes with non-vanishing momentum can be treated as perturbations breaks down. An important advantage of a matching in the ϵ-regime is that it can be done at NLO without new unknown low-energy constants which would appear in the p-regime.

6.8 Resulting Low-Energy Constants

The matching of the lattice QCD results and ChPT can in principle be done by inserting both results in

$$\frac{g_1^-}{g_1^+} \cdot \frac{\mathcal{C}_1^-(x_0,y_0)}{\mathcal{C}_1^+(x_0,y_0)} = \frac{k_1^-}{k_1^+} \cdot \frac{Z_1^-}{Z_1^+} \cdot \frac{C_1^-(x_0,y_0)}{C_1^+(x_0,y_0)}. \tag{6.58}$$

The problem is that the results in the ϵ-regime cannot easily be combined with a chiral extrapolation of the p-regime data. A possible workaround is presented in the following.

6.8.1 Fitting Strategies

A quick comparison of the results on the lattices A and B shows that the NLO expression in the ϵ-regime (6.56) overestimates the volume dependence by far. Another hint in the same direction is that fits of the ratios $R^\pm$ including both p- and ϵ-regime results with chiral corrections are difficult to perform. One could now go back one step and use just the LO "corrections" which would mean to take the results in finite volume at face value. A more sophisticated way which takes the corrections into account is to consider certain combinations of R^+ and R^-. The mass (and volume) dependence of the correction takes the form

$$R^\pm(m) = g_1^\pm\left(1 + K^\pm(m)\right). \tag{6.59}$$

At NLO the correction has the opposite sign for the two ratios in the ϵ-regime,

$$K^-_{\text{NLO}} = -K^+_{\text{NLO}}. \tag{6.60}$$

Therefore the sum of the ratios has only NNLO correction, which are not known. But these are not necessarily small since it is already known that the higher orders have to cancel almost all of the NLO contribution.

Now the idea of considering the sum of ratios can be generalised. One introduces

$$P(m) = \frac{R^+(m)}{2\alpha^+} + \frac{R^-(m)}{2\alpha^-}, \tag{6.61}$$

where $\alpha^{\pm}$ are fit parameters. They are fixed by demanding $P(m) = 1$ for all masses. In Figure 6.13a $P(m)$ is plotted as a function of the quark mass, with

$$\alpha^{+} = 0.566(58), \quad \alpha^{-} = 2.50(38), \tag{6.62}$$

from a fit to all available masses. The remaining mass dependence is well within the statistical accuracy.

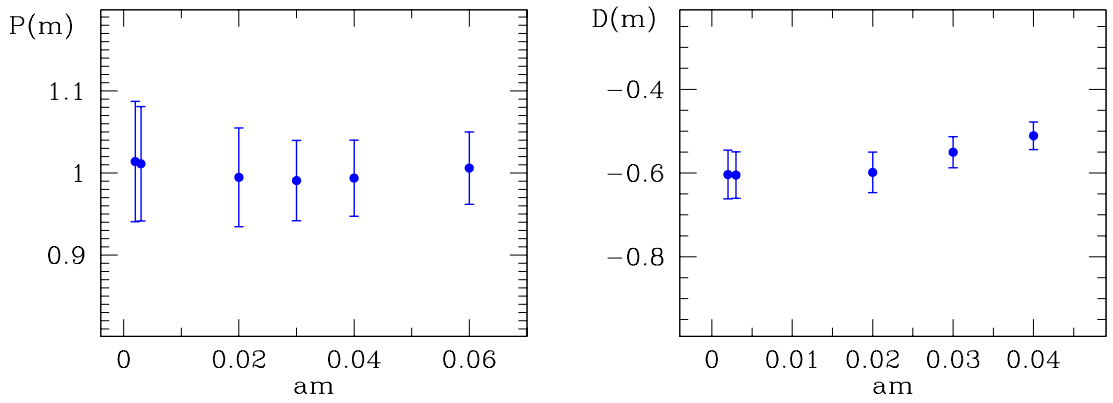

(a) $P(m)$, the combination of R_1^+ and R_1^- defined in (6.61) as a function of the bare quark mass.

(b) Double ratio $D(m)$ (6.64) as a function of the bare quark mass.

Figure 6.13: Remaining mass dependence of the ratios $P(m)$ and $D(m)$.

Combining the fit parameters (6.62) with the non-perturbative renormalisation factors from Table 6.5 and the Wilson coefficients (6.43) we quote as our final result

$$g_1^+ = 0.495(51), \quad g_1^- = 2.97(45), \quad g_1^-/g_1^+ = 6.0(1.1). \tag{6.63}$$

The error — 18% on the ratio — covers the systematic uncertainty due to the unknown higher orders in ChPT and the choice of the fit procedure. The values differ slightly from those in our publication [112] because of a preliminary set of renormalisation constants used here.

The assumption concerning the mass dependence can be checked with the double ratio

$$D(m) \equiv \frac{R^+(m) - R^+(m_{\text{ref}})}{R^-(m) - R^-(m_{\text{ref}})} \cdot \frac{R^-(m)}{R^+(m)}. \tag{6.64}$$

We take the heaviest mass as reference point for the computation of $D(m)$. From $D(m)$ being approximately mass independent, Figure 6.13b, follows the correction factors K^+ and K^- must be proportional up to a constant.

6.8.2 Comparison with Experiment

The amplitudes defined in Eq. (6.2) are related to the low-energy constants at leading order through [62]

$$\frac{A_0}{A_2} = \frac{1}{\sqrt{2}} \left(\frac{1}{2} + \frac{3}{2} \frac{g^-}{g^+} \right). \tag{6.65}$$

Therefore the result for the ratio of LECs (6.63) translates to

$$\frac{A_0}{A_2} = 6.7(1.2). \tag{6.66}$$

The result allows to conclude that a significant part of the enhancement in the ratio of amplitudes is caused by genuine QCD effects. There is a factor $3-4$ missing to the experimental value of $A_0/A_2 = 22.1$. But the low-energy constant g_1^+ is already very close to its phenomenological value of 0.50 [113][3]. This is reassuring since g_1^+ is not expected to change when including the effects of a heavier charm quark. To confirm the findings it will be necessary to move to the more realistic SU(3)-symmetric case. An exploratory study of this case is currently being done.

Furthermore the result is quenched and on a rather coarse lattice. But these systematic effects are most probably well covered by the large error and will be removed in the future. Smaller lattice spacings just require more computer time. And dynamical simulations are developing very fast.

[3]Please note the conventional factor of 5/3 between g_1^+ and the corresponding quantity g_{27} in the reference.

7 Zero Mode Saturation of Divergent Correlators

In this chapter an on-going project to extract physical quantities from topological zero-mode wavefunctions is described. The first section summarises the results of [114] where the idea was formulated. The main ingredient is again matching of lattice results to Chiral Perturbation Theory. In the second section we calculate the two-point correlator $\langle J^l P \rangle$ in LO ChPT with ϵ-regime power counting. The third section contains the application of the method to three-point functions, which describe $K \to \pi$ transitions via an effective four-fermion vertex. The low-energy constants are the same as in the previous chapter. The section also includes first numerical results.

7.1 The Method

Chiral fermions on the lattice allow to access the topological zero modes of the massless Dirac operator directly. Certain correlators are more and more dominated by their contribution when the chiral limit is approached. This can spoil the result and it is advisable to construct correlator which are free of zero mode contribution. One can, for instance, use the correlator of the left-handed current instead of the pseudoscalar density to compute the pseudoscalar mass.

Nevertheless the exact zero modes can still be used to extract physical quantities. The correlator

$$C_\nu^{ab}(x-y) = \left\langle P^a(x) P^b(y) \right\rangle_\nu, \quad P^a(x) = \overline{\psi}\gamma_5 T^a \psi, \tag{7.1}$$

quadratically diverges in the chiral limit. Here T^a is a generator in flavour space. With the help of the zero modes one can compute the correlator in the limit $m \to 0$ directly. The method and first results have been published by Giusti, Hernández, Laine, Weisz and Wittig [114].

In Chiral Perturbation Theory the general form of the correlator can be written as [58],

$$\mathcal{C}_\nu(x) = C + \alpha G(x) + \beta \left[G(x)\right]^2 + \gamma \int \mathrm{d}y\, G(x-y)G(y) + \epsilon\delta^{(4)}(x). \tag{7.2}$$

The propagator G is defined in (E.3a). Since the constant term C and the contact term $\epsilon\delta^{(4)}(x)$ depend also on the Gasser-Leutwyler constants L_i at NNLO, it is beneficial to consider the time derivative of C_ν to remove these terms. Now one defines

$$\lim_{m\to 0} (mV)^2 \mathcal{C}_\nu^{ab}(x) = \mathrm{Tr}[T^a T^b]\mathcal{A}_\nu(x) + \mathrm{Tr}[T^a]\,\mathrm{Tr}[T^b]\tilde{\mathcal{A}}_\nu(x). \tag{7.3}$$

The singlet contribution $\tilde{\mathcal{A}}_\nu$ only appears for the choice $T^a = T^b = 1$, while for $T^a \neq T^b$ with $\operatorname{Tr} T^a = 0$ one gets the non-singlet contribution $\mathcal{A}_\nu$.

At LO the integrated quantities $\mathcal{A}(x_0) \equiv \int \mathrm{d}^3x\, \mathcal{A}_\nu(x)$ and $\tilde{\mathcal{A}}(x_0) \equiv \int \mathrm{d}^3x\, \tilde{\mathcal{A}}_\nu(x)$ are constant and independent of F. The results for the time derivatives of $\mathcal{A}$ and $\tilde{\mathcal{A}}$ at NNLO from [114] are summarised in Appendix E.2.

On the QCD side of the computation one needs the exact zero modes of the Neuberger Dirac operator. These can be computed with the same algorithm that is used for the low-lying eigenmodes with non-vanishing eigenvalues. The additional numerical effort is relatively small.

For given zero modes $\{v_i\}$ one defines

$$A_\nu(x-y) \equiv \left\langle \sum_{i,j=1}^{|\nu|} v_j^\dagger(x) v_i(x) v_i^\dagger(y) v_j(y) \right\rangle_\nu , \tag{7.4a}$$

$$\tilde{A}_\nu(x-y) \equiv -\left\langle \sum_{i=1}^{|\nu|} v_i^\dagger(x) v_i(x) \sum_{j=1}^{|\nu|} v_j^\dagger(y) v_j(y) \right\rangle_\nu . \tag{7.4b}$$

Matching the numerical and analytical results allows to extract the low-energy constant F. The precision that can be reached with this method is limited by the available lattice data on rather small volumes. Furthermore it is not possible to increase the volume in the first place, because the convergence of Quenched Chiral Perturbation Theory deteriorates for volumes larger than about $(2\,\mathrm{fm})^4$ [114].

The situation is totally different for quantities which cannot be easily computed with standard methods. A computation of the low-energy constants of the effective theory for hadronic weak decays requires huge efforts as can be seen in the previous chapter. In the following sections it is described how to approach this problem in the framework of zero-mode saturation.

7.2 The $J^l P$-Correlator in LO ϵ-Regime ChPT

Another two-point function that is of interest is the mixed correlation function of the left-handed current and the pseudoscalar density. It is expected to diverge linearly in the chiral limit, since only the pseudoscalar density can contain contributions from topological zero modes. The left-handed current is "zero-mode free" in the sense that has been explained in the first paragraph of Subsection 5.1.2.

In the following the LO ChPT calculation for the correlator

$$\mathcal{C}_{JP}(x_0) = \int \mathrm{d}^3x\, \langle J_0^a(x) P(0) \rangle_\nu \tag{7.5}$$

is derived. It can be used to normalise matrix elements of the four-fermion operator Q_1 (6.8) in a similar way as the two-point function C (6.22) has been used in Chapter 6. The corresponding three-point functions can also be computed in the framework of zero mode saturation as will be explained in Section 7.3.

The ChPT expressions for the current and the density are

$$\mathcal{J}_\mu^a = \frac{1}{2}F^2 \operatorname{Tr}\left\{T^a\left(U\partial_\mu U^\dagger\right)\right\}, \tag{7.6a}$$

$$\mathcal{P}^a = \frac{1}{2}\Sigma \operatorname{Tr}\left\{T^a\left(U_\theta U - U^\dagger U_\theta\right)\right\}, \tag{7.6b}$$

where $U_\theta \equiv \mathrm{e}^{\mathrm{i}\theta/N_\mathrm{f}}$. The expansion in the fluctuation field $\xi(x)$ (3.8) leads to

$$\mathcal{J}_\mu^a = F \operatorname{Tr}\left\{T^a\left(-\mathrm{i}\partial_\mu\xi(x) + \frac{1}{F}\left[\xi(x), \partial_\mu\xi(x)\right] + \mathrm{O}\big(\epsilon^4\big)\right)\right\}, \tag{7.7a}$$

$$\begin{aligned}\mathcal{P}^a = \Sigma \operatorname{Tr}\Bigg\{T^a\Bigg[&\frac{1}{2}\left(U_\theta U_0 - \text{h.c.}\right) + \frac{\mathrm{i}}{F}\left(\xi U_\theta U_0 + \text{h.c.}\right)\\ &-\frac{1}{F^2}\left(\xi^2 U_\theta U_0 - \text{h.c.}\right) + \mathrm{O}\big(\epsilon^3\big)\Bigg]\Bigg\}.\end{aligned} \tag{7.7b}$$

The leading contribution to $\mathcal{J}^l\mathcal{P}$ is the $\mathrm{O}\big(\epsilon^3\big)$ term proportional to $(\partial_\mu\xi)\xi$. The $\mathrm{O}\big(\epsilon^2\big)$ term contains only one ξ-field and does not contribute. Using the notations defined in Appendix E and $\mu = m\Sigma V$ the correlator is given by

$$\begin{aligned}\left\langle \mathcal{J}_0^a(x)\mathcal{P}^b(y)\right\rangle_\nu^\mu = {}&\Sigma\partial_0^x G(x-y)\left\langle \operatorname{Re}\,\operatorname{Tr}(T^a U_0' T^b)\right\rangle_\nu^\mu\\ &-\Sigma\partial_0^y E(x-y)\left\langle \operatorname{Tr}(T^a)\operatorname{Re}\,\operatorname{Tr}(U_0' T^b)\right\rangle_\nu^\mu,\end{aligned} \tag{7.8}$$

where

$$\langle\cdots\rangle_\nu^\mu \equiv \frac{1}{Z_\nu(\mu)}\int\limits_{\mathrm{U}(N)} \mathrm{d}U_0' \cdots \left(\det U_0'\right)^\nu\ \mathrm{e}^{\mu\operatorname{Re}\operatorname{Tr}U_0'}. \tag{7.9}$$

The choice $T^a = T^b \neq 1$, $\operatorname{Tr}T^a = 0$ corresponds to the flavour non-singlet contribution while $T^a = T^b = 1$ leads to the singlet contribution. After integration over the spacial components and for $y = 0$ one gets for the flavour non-singlet contribution

$$\int \mathrm{d}^3x \left\langle \mathcal{J}_0^a(x)\mathcal{P}^a(0)\right\rangle_\nu^\mu = \frac{\Sigma}{2\mu}|\nu|h_1'(\tau) = \frac{|\nu|}{2mV}\left(\tau - \frac{1}{2}\right), \tag{7.10}$$

where $\int \mathrm{d}^3x\, G(x) = Th_1(\tau)$ and h_1 defined in (E.4a). The relevant zero mode integral is reported in Eq. (E.7).

The flavour singlet contribution reads

$$\int \mathrm{d}^3x \left\langle \mathcal{J}_0^a(x)\mathcal{P}^a(0)\right\rangle_\nu^\mu = \Sigma\left\langle \operatorname{Re}\,\operatorname{Tr}(U_0')\right\rangle_\nu^\mu \partial_0^x \int \mathrm{d}^3x\left[G(x) - NE(x)\right]. \tag{7.11}$$

It vanishes in the unquenched theory since $E(x-y) = G(x-y)/N$ in this case. In quenched ChPT it is

$$E(x) = \frac{\alpha}{2N_\mathrm{c}}G(x) + \frac{m_0^2}{2N_\mathrm{c}}F(x), \tag{7.12}$$

with $F(x)$ defined in (E.3d). Here the integrated result reads

$$\int \mathrm{d}^3x \left\langle \mathcal{J}_0^a(x)\mathcal{P}^a(0)\right\rangle_\nu^\mu = N|\nu|\left[\left(1 - \frac{\alpha N}{2N_\mathrm{c}}\right)h_1'(\tau) + \frac{m_0^2 N}{24N_\mathrm{c}}h_2'(\tau)\right], \tag{7.13}$$

with h_2 defined in (E.4b).

7.3 Zero Mode Saturation of Three-Point Functions

The three-point function C_P corresponds to C_1 defined in the previous chapter except that the left-handed currents have been replaced by insertions of the pseudoscalar density,

$$C_P^{\pm}(x_0, y_0) \equiv \int \mathrm{d}^3x\, \mathrm{d}^3y \left\langle \left[P(x)\right]_{du} \left[\mathcal{Q}_1^{\pm}(0)\right] \left[P(y)\right]_{us} \right\rangle. \tag{7.14}$$

The four-fermion operator has been introduced in Eq. (6.8). Again one assumes four mass-degenerate flavours. This SU(4)-symmetric theory has been introduced in Section 6.3. The results for the correlator in leading-order ChPT and from lattice QCD are given in the following.

7.3.1 Leading Order ChPT results

The leading order ChPT behaviour of the correlator has been calculated by Hernández [115],

$$\mathcal{C}_P(x_0, y_0) = g_1^{\pm} \left(\nu^2 \mp |\nu|\right)\, h_1'\left(\frac{x_0}{T}\right) h_1'\left(\frac{y_0}{T}\right). \tag{7.15}$$

It is directly proportional to the low-energy constants $g_1^{\pm}$. The time dependence is given through the derivative of $h_1(\tau)$ defined in (E.4a). It is possible to extract the low-energy constants from different ratios. Sufficiently far away from the insertion points and for $|\nu| > 1$ one gets

$$\frac{\mathcal{C}_P^{-}(x_0, y_0)}{\mathcal{C}_P^{+}(x_0, y_0)} = \frac{|\nu| + 1}{|\nu| - 1} \cdot \frac{g_1^{-}}{g_1^{+}}. \tag{7.16}$$

The individual low-energy constants can be obtained from the ratios

$$R_P^{\pm} \equiv \frac{\mathcal{C}_P^{\pm}(x_0, y_0)}{\mathcal{C}_{JP}(x_0)\mathcal{C}_{JP}(y_0)} = 4\left(1 \mp \frac{1}{|\nu|}\right) \cdot g_1^{\pm}, \tag{7.17}$$

where $\mathcal{C}_{JP}$ was defined in the previous section. The LO result for $\mathcal{C}_{JP}$ is given in Eq. (7.10). At this order in ChPT the time dependence in the ratio (7.17) is cancelled exactly. As will be explained in more detail in the next subsection the correlation functions consist of a colour-connected and a colour-disconnected piece. One can also form a ratio of these terms to extract g_1^{-}/g_1^{+},

$$\frac{\mathcal{C}_P^{\mathrm{disc}}(x_0, y_0)}{\mathcal{C}_P^{\mathrm{conn}}(x_0, y_0)} = -\frac{\frac{|\nu|+1}{|\nu|-1} \cdot \frac{g_1^{-}}{g_1^{+}} + 1}{\frac{|\nu|+1}{|\nu|-1} \cdot \frac{g_1^{-}}{g_1^{+}} - 1}. \tag{7.18}$$

7.3.2 Lattice Observables

The lattice version of the three-point function reads

$$C_P^{\pm}(x_0 - z_0, y_0 - z_0) = \frac{1}{L^3} \sum_{\vec{x},\vec{y},\vec{z}} \left\langle P^a(x) \left[Q_1^{\pm}\right]_{rsuv}(z) P^p(y) \right\rangle, \tag{7.19}$$

where $P^a = \overline{\psi}\gamma_5 T^a \psi$. Now one can again multiply by $(mV)^2$ to remove the divergence and define

$$\lim_{m\to 0}(mV)^2 \mathcal{C}_P^{\pm}(x_0, y_0) \equiv A_\nu(x_0, y_0) \pm \tilde{A}_\nu(x_0, y_0). \tag{7.20}$$

The quantities A_ν and $\tilde{A}_\nu$ can be expressed through the fermionic zero modes in analogy to the procedure described in Section 7.1,

$$A_\nu(x_0 - z_0, y_0 - z_0) = \frac{1}{L^3}\sum_{i,j\in\mathcal{K}}\sum_{\vec{x},\vec{y},\vec{z}} \left\langle \left[v_i^\dagger(x) S(x,z)\gamma_\mu P_- v_i(z)\right]\left[v_j^\dagger(y) S(y,z)\gamma_\mu P_- v_j(z)\right]\right\rangle_\nu, \tag{7.21a}$$

$$\tilde{A}_\nu(x_0 - z_0, y_0 - z_0) = \frac{1}{L^3}\sum_{i,j\in\mathcal{K}}\sum_{\vec{x},\vec{y},\vec{z}} \left\langle \left[v_j^\dagger(x) S(x,z)\gamma_\mu P_- v_i(z)\right]\left[v_i^\dagger(y) S(y,z)\gamma_\mu P_- v_j(z)\right]\right\rangle_\nu, \tag{7.21b}$$

for negative chirality of the zero modes, and

$$A_\nu(x_0 - z_0, y_0 - z_0) = \frac{1}{L^3}\sum_{i,j\in\mathcal{K}}\sum_{\vec{x},\vec{y},\vec{z}} \left\langle \left[v_i^\dagger(x) \gamma_\mu P_- S(z,y) v_i(z)\right]\left[v_j^\dagger(y) \gamma_\mu P_- S(z,x) v_j(z)\right]\right\rangle_\nu, \tag{7.22a}$$

$$\tilde{A}_\nu(x_0 - z_0, y_0 - z_0) = \frac{1}{L^3}\sum_{i,j\in\mathcal{K}}\sum_{\vec{x},\vec{y},\vec{z}} \left\langle \left[v_j^\dagger(x) \gamma_\mu P_- S(z,y) v_i(z)\right]\left[v_i^\dagger(y) \gamma_\mu P_- S(z,x) v_j(z)\right]\right\rangle_\nu, \tag{7.22b}$$

for positive chirality. There is a remaining propagator, which has to be computed for each zero mode and chirality. This has to be done at non-vanishing quark mass, of course. But the extrapolation to $m = 0$ turns out to be not problematic.

The second observable is the two-point function C_{JP}. Its divergence is linear in m. One can relate it to the zero modes in a similar way as the three-point function,

$$\lim_{m\to 0}(mV) C_{JP}(x_0 - z_0) = \frac{1}{L^3}\sum_{i\in\mathcal{K}}\sum_{\vec{x},\vec{z}} \begin{cases} \left\langle \left[v_i^\dagger(x) S(x,z)\gamma_\mu P_- v_i(z)\right]\right\rangle_\nu & \text{for } P_- v_i = v_i, \\ \left\langle \left[v_i^\dagger(x) \gamma_\mu P_- S(x,z) v_i(z)\right]\right\rangle_\nu & \text{for } P_+ v_i = v_i. \end{cases} \tag{7.23}$$

As input for this observable one can use the same propagators that are used for the computation of A_ν and $\tilde{A}_\nu$. The summation over $\vec{z}$ is performed implicitly by inverting the Dirac operator with each of the zero modes restricted to a single timeslice as a source.

7.3.3 Numerical Results

The first numerical experience has been gained on a subset of the configurations from lattice B generated for the calculation in the ϵ-regime described in the previous chapter. Since the index of the configuration has already been known and 20 low modes have been stored the

additional computational effort to compute the zero modes and the additional propagators is comparatively small.

The ratio (7.16) is undefined for $\nu = 0$ and infinite for $|\nu| = 1$. The finite volume corrections to the correlators are of next-to-leading order and have not been computed so far. They are expected to be moderate for $|\nu| \ll \sqrt{\langle \nu^2 \rangle}$. One can estimate $\langle \nu^2 \rangle$ from the topological susceptibility which was computed in [109], see Section 6.5.3. Since $\sqrt{\langle \nu^2 \rangle} = 5.89$ at the given bare coupling and lattice volume, only the interval $|\nu| \in [2, 5]$ has been considered.

Leading order ChPT predicts the ratios to be constant far enough from the insertion points x_0 and y_0. Therefore it is sufficient to fit them to a constant over an interval in the middle of the time direction. The results from these fits, which all show a correlated χ^2 smaller than 1, are summarised in Table 7.1. The plots in Figure 7.1 give an impression on the quality of the plateaux for the smallest quark mass. The considered bare masses are $am = 0.003, 0.005, 0.010$. This corresponds to $5 - 16\,\mathrm{MeV}$.

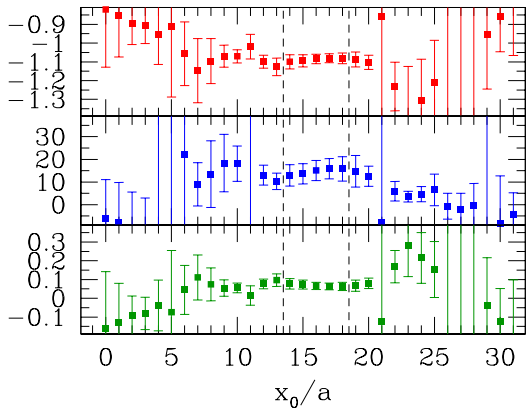

(a) From top to bottom: R_{dc} (7.18), R^-/R^+ (7.16) and its inverse R^+/R^- as a function of time.

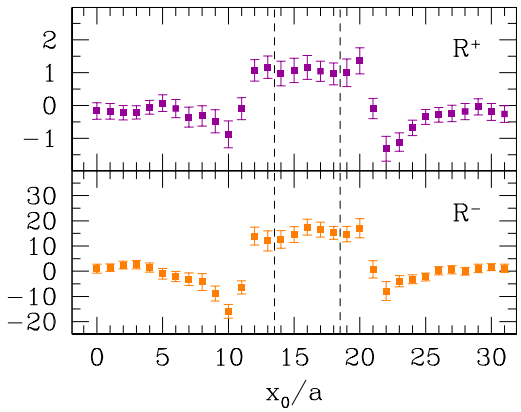

(b) Ratios defined in Eq. (7.17) as a function of time

Figure 7.1: Bare results for the ratios of correlation function for the lowest mass ($am = 0.003$) and $|\nu| = 3$. The chosen interval for the constant fit is indicated by the vertical dashed lines. The insertions of the currents sit at $x_0/a = 11$ and 21.

Three masses turn out to be sufficient for the chiral extrapolation. The full results are listed in Table 7.1. The plots in Fig. 7.2 (a) and (c) show that the remaining mass dependence is rather mild.

The bare ratios are then multiplied with the renormalisation factors and Wilson coefficients introduced in Section 6.6. One can use the same Z-factors (Table 6.5) since the contribution from the insertions of the pseudoscalar density cancels in the ratios.

In the next step the matching to ChPT at leading order is performed . The relevant formulae can be found in Subsection 7.3.1. The resulting low-energy constants are summarised in Table 7.2. The numerical results for the LECs are very well compatible with a constant in $|\nu|$,

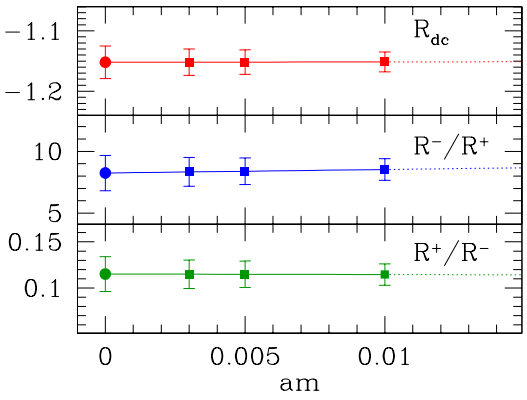

(a) Results at $|\nu| = 5$ for the different ratios of three-point functions with a linear chiral extrapolation.

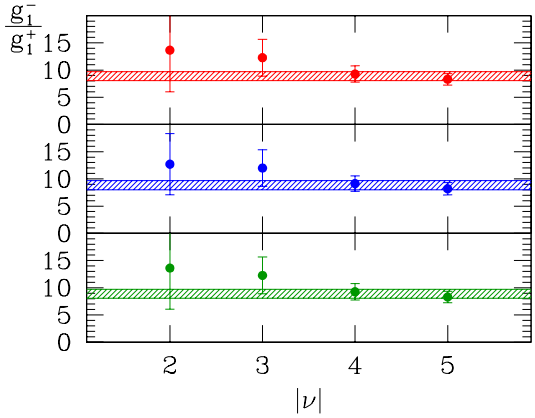

(b) Weighted average of the ratio of LECs over the interval $|\nu| = 2, 5$ from the corresponding ratios shown on the l.h.s.

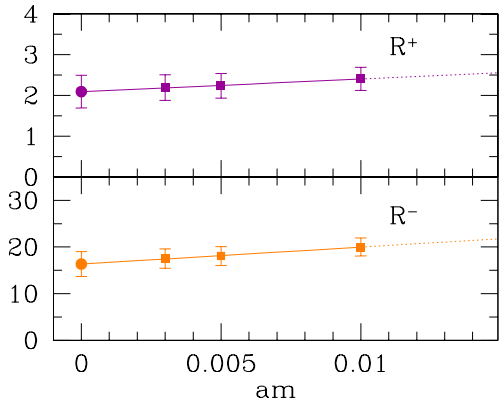

(c) Results at $|\nu| = 5$ with a linear chiral extrapolation for the ratios defined in (7.17).

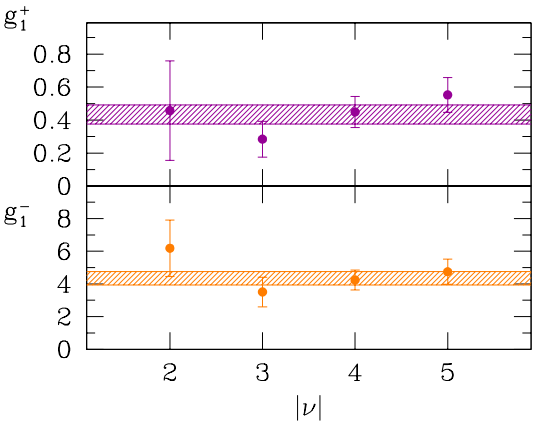

(d) Weighted average of the individual LECs $g_1^{\pm}$ over the interval $|\nu| = 2, 5$ from the corresponding ratios shown on the l.h.s.

Figure 7.2: Illustration of the results of the Tables 7.1 — only for $|\nu| = 5$ — and 7.2.

$\lvert\nu\rvert$	cfgs	am	$C_P^{\text{disc}}/C_P^{\text{conn}}$	C_P^-/C_P^+	C_P^+/C_P^-	R_P^-	R_P^+
2	129	0.010	−1.062(17)	19.7(5.0)	0.049(13)	30.7(4.9)	1.47(45)
		0.005	−1.058(22)	21.3(7.3)	0.045(17)	21.3(7.3)	1.27(53)
		0.003	−1.053(23)	22.6(9.2)	0.042(18)	28.1(6.1)	1.20(58)
		0.000	*−1.050(29)*	*23(10)*	*0.040(22)*	*26.6(7.4)*	*1.08(71)*
3	103	0.010	−1.085(13)	15.0(2.2)	0.0663(95)	20.2(2.7)	1.35(25)
		0.005	−1.084(18)	15.1(3.1)	0.065(13)	16.9(2.6)	1.11(26)
		0.003	−1.086(21)	14.6(3.5)	0.067(16)	15.4(2.6)	1.04(27)
		0.000	*−1.085(24)*	*14.8(4.1)*	*0.066(18)*	*13.4(3.5)*	*0.90(34)*
4	100	0.010	−1.145(14)	9.03(82)	0.110(10)	19.4(1.8)	2.13(26)
		0.005	−1.142(18)	9.2(1.1)	0.108(13)	17.2(1.6)	1.85(25)
		0.003	−1.140(20)	9.3(1.2)	0.107(14)	16.5(1.6)	1.76(26)
		0.000	*−1.138(24)*	*9.4(1.5)*	*0.105(17)*	*15.2(2.2)*	*1.59(34)*
5	73	0.010	−1.162(15)	8.13(69)	0.122(10)	20.0(1.9)	2.40(28)
		0.005	−1.168(18)	7.83(79)	0.126(13)	18.1(2.0)	2.23(30)
		0.003	−1.171(19)	7.74(82)	0.128(13)	17.5(2.1)	2.19(31)
		0.000	*−1.175(24)*	*7.6(1.1)*	*0.131(17)*	*16.3(2.7)*	*2.09(40)*

Table 7.1: Results for the different ratios from a fit to a constant for $x_0/a \in [14, 18]$. For each index ν the results are extrapolated to $am = 0$ with a linear fit.

Figure 7.2 (b) and (d). The statistical fluctuations are much larger for $|\nu| = 2$ which is consistent with the findings on ϵ-regime correlation functions in Chapter 6. Again we obtain the final result with a weighted average over the considered topological sectors.

Although the estimates are preliminary, the values for the low-energy constants,

$$g_1^- = 4.34(41), \qquad g_1^+ = 0.434(58), \tag{7.24}$$

again suggest a large enhancement in the SU(4)-symmetric case. They roughly agree with the values from the direct ϵ-regime computation (Chapter 6). But one has to keep in mind, that finite volume corrections are not taken into account. Still the outcome of this first simulation is very encouraging and it should be possible to implement the same strategy for the SU(3)-symmetric case where the direct computation is even more difficult.

	g_1^-/g_1^+			g_1^-	g_1^+
$\lvert\nu\rvert$	from $C^{\text{disc}}/C^{\text{conn}}$	from C^-/C^+	from C^+/C^-	from R^-	from R^+
2	13.6(7.6)	12.7(5.6)	13.6(7.6)	6.2(1.7)	0.46(30)
3	12.3(3.4)	12.0(3.4)	12.3(3.4)	3.51(90)	0.28(11)
4	9.3(1.5)	9.1(1.4)	9.3(1.5)	4.24(61)	0.449(95)
5	8.3(1.0)	8.2(1.1)	8.3(1.0)	4.75(77)	0.55(11)
w.a.	8.89(83)	8.86(84)	8.89(83)	4.34(41)	0.434(58)
χ^2	0.59	0.58	0.59	0.76	1.1

Table 7.2: Ratio of LECs g_1^-/g_1^+ resulting from the chiral extrapolation of the different combination of three-point functions with MFI perturbative renormalisation. The separate estimate of the g_1^+ and g_1^- stems from a matching of the result on R_P^+ and R_P^- (Table 7.1) with the LO formula (7.17).

8 Conclusion and Outlook

In this thesis we have performed numerical investigations of lattice QCD with exact chiral symmetry. One large part of this work has been the development of new methods to deal with simulation at very small quark masses. The other main ingredient has been the interplay of lattice QCD and Chiral Perturbation Theory (ChPT). The free parameters of ChPT, called low-energy constants, can be fixed by matching lattice results to ChPT formulae.

Simulating QCD, or in this case the quenched approximation of QCD, at very small quark masses requires sophisticated numerical techniques. In Chapter 4 of this thesis we have tested a new algorithm for the inversion of the Neuberger Dirac operator, namely the generalised minimal residual (GMRES) algorithm with low-mode preconditioning (LMP). LMP is a method to reduce the slowing down of the inversion with decreasing quark mass by projecting out the eigenmodes corresponding to the lowest eigenvalues of the operator. The outcome of a numerical comparison with the conjugate gradient (CG) algorithm is, that both algorithm are suitable for very small quark masses if LMP is employed.

A practical application of the mentioned algorithm is the computation of the multiplicative renormalisation constant of the scalar density Z_{S} for Ginsparg-Wilson fermions at several lattice spacings. Here we follow an indirect route via intermediate results from O(a)-improved Wilson fermions. The continuum limit of the quark mass at a reference scale from these results is matched to the same observable in our simulation to compute Z_{S}. In Chapter 5 we report on this work which allows to extrapolate the low-energy constant Σ, which is equal to the chiral condensate in full QCD, to the continuum limit. For the condensate we obtain $\Sigma_{\overline{\mathrm{MS}}}(2\,\mathrm{GeV}) = (285 \pm 9\,\mathrm{MeV})^3$, if the scale is set by the kaon decay constant F_K. The study also includes the first scaling tests with Ginsparg-Wilson fermion for F_K and the vector meson mass, which show, that lattice artefacts are very small for this discretisation provided the renormalisation procedure is non-perturbative.

An important conceptual advantage of Ginsparg-Wilson fermions is the possibility to compare directly with continuum Chiral Perturbation Theory. The ϵ-regime of QCD is a peculiar finite volume regime where the quark mass m is so small that $\mu = m\Sigma V \ll 1$. Matching QCD and ChPT in this regime allows to extract the occurring low-energy constants directly in the chiral limit. In lattice QCD in the ϵ-regime one has to face large fluctuation and numerical instabilities which cannot be tamed by standard methods. A procedure called low-mode averaging (LMA) allows to separate the most fluctuating parts of the different observables since only a few low-lying eigenvalues are responsible for the problems. It is shown, that LMA is essential for obtaining reliable results in the ϵ-regime.

In Chapter 6 this concept has been applied to matrix elements of hadronic kaon decays. The

matching is performed between three-point correlation functions of an effective four-fermion operator. Since it is not possible to access two-body final states in lattice QCD directly, we compute matrix elements of unphysical $K \to \pi$ transitions. In ChPT the low-energy constants are the same as in the physical $K \to \pi\pi$ decays. The aim of the project is to disentangle different contributions to the $\Delta I = 1/2$ rule which states that decays into the isospin zero state of the two pions are preferred. In a first step the contributing correlation functions have been evaluated in the limit of four mass-degenerate flavours. In this SU(4)-symmetric case the effect of the charm quark mass is cancelled and therefore only QCD effects at a typical scale around 250 MeV are responsible for the observed enhancement. The correlation functions in QCD are renormalised non-perturbatively with a procedure very similar to the case of the scalar density. Finally the low-energy constant are related to the decay amplitudes via a leading-order ChPT formula. Our value for the enhancement in the SU(4)-symmetric limit is $A_0/A_2 = 6.7(1.2)$. This has to be compared with the experimental value of $A_0/A_2 = 22.1$. Keeping in mind that the study is quenched and on one rather coarse lattice, we still conclude that a substantial fraction of the enhancement is due to genuine QCD effects. The next step will be to investigate the same setting with a heavy charm quark.

The same decay amplitudes can also be addressed in a different framework, where correlators are calculated which diverge in the chiral limit. For $m \to 0$ these correlators are completely dominated by the zero modes of the massless Dirac operator. We have computed these zero modes on the lattice, which is only possible for a fermion discretisation which preserves chiral symmetry. Again the matching of the correlation functions is performed in the ϵ-regime, where we have calculated the leading order ChPT result for the two-point function C_{JP} which is also needed to extract the individual low-energy constants for the decay channels. The obtained values for the low-energy constants are consistent with the estimates form the previous project, which further corroborates our findings. It is important that we have obtained a similar same answer from a procedure with very different systematic uncertainties.

All our results on the kaon decay amplitudes are valid in the limit where the charm quark mass is as small as the other quark masses. It will be important to leave this limit and consider the case where $m_u = m_d = m_s \ll m_c$. The physical charm quark mass is clearly to heavy for our simulation since the lattice cut-off is too low. But the low-energy constants as a function of m_c below the physical charm scale are accessible. A further complication is a new diagram which appears in this case and contains a propagator going back to itself. A possibility would be to use volume source techniques for this problem. It will also be interesting to apply the method of zero-mode saturation to the SU(3) case. From the experience with other observables it is not expected that going to smaller lattice spacing will change the picture qualitatively.

The other main source of systematic uncertainty is of course the quenched approximation. Direct simulations of dynamical Ginsparg-Wilson fermions are possible, but they are extremely demanding. Also the tunnelling between topological sectors cannot be reproduced very well, so far. Still these simulations will be done within the next ten years. A faster way could be to use mixed actions. In this approach the dynamical configurations are generated with other lattice fermions, for instance Wilson fermions. Then the observables constructed from valence Ginsparg-Wilson quarks exhibit most of the positive features of this discretisation.

A Lattice Procedures

A.1 Monte Carlo Algorithms

A.1.1 The Basic Concept

In order to compute expectation values of observables on the lattice it is necessary to generate a set of gauge configurations U according to the probability distribution,

$$\rho([U]) = \frac{1}{Z} \cdot \mathrm{e}^{-S([U])}, \tag{A.1}$$

where Z is chosen such that $\sum_U \rho([U]) = 1$. The transition probability P to go from one configuration to the next one must fulfil the *strong ergodicity condition*,

$$P\left([U] \to [U']\right) > 0, \quad \text{for all} \quad U, U'. \tag{A.2}$$

An algorithm satisfying (A.2) is called ergodic because the whole space of configurations is sampled since every representative can be reached from every starting point with finite probability.

An updating (or Markov) process which fulfils the condition of *detailed balance*,

$$P\left([U] \to [U']\right) \rho\left([U]\right) = P\left([U'] \to [U]\right) \rho\left([U']\right), \tag{A.3}$$

automatically produces configurations with the distribution (A.1).

The update in our programs are done with the algorithm described in the next subsection.

A.1.2 Heatbath and Overrelaxation

The idea of the heatbath algorithm [3] is to change one link only and then loop over all links,

$$P\left([U] \to [U']\right) = \prod_l P\left([U_l] \to [U'_l]\right). \tag{A.4}$$

The link variable is brought into contact with an "infinite heatbath". That means it is updated with the equilibrium distribution $1/Z \exp(S[U'])$ irrespective of the initial distribution. The *sweep* over all links ensures the ergodicity, if the local update satisfies a local version of the ergodicity condition (A.2). In practice the update is done for three SU(2) subgroups of SU(3) as introduced by Cabibbo and Marinari [116].

The second ingredient is called *overrelaxation* [117–119]. The link variable for the next update step should be chosen" as far as possible" [120] from the original one. The Wilson gauge action, for example, can be decomposed in

$$S[U] = -\frac{\beta}{N} \text{ Re Tr}(U_l S_l) + \hat{S}(\hat{U}_l), \tag{A.5}$$

where $\hat{U}_l$ means the set of all link variable except U_l. The factor S_l denotes the sum over the *staples* around U_l. A staple is a product of link variables such that

$$S_l = \sum_{\substack{\pm\nu \\ \nu\neq\mu}} U_\nu(x+\hat{\mu})U_\mu^\dagger(x+\hat{\mu}+\hat{\nu})U_\nu^\dagger(x+\hat{\nu}), \quad \text{for} \quad U_l = U_\mu(x). \tag{A.6}$$

Each staple forms a plaquette together with the link U_l. A candidate for an overrelaxed link is now

$$U' = U_0 U^{-1} U_0, \quad \text{where} \quad U_0 = [P_{\text{SU(2)}}(S_l)]^{-1}. \tag{A.7}$$

The given choice for U_0 with the projector on the group can only be made for SU(2). For SU(3) it is not possible to use a simple projector.

In our programs we use six overrelaxation steps for each heatbath step. Since the generation of configurations is a rather small part of the whole simulation in our quenched studies, we choose the distance between configurations written to disk to be fairly large. We use every 500th configuration for the analysis.

A.2 Error Procedures

The estimate of the statistical uncertainty of a Monte Carlo simulation can be done in different ways. Here we summarise the two procedures we used, namely *jackknife* errors and *bootstrap distributions*.

The jackknife error usually gives a more reliable estimate of the error than the plain standard deviation. Considering a primary observable A and its values A_i on N configurations, the *jackknife samples* A'_i are constructed as the average of all but one of the A_i,

$$A'_i \equiv \frac{1}{N-1} \sum_{\substack{j=1 \\ j\neq i}}^{N} A_i. \tag{A.8}$$

The jackknife error is then obtained from the average of the jackknife samples,

$$\Delta A \equiv \frac{N-1}{N} \sum_{i=1}^{N} A'_i \tag{A.9}$$

The main advantage of the procedure is the ability to estimate the errors for arbitrary functions of the primary quantities. The jackknife error for such a function f is given as,

$$\Delta f(A) = \frac{N-1}{N} \sum_{i=1}^{N} f(A'_i). \tag{A.10}$$

The second method we widely used is the *bootstrap error*. It is applicable to skewed distribution because it allows for asymmetric errors. The idea is to estimate the probability distribution of the observable from a limited set of data and use the (bootstrap) distribution for the error analysis. The error can then simply be read off from the central 68% interval of the distribution.

A.3 Fitting Two-Point Correlation Functions

The simplest fermionic observables are two-point functions of quark bilinears. We consider the left-handed current J_μ and the pseudoscalar density P as well as the vector current V_μ,

$$J_\mu(x) = (\overline{\psi}_r \gamma_\mu P_- \psi_s)(x), \qquad P(x) = (\overline{\psi}_r \gamma_5 \psi_s)(x), \tag{A.11}$$

$$C_{\mathrm{QR}}(x_0) = a^3 \sum_{\vec{x}} \Big\langle Q(x) R(0) \Big\rangle, \qquad Q,\, R = J_0,\, P. \tag{A.12}$$

$$C_{\mathrm{VV}}(x_0) = a^3 \sum_{\vec{x}} \sum_{k=1}^{3} \Big\langle V_k(x) V_k(0) \Big\rangle, \qquad V_k(x) = (\overline{\psi}_r \gamma_k \psi_s)(x). \tag{A.13}$$

The flavour indices are chosen such that one obtains the flavour non-singlet contribution, $r \neq s$. The sum over the spatial coordinates projects onto the state with spatial momentum zero.

The time dependence of a generic two-point function C_2 can be written as a sum over exponentials with exponents m_i and periodic boundary conditions require a symmetric time dependence,

$$C_2(x_0) = \sum_i c_i \left[\mathrm{e}^{-m_i(x_0 - \frac{T}{2})} + \mathrm{e}^{-m_i(-x_0 + \frac{T}{2})} \right] = 2 \sum_i c_i \cosh\left[m_i (x_0 - \tfrac{T}{2}) \right]. \tag{A.14}$$

For large separations from the boundary the contribution with the smallest mass dominates, because it decays less rapidly than the heavier ones,

$$C_2(x_0) \to 2 c_0 \cosh\left[m_0 (x_0 - \tfrac{T}{2}) \right], \quad \text{for} \quad 0 \ll x_0 \ll T. \tag{A.15}$$

The ground state energy — or mass — can be obtained by fitting the correlation function to the ansatz (A.15). Of course, one has to restrict the fitting interval to timeslices "in the middle" of the lattice. The optimal fit-range for the ground state can be estimated by including a second mass in the fit,

$$2 c_0 \cosh\left[m_0 (x_0 - \tfrac{T}{2}) \right] + 2 c_1 \cosh\left[m_1 (x_0 - \tfrac{T}{2}) \right]. \tag{A.16}$$

A convenient way to check for exited states in the spectrum is to estimate the lowest mass from a *single cosh* fit (A.15) and to use the resulting m_0 to constrain the ansatz (A.16) to a three parameter fit. A criterion for choosing the time interval for the ground state is the smallest value for x_0 at which the coefficient c_1 is still consistent with zero, assuming a reasonable χ^2 per degree of freedom.

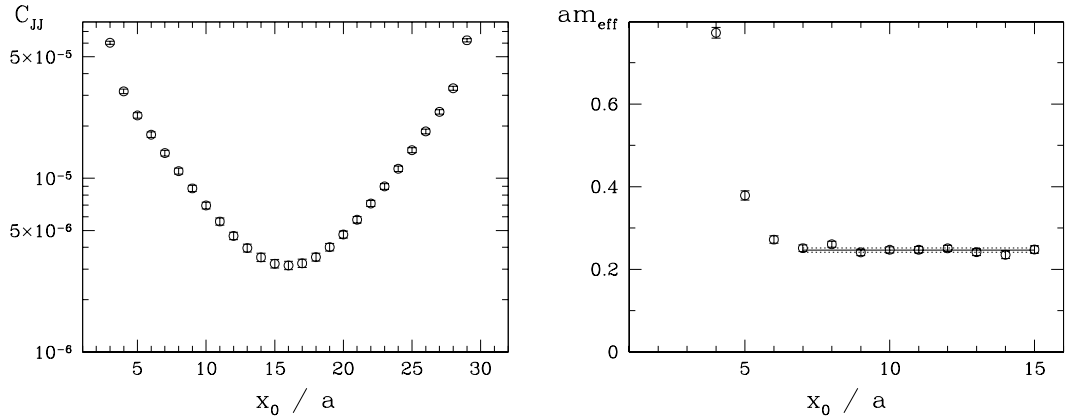

(a) Correlation function C_{JJ} (A.12) on a logarithmic scale.

(b) Effective mass plot of C_{JJ}. The line denotes the fit according to ansatz (A.15), and the fit-range in x_0

Figure A.1: Example for a two-point function on a $16^3 \times 32$ lattice. The resulting pseudoscalar mass is of the order of the kaon mass.

It is also possible to define an *effective mass* of the ground state as

$$am_{\text{eff}} \equiv -\frac{\mathrm{d}}{\mathrm{d}x_0} \log C_2. \tag{A.17}$$

After averaging over the forward and backward half of the lattice m_{eff} gives an useful estimate of the ground state mass without any fit procedure. The method can serve as a consistency check for the more accurate fit, see Figure A.1b.

A.4 Jacobi Smearing

Smearing in the context of a lattice simulation usually refers to a procedure in which a point-like object is replaced by a spatially extended one. In this case the source (or sink) of the numerical inversion is smeared.

Computing propagators from extended sources can reduce fluctuations for certain correlators. In [121] *Jacobi smearing* is advertised as an efficient iterative procedure to construct the smeared field. The *smearing kernel* K is defined as [122]

$$\sum_{\vec{y}} K(x,y)\eta_{\text{s}}(y) = \eta(x). \tag{A.18}$$

Using the ansatz $K = 1 - \kappa\Delta$, its inverse is approximated by applying Δ iteratively to the point source. Δ is a covariant lattice Laplacian,

$$\Delta = \sum_{k=1}^{3} \left[U_k(x)\delta(x_k - a, y_k) - U_k^{\dagger}(x - \hat{k})\delta(x_k - a, y_k) \right]. \tag{A.19}$$

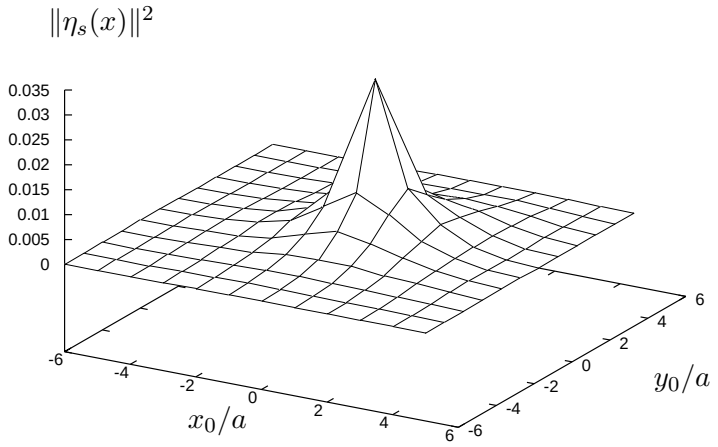

Figure A.2: Illustration of Jacobi smearing. The local norm $\|\psi\|^2 \equiv (\psi(x), \psi(x))$ of the source field is plotted as a function of two spatial directions. The smearing parameter are $\kappa = 0.194$ and 90 iterations.

The smeared source is then given recursively by

$$\eta_s^n = \eta + \kappa \Delta \eta_s^{n-1}. \tag{A.20}$$

There are two free parameters, the dampening factor κ and the number of iterations n. Tuning both simultaneously allows it to generate a source with a given average radius. The smearing is manifestly gauge invariant and extends only in the three spatial directions. For the correlator of the vector current it was essential to use smearing while the results for the pseudoscalar mesons did not improve.

B Renormalisation Group Equations

The renormalised parameters of QCD, namely the coupling $\bar{g}$ and the quark masses $\overline{m}_f$, where $f = u, d, c, s, t, b$, obey the renormalisation group equations (RGEs)

$$\mu \frac{\partial \bar{g}}{\mu} = \beta(\bar{g}), \tag{B.1a}$$

$$\mu \frac{\partial \overline{m}_f}{\mu} = \tau(\bar{g}) \overline{m}_f. \tag{B.1b}$$

The perturbative expansion of the RG functions β and τ reads

$$\beta g = -g^3 \sum_{k=0}^{\infty} b_k g^{2k}, \tag{B.2a}$$

$$\tau g = -g^2 \sum_{k=0}^{\infty} d_k g^{2k}, \tag{B.2b}$$

with the universal coefficients

$$b_0 = \frac{1}{(4\pi)^2} \left(\frac{11}{3} N_\mathrm{c} - \frac{2}{3} N_\mathrm{f} \right), \tag{B.3a}$$

$$b_1 = \frac{1}{(4\pi)^4} \left(\frac{34}{3} N_\mathrm{c}^2 - N_\mathrm{f} \left[\frac{13}{3} N_\mathrm{c} - \frac{1}{N_\mathrm{c}} \right] \right), \tag{B.3b}$$

$$d_0 = \frac{8}{(4\pi)^2}. \tag{B.3c}$$

The higher coefficients depend on the renormalisation scheme.

Solving the RGEs (B.1), one can calculate the *renormalisation group invariant* (RGI) quark mass M_f,

$$M_f = \overline{m}_f \cdot \left[2 b_0 \bar{g}^2 \right]^{d_0 / 2 b_0} \exp \left\{ - \int_0^{\bar{g}} \mathrm{d}g \left[\frac{\tau(g)}{\beta g} - \frac{d_0}{b_0 g} \right] \right\}, \tag{B.4}$$

which is used to determine the renormalisation constant $\widehat{Z}_\mathrm{S}$ in Chapter 5.

In Chapter 6 four-fermion operators appear, which have to be renormalised. One defines the anomalous dimension for the four-fermion operator Q_1^τ as

$$\gamma^\tau(g) = g^2 \sum_{k=0}^{\infty} \gamma_k^\tau g^{2k}, \quad \tau = \pm 1. \tag{B.5}$$

The one-loop coefficient is again universal:

$$\gamma_0^\tau = -\frac{1}{(4\pi)^2}\frac{6\tau(N_\mathrm{c}-\tau)}{N_\mathrm{c}}. \tag{B.6}$$

The two-loop anomalous dimension is scheme dependent and in the 't Hooft-Veltman (HV(MS)) scheme it reads [123]

$$\gamma_1^\tau = \frac{1}{(4\pi)^4}\frac{N_\mathrm{c}-\tau}{2N_\mathrm{c}}\left(-\frac{88}{3}N_\mathrm{c}^2+21+\frac{16}{3}N_\mathrm{c}N_\mathrm{f}-\tau\left\{\frac{157}{3}N_\mathrm{c}+\frac{57}{N_\mathrm{c}}-\frac{28}{3}N_\mathrm{f}\right\}\right). \tag{B.7}$$

This expression can be related to different schemes by

$$\gamma_S^\tau(g) = \gamma^\tau(g) + \beta(g)\frac{\partial}{\partial g}\ln\mathcal{X}_S^\tau(g), \tag{B.8a}$$

$$\mathcal{X}_S^\tau(g) = 1+\sum_{k=1}^{\infty}(x_k^\tau)_S\, g^{2k}. \tag{B.8b}$$

For the two-loop term this means $(\gamma_1^\tau)_S = \gamma_1\tau - 2b_0(x_1^\tau)_S$. For the RI/MOM scheme the factor x_1 reads [110]

$$(x_1^\tau)_\mathrm{RI} = -\frac{1}{(4\pi)^2}\frac{(N_\mathrm{c}-\tau)}{2N_\mathrm{c}}\left(4N_\mathrm{c}-6\tau[1-4\ln(2)]\right). \tag{B.9}$$

The perturbative expansion of the Wilson coefficient k_1^τ contains the coefficients h_1^τ which are in the HV(MS) scheme given by

$$h_1^\tau = \frac{1}{(4\pi)^2}\frac{N_\mathrm{c}-\tau}{2N_\mathrm{c}}(3\tau-4N_\mathrm{c}). \tag{B.10}$$

The conversion to other schemes is then simply given by $(h_1^\tau)_S = h_1^\tau - (x_1^\tau)_S$.

C Chiral Condensate, Numerical Details

C.1 Two-Point Function Fits

The two-point correlation functions of the left-handed and vector current and of the pseudoscalar density are fitted with a correlated least-square method to the ansatz

$$C_{\mathrm{X}} = 2A_{\mathrm{X}} \cosh\left(B_X x_0 - \frac{T}{2}\right), \quad \mathrm{X} = JJ, PP, VV. \tag{C.1}$$

		C_{JJ}			C_{PP}		
L/a	am	t_{min}	$A \cdot 10^{-4}$	B	t_{min}	$A \cdot 10^{-2}$	B
12	0.040	7	1.14(6)	0.262(9)	7	1.57(11)	0.267(6)
	0.053		1.33(7)	0.294(8)		1.33(8)	0.300(5)
	0.067		1.54(7)	0.327(8)		1.19(6)	0.332(5)
	0.113		2.32(9)	0.421(6)		1.03(4)	0.426(3)
14	0.034	10	0.88(6)	0.235(7)	8	1.02(6)	0.235(4)
	0.046		1.03(6)	0.266(6)		0.88(4)	0.269(4)
	0.057		1.18(6)	0.292(6)		0.81(3)	0.297(3)
	0.097		1.75(7)	0.377(4)		0.73(2)	0.385(2)
16	0.030	9	0.65(4)	0.217(6)	9	0.90(6)	0.221(4)
	0.040		0.78(4)	0.247(5)		0.76(4)	0.248(3)
	0.050		0.92(4)	0.273(5)		0.68(3)	0.273(3)
	0.085		1.43(4)	0.352(3)		0.60(2)	0.351(2)
20	0.024	10	0.37(2)	0.168(5)	9	0.40(2)	0.177(3)
	0.032		0.44(2)	0.195(4)		0.37(2)	0.203(2)
	0.040		0.52(2)	0.218(4)		0.35(1)	0.226(2)

Table C.1: Summary of the single cosh fits to the different two-point functions.

The PCAC mass is related to the renormalisation factor of the axial current through

$$Z_A = \lim_{m \to 0} \frac{m}{m_{\mathrm{PCAC}}}. \tag{C.2}$$

		local			smeared		
L/a	am	$t_{\min}$	$A \cdot 10^{-4}$	B	$t_{\min}$	$A \cdot 10^{-2}$	B
12	0.040	7	1.14(6)	0.262(9)	7	1.57(11)	0.267(6)
	0.053		1.33(7)	0.294(8)		1.33(8)	0.300(5)
	0.067		1.54(7)	0.327(8)		1.19(6)	0.332(5)
	0.113		2.32(9)	0.421(6)		1.03(4)	0.426(3)
14	0.034	10	0.88(6)	0.235(7)	8	1.02(6)	0.235(4)
	0.046		1.03(6)	0.266(6)		0.88(4)	0.269(4)
	0.057		1.18(6)	0.292(6)		0.81(3)	0.297(3)
	0.097		1.75(7)	0.377(4)		0.73(2)	0.385(2)
16	0.030	9	0.65(4)	0.217(6)	9	0.90(6)	0.221(4)
	0.040		0.78(4)	0.247(5)		0.76(4)	0.248(3)
	0.050		0.92(4)	0.273(5)		0.68(3)	0.273(3)
	0.085		1.43(4)	0.352(3)		0.60(2)	0.351(2)
20	0.024	10	0.37(2)	0.168(5)	9	0.40(2)	0.177(3)
	0.032		0.44(2)	0.195(4)		0.37(2)	0.203(2)
	0.040		0.52(2)	0.218(4)		0.35(1)	0.226(2)

Table C.2: Summary of the single cosh fits to the correlation function C_{VV} with local and smeared source.

For the extrapolation the simplest possible ansatz,

$$Z_A = A + B \cdot m, \tag{C.3}$$

is used because the mass dependence of the ratio is extremely weak.

β	A	B
5.8458	1.7104(49)	−0.363(30)
5.9256	1.6118(31)	−0.324(23)
6.0000	1.5533(17)	−0.315(13)
6.1366	1.4778(16)	−0.223(27)

Table C.3: Fit parameters for the chiral extrapolation of m/m_{PCAC}.

C.2 Chiral Condensate

C.2.1 Σ from Random Matrix Theory at $\beta = 5.9256$

The numerical results from the matching of the lowest eigenvalues λ_k of the Dirac operator according to Eq. (3.29) are given in Table C.4. The RMT values for the eigenvalues are denoted by $\langle\zeta\rangle$ and can be obtained from [77, 124, 125].

	$\nu = 0$			$\nu = 1$		
k	$\langle\zeta_k\rangle$	$\langle\lambda_k\rangle$	$r_0^3\Sigma$	$\langle\zeta_k\rangle$	$\langle\lambda_k\rangle$	$r_0^3\Sigma$
1	1.772	0.0199(8)	0.240(10)	3.108	0.0332(8)	0.252(6)
2	4.791	0.0516(12)	0.255(6)	6.264	0.0684(11)	0.247(4)
3	7.902	0.0862(14)	0.247(4)	9.412	0.1037(13)	0.245(3)
4	11.030	0.1207(16)	0.246(3)	12.556	0.1379(13)	0.246(3)

	$\nu = 2$		
k	$\langle\zeta_k\rangle$	$\langle\lambda_k\rangle$	$r_0^3\Sigma$
1	4.344	0.0464(10)	0.253(5)
2	7.641	0.0833(13)	0.248(4)
3	10.846	0.1194(14)	0.245(3)
4	14.012	0.1503(13)	0.252(2)

Table C.4: Results for the bare condensate from RMT at $\beta = 5.9256$.

C.2.2 Continuum Extrapolation

The extrapolation to the continuum limit (CL) for all twelve estimates for Σ is tabulated below. The results are all consistent within errors and the slope is always compatible with zero.

ν	k	$\beta = 5.8458$	$\beta = 5.9256$	$\beta = 6.0000$	$\beta = 6.1366$	CL	slope
0	1	0.283(15)	0.285(20)	0.284(18)	0.282(18)	*0.281(26)*	0.01(57)
0	2	0.281(14)	0.298(18)	0.280(15)	0.299(15)	*0.301(23)*	−0.32(52)
0	3	0.283(14)	0.293(17)	0.275(14)	0.285(13)	*0.281(21)*	0.04(48)
0	4	0.281(14)	0.292(17)	0.269(13)	0.286(13)	*0.279(20)*	0.02(48)
1	1	0.285(15)	0.299(18)	0.277(15)	0.308(15)	*0.307(23)*	−0.38(52)
1	2	0.281(14)	0.293(17)	0.275(14)	0.294(13)	*0.293(21)*	−0.20(48)
1	3	0.280(14)	0.291(17)	0.273(13)	0.289(13)	*0.287(20)*	−0.12(47)
1	4	0.284(14)	0.292(16)	0.275(13)	0.290(13)	*0.286(20)*	−0.05(48)
2	1	0.292(15)	0.300(18)	0.283(15)	0.293(15)	*0.288(23)*	0.06(52)
2	2	0.287(14)	0.294(17)	0.271(14)	0.286(13)	*0.277(21)*	0.14(48)
2	3	0.285(14)	0.291(17)	0.271(13)	0.291(13)	*0.284(21)*	−0.01(48)
2	4	0.289(14)	0.299(17)	0.276(13)	0.293(13)	*0.286(20)*	0.03(48)

Table C.5: Renormalised scalar condensate (${r_0}^3\ \Sigma$). *CL* denotes the extrapolated result in the continuum limit. Our final result is the one for $\nu = 1$, $k = 2$. The slope is the coefficient of the $O(a^2)$ term and it is well compatible with zero for all twelve fits.

C.2.3 Further Numerical Tests

This subsections contains deals with three potential problems of the presented results and shows that they do not spoil the outcome.

Chiral Logarithms

The behaviour of the pseudoscalar mass in ChPT contains logarithms in the quenched theory as well as in full QCD. The full QCD chiral logarithms in m_{P} are small [126] because the dominant term is proportional to $m_{\mathrm{P}} \ln m_{\mathrm{P}}$. In quenched QCD there are additional logarithmic contribution, the *quenched chiral logarithms*. Still being a potential problem their behaviour is understood in quenched ChPT. We checked for deviations from the LO behaviour of m_{P} and found a rather inconclusive picture, Figure C.1a. There seems to be a trend in the data on the three coarser lattices which is absent at $L/a = 20$. A problem here is the lack of precision as the effect is supposed to be relatively small at such high quark masses.

Since we just had to interpolate to x_{ref} the possible (small) deviation from a linear behaviour of m_{P}^2 against m is irrelevant for the results on the renormalization factor Z_{S}. The slope is taken into account via a non-zero intercept in the fit.

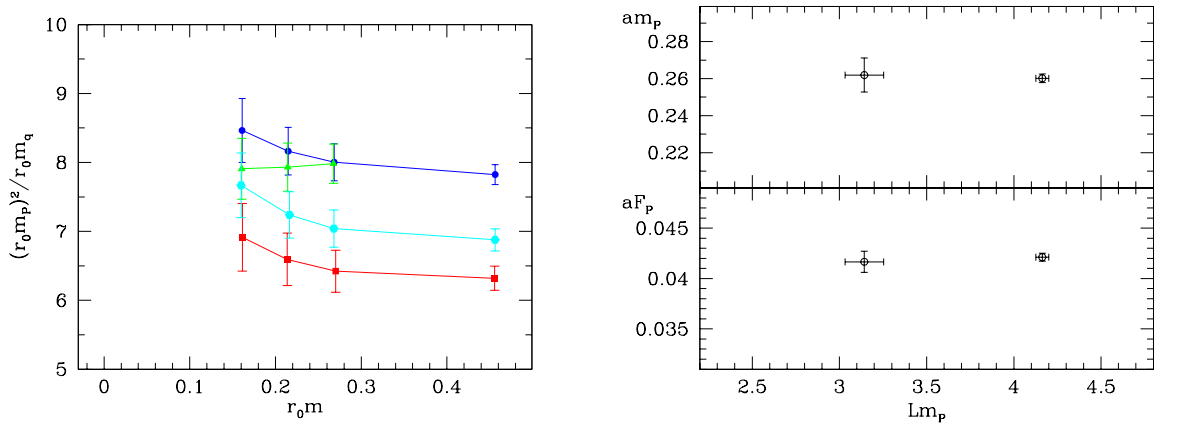

(a) Ratio $(r_0 m_\mathrm{P})^2 / r_0 m$ as a function of $r_0 m$

(b) Volume scaling of m_P and F_P at $a = 0.124\,\mathrm{fm}$ and at the lowest considered quark mass

Figure C.1: Chiral logarithms (a) and FVE (b) for the presented results.

Finite Volume Effects

Besides the remark in the beginning of the section it was also tested directly that finite volume effects are small in our computation. The comparison with lattice data at larger volume ($L = 1.9X$ fm) is performed at the coarsest lattice spacing. The underlying assumption here is that FVE are universal, that means they depend only on the volume and not on the lattice spacing. In a quenched study where the lattice spacing does not depend on the quark mass, the assumption seems to be well justified.

The data at $\beta = 5.8485$[1] and $L/a = 16$ come from a study of non-leptonic kaon decay, described in full detail in Chapter 4. As seen in Figure C.1b one can neglect the FVE compared to the statistical uncertainty.

Zero Mode Contribution to the PP correlator

The main reason to introduce the left-handed current in this project was to ensure that there is no dependence on topological zero modes. These zero modes appear at finite volume and their contribution can be seen as a potentially large FVE. We also considered the PP correlator which is dominated by zero modes in the chiral limit [114]. Here we want to check whether the effect of the zero modes can already be seen at the quark masses considered. Therefore we compare the pseudoscalar mass resulting from the two-correlators and plot the difference as a function of the bare quark mass for all four lattices, Figure C.2. The outcome is marginally consistent with zero. Again the limitations of the statistical precision prevent a clear statement for or against zero-mode effects. Since the difference is not randomly distributed around zero but always positive we conclude that there is a small effect already at these rather high quark

[1] The value of β is slightly different but resulting effect is negligible.

masses.

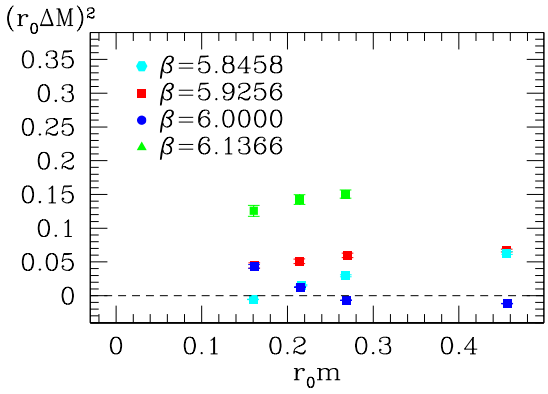

Figure C.2: Mass difference $\Delta M = m_{\mathrm{P}}^{PP} - m_{\mathrm{P}}^{PP}$ as a function of the quark mass on all four lattices.

D Kaon Decays, Numerical Details

D.1 Low Mode Averaging for Three-Point Functions

The mixed contributions to the low-mode averaged three-point functions $C_{1\mathrm{d}}$ and $C_{1\mathrm{c}}$ are given by

$$C^{\mathrm{hlll}}_{1\mathrm{d/c}} = \frac{1}{L^3}\left[a^{\mathrm{hlll}}_{1\mathrm{d/c}} + b^{\mathrm{hlll}}_{1\mathrm{d/c}} + c^{\mathrm{hlll}}_{1\mathrm{d/c}} + d^{\mathrm{hlll}}_{1\mathrm{d/c}}\right], \tag{D.1a}$$

$$C^{\mathrm{hhll}}_{1\mathrm{d/c}} = a^{\mathrm{hhll}}_{1\mathrm{d/c}} + b^{\mathrm{hhll}}_{1\mathrm{d/c}} + a^{\mathrm{hlhl}}_{1\mathrm{d/c}} + b^{\mathrm{hlhl}}_{1\mathrm{d/c}} + c^{\mathrm{hlhl}}_{1\mathrm{d/c}} + d^{\mathrm{hlhl}}_{1\mathrm{d/c}}, \tag{D.1b}$$

$$C^{\mathrm{hhhl}}_{1\mathrm{d/c}} = \frac{1}{L^3}\left[a^{\mathrm{hhhl}}_{1\mathrm{d/c}} + b^{\mathrm{hhhl}}_{1\mathrm{d/c}} + c^{\mathrm{hhhl}}_{1\mathrm{d/c}} + d^{\mathrm{hhhl}}_{1\mathrm{d/c}}\right]. \tag{D.1c}$$

In the following the expressions for the coefficient *a-d* are listed using the notations

$$\zeta_i(x) \equiv \sum_y P_- S_{\mathrm{h}}(x,y) P_+ \gamma_0 P_- \phi_i(y) \delta(y_0 - t_{\mathrm{fix}}), \tag{D.2}$$

$$\rho_a(x) \equiv P_-(S_{\mathrm{h}})_a(x,0) P_+ \eta_a, \tag{D.3}$$

$$\xi_a(x) \equiv (\delta^{(4)}(x)\delta_{ab})_{b=1,\ldots 6}, \quad \Xi_{ab}(x) \equiv \left[\xi_a(x)\gamma_\mu P_- \xi_b(x)\right], \tag{D.4}$$

$$\Phi^\mu_{ij}(x) \equiv \left[\phi^\dagger_i(x)\gamma_\mu P_- \phi_j(x)\right]. \tag{D.5}$$

The source field η_a is diagonal in Dirac and colour indices. The index a runs from 1 to 12; the two indices have been merged in to one. In practice only one chirality component is needed and therefore a runs from 1 to 6 in the following.

hlll-Contribution, colour-connected

$$a^{\mathrm{hlll}}_{1\mathrm{c}}(x_0 - z_0, -z_0) = \sum_{i,j,k=1}^{N_{\mathrm{low}}} \sum_{\vec{x},\vec{z}} \sum_{\mu=0}^{3} \left\{ \Phi^0_{ij}(x) \Phi^\mu_{jk}(z) \left[\zeta^\dagger_k(z)\gamma_\mu P_- \phi_i(z)\right] \right\} \tag{D.6a}$$

$$b^{\mathrm{hlll}}_{1\mathrm{c}}(x_0 - z_0, -z_0) = \sum_{i,j,k=1}^{N_{\mathrm{low}}} \sum_{\vec{x},\vec{z}} \sum_{\mu=0}^{3} \left\{ \Phi^0_{ij}(x) \left[\phi^\dagger_j(z)\gamma_\mu P_- \zeta_k(z)\right] \Phi^\mu_{ki}(z) \right\} \tag{D.6b}$$

$$c^{\mathrm{hlll}}_{1\mathrm{c}}(-z_0, x_0 - z_0) = \sum_{i,j,k=1}^{N_{\mathrm{low}}} \sum_{\vec{x},\vec{z}} \sum_{\mu=0}^{3} \left\{ \Phi^0_{ij}(x) \Phi^\mu_{jk}(z) \left[\zeta^\dagger_k(z)\gamma_\mu P_- \phi_i(z)\right] \right\} \tag{D.6c}$$

$$d^{\mathrm{hlll}}_{1\mathrm{c}}(-z_0, x_0 - z_0) = \sum_{i,j,k=1}^{N_{\mathrm{low}}} \sum_{\vec{x},\vec{z}} \sum_{\mu=0}^{3} \left\{ \Phi^0_{ij}(x) \left[\phi^\dagger_j(z)\gamma_\mu P_- \zeta_k(z)\right] \Phi^\mu_{ki}(z) \right\} \tag{D.6d}$$

hlll-Contribution, colour-disconnected

$$a_{1\mathrm{d}}^{\mathrm{hlll}}(x_0 - z_0, -z_0) = \sum_{i,j,k=1}^{N_{\mathrm{low}}} \sum_{\vec{x},\vec{z}} \sum_{\mu=0}^{3} \left\{ \Phi_{ij}^{0}(x) \Phi_{ji}^{\mu}(z) \left[\zeta_k^{\dagger}(z) \gamma_\mu P_- \phi_k(z) \right] \right\} \tag{D.7a}$$

$$b_{1\mathrm{d}}^{\mathrm{hlll}}(x_0 - z_0, -z_0) = \sum_{i,j,k=1}^{N_{\mathrm{low}}} \sum_{\vec{x},\vec{z}} \sum_{\mu=0}^{3} \left\{ \Phi_{ij}^{0}(x) \Phi_{ji}^{\mu}(z) \left[\phi_k^{\dagger}(z) \gamma_\mu P_- \zeta_k(z) \right] \right\} \tag{D.7b}$$

$$c_{1\mathrm{d}}^{\mathrm{hlll}}(-z_0, x_0 - z_0) = \sum_{i,j,k=1}^{N_{\mathrm{low}}} \sum_{\vec{x},\vec{z}} \sum_{\mu=0}^{3} \left\{ \Phi_{ij}^{0}(x) \Phi_{ji}^{\mu}(z) \left[\zeta_k^{\dagger}(z) \gamma_\mu P_- \phi_k(z) \right] \right\} \tag{D.7c}$$

$$d_{1\mathrm{d}}^{\mathrm{hlll}}(-z_0, x_0 - z_0) = \sum_{i,j,k=1}^{N_{\mathrm{low}}} \sum_{\vec{x},\vec{z}} \sum_{\mu=0}^{3} \left\{ \Phi_{ij}^{0}(x) \Phi_{ji}^{\mu}(z) \left[\phi_k^{\dagger}(z) \gamma_\mu P_- \zeta_k(z) \right] \right\} \tag{D.7d}$$

hhll-Contribution, colour-connected

$$a_{1\mathrm{c}}^{\mathrm{hhll}}(x_0, -z_0) = \sum_{i,j=1}^{N_{\mathrm{low}}} \sum_{a,b=1}^{6} \sum_{\vec{x},\vec{z}} \sum_{\mu=0}^{3} \left\{ \Phi_{ij}^{0}(x) \left[\phi_j^{\dagger}(z) \gamma_\mu P_- \rho_a(z) \right] \left[\rho_b^{\dagger}(z) \gamma_\mu P_- \phi_i(z) \right] \right\} \tag{D.8a}$$

$$b_{1\mathrm{c}}^{\mathrm{hhll}}(-z_0, x_0 - z_0) = \sum_{i,j=1}^{N_{\mathrm{low}}} \sum_{a,b=1}^{6} \sum_{\vec{x},\vec{z}} \sum_{\mu=0}^{3} \left\{ \Phi_{ij}^{0}(x) \left[\phi_j^{\dagger}(z) \gamma_\mu P_- \rho_a(z) \right] \left[\rho_b^{\dagger}(z) \gamma_\mu P_- \phi_i(z) \right] \right\} \tag{D.8b}$$

$$a_{1\mathrm{c}}^{\mathrm{hlhl}}(x_0, y_0) = \sum_{i,j=1}^{N_{\mathrm{low}}} \sum_{\vec{x},\vec{y}} \sum_{\mu=0}^{3} \left\{ \left[\phi_i(x) \gamma_0 P_- \rho_a(x) \right] \left[\rho_b(y) \gamma_0 P_- \phi_j(y) \right] \Xi_{ab}(0) \Phi_{ji}^{\mu}(0) \right\} \tag{D.9a}$$

$$\begin{aligned} b_{1\mathrm{c}}^{\mathrm{hlhl}}(x_0, y_0) = \sum_{i,j=1}^{N_{\mathrm{low}}} \sum_{\vec{x},\vec{y}} \sum_{\mu=0}^{3} \Big\{ & \left[\phi_i(x) \gamma_0 P_- \rho_a(x) \right] \left[\phi_j(y) \gamma_0 P_- \rho_b(y) \right] \\ & \times \left[\xi_a^{\dagger}(0) \gamma_\mu P_- \phi_j(0) \right] \left[\xi_b^{\dagger}(0) \gamma_\mu P_- \phi_i(0) \right] \Big\} \end{aligned} \tag{D.9b}$$

$$\begin{aligned} c_{1\mathrm{c}}^{\mathrm{hlhl}}(x_0, y_0) = \sum_{i,j=1}^{N_{\mathrm{low}}} \sum_{\vec{x},\vec{y}} \sum_{\mu=0}^{3} \Big\{ & \left[\rho_a(x) \gamma_0 P_- \phi_i(x) \right] \left[\rho_b(y) \gamma_0 P_- \phi_j(y) \right] \\ & \times \left[\phi_i^{\dagger}(0) \gamma_\mu P_- \xi_b(0) \right] \left[\phi_j(0) \gamma_\mu P_- \xi_a(0) \right] \Big\} \end{aligned} \tag{D.9c}$$

$$d_{1\mathrm{c}}^{\mathrm{hlhl}}(y_0, x_0) = \sum_{i,j=1}^{N_{\mathrm{low}}} \sum_{\vec{x},\vec{y}} \sum_{\mu=0}^{3} \left\{ \left[\phi_i(x) \gamma_0 P_- \rho_a(x) \right] \left[\rho_b(y) \gamma_0 P_- \phi_j(y) \right] \Phi_{ji}^{\mu}(0) \Xi_{ab}(0) \right\} \tag{D.9d}$$

hhll-Contribution, colour-disconnected

$$a_{1\mathrm{d}}^{\mathrm{hhll}}(x_0 - z_0, -z_0) = \sum_{i,j=1}^{N_{\mathrm{low}}} \sum_{a,b=1}^{6} \sum_{\vec{x},\vec{z}} \sum_{\mu=0}^{3} \left\{ \Phi_{ij}^{0}(x) \Phi_{ji}^{\mu}(z) \left[\rho_a^{\dagger}(z) \gamma_\mu P_- \rho_b(z) \right] \right\} \tag{D.10a}$$

$$b_{1\mathrm{d}}^{\mathrm{hhll}}(-z_0, x_0 - z_0) = \sum_{i,j,k=1}^{N_{\mathrm{low}}} \sum_{a,b=1}^{6} \sum_{\vec{x},\vec{z}} \sum_{\mu=0}^{3} \left\{ \Phi_{ij}^{0}(x) \Phi_{ji}^{\mu}(z) \left[\rho_a^{\dagger}(z) \gamma_\mu P_- \rho_b(z) \right] \right\} \tag{D.10b}$$

$$a_{1\mathrm{d}}^{\mathrm{hlhl}}(x_0,y_0) = \sum_{i,j=1}^{N_{\mathrm{low}}} \sum_{\vec{x},\vec{y}} \sum_{\mu=0}^{3} \Big\{ \Big[\phi_i(x)\gamma_0 P_- \rho_a(x)\Big] \Big[\rho_b(y)\gamma_0 P_- \phi_j(y)\Big] \times \Big[\xi_a(0)\gamma_\mu P_- \phi_i(0)\Big] \Big[\phi_j(0)\gamma_\mu P_- \xi_b(0)\Big] \Big\} \tag{D.11a}$$

$$b_{1\mathrm{d}}^{\mathrm{hlhl}}(x_0,y_0) = \sum_{i,j=1}^{N_{\mathrm{low}}} \sum_{\vec{x},\vec{y}} \sum_{\mu=0}^{3} \Big\{ \Big[\phi_i(x)\gamma_0 P_- \rho_a(x)\Big] \Big[\phi_i(y)\gamma_0 P_- \rho_b(y)\Big] \times \Big[\xi_a(0)\gamma_\mu P_- \phi_i(0)\Big] \Big[\xi_b(0)\gamma_\mu P_- \phi_j(0)\Big] \Big\} \tag{D.11b}$$

$$c_{1\mathrm{d}}^{\mathrm{hlhl}}(x_0,y_0) = \sum_{i,j=1}^{N_{\mathrm{low}}} \sum_{\vec{x},\vec{y}} \sum_{\mu=0}^{3} \Big\{ \Big[\rho_a(x)\gamma_0 P_- \phi_i(x)\Big] \Big[\rho_b(y)\gamma_0 P_- \phi_j(y)\Big] \times \Big[\phi_i(0)\gamma_\mu P_- \xi_a(0)\Big] \Big[\phi_j(0)\gamma_\mu P_- \xi_b(0)\Big] \Big\} \tag{D.11c}$$

$$d_{1\mathrm{d}}^{\mathrm{hlhl}}(y_0,x_0) = \sum_{i,j=1}^{N_{\mathrm{low}}} \sum_{\vec{x},\vec{y}} \sum_{\mu=0}^{3} \Big\{ \Big[\phi_i(x)\gamma_0 P_- \rho_a(x)\Big] \Big[\rho_b(y)\gamma_0 P_- \phi_j(y)\Big] \times \Big[\xi_a(0)\gamma_\mu P_- \phi_i(0)\Big] \Big[\phi_j(0)\gamma_\mu P_- \xi_b(0)\Big] \Big\} \tag{D.11d}$$

hhhl-Contribution, colour-connected

$$a_{1\mathrm{d}}^{\mathrm{hhhl}}(x_0,y_0) = \sum_{i=1}^{N_{\mathrm{low}}} \sum_{a,b,c=1}^{6} \sum_{\vec{x},\vec{y}} \sum_{\mu=0}^{3} \Big\{ \Big[\phi_i^\dagger(x)\gamma_0 P_- \rho_a(x)\Big] \Big[\rho_b^\dagger(y)\gamma_\mu P_- \rho_c(y)\Big] \times \Xi_{ba}(0) \Big[\xi_c^\dagger(0)\gamma_\mu P_- \phi_i(0)\Big] \Big\} \tag{D.12a}$$

$$b_{1\mathrm{d}}^{\mathrm{hhhl}}(x_0,y_0) = \sum_{i=1}^{N_{\mathrm{low}}} \sum_{a,b,c=1}^{6} \sum_{\vec{x},\vec{y}} \sum_{\mu=0}^{3} \Big\{ \Big[\rho_a^\dagger(x)\gamma_0 P_- \phi_i(x)\Big] \Big[\rho_b^\dagger(z)\gamma_\mu P_- \rho_c(z)\Big] \times \Big[\phi_i^\dagger(0)\gamma_\mu P_- \xi_b(0)\Big] \Xi_{ca}(0) \Big\} \tag{D.12b}$$

$$c_{1\mathrm{d}}^{\mathrm{hhhl}}(y_0,x_0) = \sum_{i=1}^{N_{\mathrm{low}}} \sum_{a,b,c=1}^{6} \sum_{\vec{x},\vec{y}} \sum_{\mu=0}^{3} \Big\{ \Big[\phi_i^\dagger(x)\gamma_0 P_- \rho_a(x)\Big] \Big[\rho_b^\dagger(0)\gamma_\mu P_- \rho_c(0)\Big] \times \Xi_{ab}(0) \Big[\xi_c^\dagger(0)\gamma_\mu P_- \phi_i(z)\Big] \Big\} \tag{D.12c}$$

$$d_{1\mathrm{d}}^{\mathrm{hhhl}}(y_0,x_0) = \sum_{i=1}^{N_{\mathrm{low}}} \sum_{a,b,c=1}^{6} \sum_{\vec{x},\vec{y}} \sum_{\mu=0}^{3} \Big\{ \Big[\rho_a^\dagger(x)\gamma_0 P_- \phi_i(x)\Big] \Big[\rho_b^\dagger(z)\gamma_\mu P_- \rho_c(z)\Big] \times \Big[\phi_i^\dagger(0)\gamma_\mu P_- \xi_b(0)\Big] \Xi_{ca}(0) \Big\} \tag{D.12d}$$

hhhl-Contribution, colour-disconnected

$$a_{1\mathrm{d}}^{\mathrm{hhhl}}(x_0,y_0) = \sum_{i=1}^{N_{\mathrm{low}}} \sum_{a,b,c=1}^{6} \sum_{\vec{x},\vec{z}} \sum_{\mu=0}^{3} \Big\{ \Big[\phi_i^\dagger(x)\gamma_0 P_- \rho_a(x)\Big] \Big[\rho_b^\dagger(z)\gamma_\mu P_- \rho_c(z)\Big] \times \Big[\xi_a^\dagger(0)\gamma_\mu P_- \phi_i(0)\Big] \Xi_{cb}(0) \Big\} \tag{D.13a}$$

$$b_{1\mathrm{d}}^{\mathrm{hhhl}}(x_0,y_0) = \sum_{i=1}^{N_{\mathrm{low}}} \sum_{a,b,c=1}^{6} \sum_{\vec{x},\vec{z}} \sum_{\mu=0}^{3} \Big\{ \Big[\rho_a^\dagger(x)\gamma_0 P_- \phi_i(x)\Big] \Big[\rho_b^\dagger(z)\gamma_\mu P_- \rho_c(z)\Big] \times \Big[\phi_i^\dagger(0)\gamma_\mu P_- \xi_a(0)\Big] \Xi_{cb}(0) \Big\} \tag{D.13b}$$

$$c_{1\mathrm{d}}^{\mathrm{hhhl}}(y_0,x_0) = \sum_{i=1}^{N_{\mathrm{low}}} \sum_{a,b,c=1}^{6} \sum_{\vec{x},\vec{z}} \sum_{\mu=0}^{3} \Big\{ \Big[\phi_i^\dagger(x)\gamma_0 P_- \rho_a(x)\Big] \Big[\rho_b^\dagger(z)\gamma_\mu P_- \rho_c(z)\Big] \times \Big[\xi_a^\dagger(z)\gamma_\mu P_- \phi_i(0)\Big] \Xi_{cb}(0) \Big\} \tag{D.13c}$$

$$d_{1\mathrm{d}}^{\mathrm{hhhl}}(y_0,x_0) = \sum_{i=1}^{N_{\mathrm{low}}} \sum_{a,b,c=1}^{6} \sum_{\vec{x},\vec{z}} \sum_{\mu=0}^{3} \Big\{ \Big[\rho_a^\dagger(x)\gamma_0 P_- \phi_i(x)\Big] \Big[\rho_b^\dagger(z)\gamma_\mu P_- \rho_c(z)\Big] \times \Big[\phi_i^\dagger(0)\gamma_\mu P_- \xi_a(0)\Big] \Xi_{cb}(0) \Big\} \tag{D.13d}$$

D.2 Complete Results in the ϵ-Regime

In the tables below the results on both lattice for the ϵ-regime masses are listed with the exception of $am = 0.003$ on lattice B which is given in Table 6.2.

$\lvert\nu\rvert$	# cfgs	R_+	R_-	R_-/R_+	R_+/R_-
2	151	0.52(19)(17)	2.34(97)(86)	4.5(3.3)(1.9)	0.140(73)
3	130	0.82(13)(15)	3.69(63)(66)	4.5(1.2)(0.8)	0.243(68)
4	125	0.68(13)(12)	3.47(48)(50)	5.1(1.6)(1.0)	0.185(58)
5	101	0.67(11)(10)	2.00(69)(79)	3.0(1.1)(1.1)	0.34(18)
6	87	0.606(94)(88)	2.15(31)(37)	3.57(72)(68)	0.318(86)
7	86	0.55(10)(11)	2.64(26)(28)	4.8(1.4)(0.9)	0.170(51)
8	66	0.53(13)(11)	2.18(30)(28)	4.2(1.5)(1.1)	0.341(73)
9	52	0.36(11)(11)	2.64(60)(61)	7.8(5.3)(3.1)	0.247(55)
10	29	0.57(10)(10)	1.89(42)(50)	3.4(1.1)(1.0)	0.36(14)
2-8	w.a.	0.623(46)(47)	2.36(15)	3.57(42)	0.220(26)

Table D.1: Results for the ratios defined in Eq. (6.18) on the lattice B, $L/a = 16$ at $am = 0.002$. The first error is the upper and the second the lower bootstrap error.

am	$\lvert\nu\rvert$	# cfgs	R_+	R_-	R_-/R_+	R_+/R_-
0.007	0	70	0.35(14)(18)	−0.3(1.8)(2.2)	−1(6)(7)	−1.3(1.8)(0.9)
	1	154	0.52(15)(14)	0.6(0.8)(0.9)	1.1(1.9)(1.8)	1.0(0.3)(1.8)
	2	145	0.49(10)(10)	3.22(72)(4)	6.6(2.5)(1.8)	0.152(60)(40)
	3	105	0.31(11)(9)	3.08(70)(64)	9.8(4.1)(2.5)	0.102(36)(28)
	4	76	0.542(87)(88)	1.97(48)(50)	3.6(1.3)(1.1)	0.28(12)(7)
	5	46	0.46(12)(12)	2.74(37)(40)	6.2(2.7)(1.6)	0.171(67)(47)
	6	34	0.59(13)(12)	1.09(40)(40)	1.9(1.1)(0.8)	0.56(43)(22)
	7	26	0.65(14)(14)	2.65(50)(62)	4.1(1.2)(1.0)	0.250(89)(57)
	8	14	0.58(12)(14)	2.56(56)(76)	4.4(1.9)(1.4)	0.23(12)(7)
	2-8	669	0.497(41)(42)	2.16(19)(20)	3.45(62)(62)	0.147(25)(25)
0.005	0	70	0.39(21)(30)	−1.4(3.3)(4.3)	−4(13)(12)	−0.3(0.5)(0.1)
	1	154	0.57(19)(17)	−0.2(1.2)(1.5)	−0.4(2.5)(2.4)	−6.9(7.9)(5.9)
	2	145	0.50(15)(12)	3.7(1.0)(1.0)	7.4(3.2)(2.2)	0.136(59)(40)
	3	105	0.24(15)(12)	2.6(1.1)(1.0)	10.9(6.3)(4.3)	0.092(50)(37)
	4	76	0.545(91)(93)	1.86(52)(53)	3.4(1.4)(1.1)	0.30(16)(9)
	5	46	0.44(13)(12)	2.81(39)(41)	6.6(3.1)(1.8)	0.161(68)(46)
	6	34	0.58(13)(12)	1.09(41)(40)	1.89(1.2)(0.8)	0.55(43)(22)
	7	26	0.66(14)(15)	2.74(54)(68)	4.2(1.3)(1.1)	0.242(88)(56)
	8	14	0.58(12)(14)	2.51(60)(80)	4.3(2.0)(1.5)	0.23(13)(7)
	2-8	669	0.510(44)(44)	2.12(21)(21)	3.52(69)(68)	0.199(39)(39)
0.003	0	70	0.6(0.5)(0.7)	−3(10)(12)	−5(25)(20)	−0.2(0.4)(0.1)
	1	154	0.62(22)(20)	−1.0(1.9)(2.1)	−1.7(3.3)(3.6)	−0.6(1.1)(0.2)
	2	145	0.52(14)(13)	4.5(1.4)(1.4)	8.6(3.9)(2.8)	0.117(59)(34)
	3	105	0.1(0.2)(0.2)	1.3(2.5)(2.1)	8.2(10.2)(5.6)	0.13(5)(10)
	4	76	0.55(9)(10)	1.73(58)(58)	3.2(1.5)(1.2)	0.32(21)(10)
	5	46	0.43(13)(12)	2.86(40)(43)	6.9(3.5)(2.0)	0.153(67)(45)
	6	34	0.58(13)(13)	1.10(42)(41)	1.9(1.1)(0.8)	0.54(43)(22)
	7	26	0.66(15)(15)	2.80(56)(73)	4.3(1.3)(1.1)	0.237(88)(54)
	8	14	0.58(12)(13)	2.47(64)(81)	4.3(2.0)(1.6)	0.24(14)(7)
	0-8	669	0.528(49)(50)	2.11(23)(23)	3.72(74)(76)	0.200(44)(44)

Table D.2: Results for the ratios defined in Eq. (6.18) on lattice A, $L/a = 12$, for all three ϵ-regime masses. Again, the first error is the upper and the second the lower bootstrap error.

E ChPT for Zero-Mode Saturated Correlators

E.1 Notations for ChPT in the ϵ-regime

The partition function Z_0 can be split into $Z_0 = Z_\theta(\mu) \cdot Z_\xi$, where

$$Z_\xi = \int [\mathrm{d}\xi] \exp\left\{ -\int \mathrm{d}^4x \, \mathrm{Tr}\left(\partial_\mu \xi \partial_\mu \xi\right)\right\}, \tag{E.1a}$$

$$Z_\theta(\mu) = \int\limits_{\mathrm{SU}(N)} \mathrm{d}U_0 \exp\left\{\mu \, \mathrm{Re}\ \mathrm{Tr}\left(U_\theta U_0\right)\right\}. \tag{E.1b}$$

The free propagator for the ξ-field is then given by

$$\begin{aligned} \frac{1}{Z_\xi} \int [\mathrm{d}\xi] \xi(x)_{\alpha\beta} \xi(0)_{\gamma\delta} \exp\left\{ -\int \mathrm{d}^4x \, \mathrm{Tr}(\partial_\mu \xi \partial_\mu \xi)\right\} \\ = \frac{1}{2}\left[\delta_{\alpha\delta}\delta_{\gamma\beta} G(x) - \delta_{\alpha\beta}\delta_{\gamma\delta} E(x)\right], \end{aligned} \tag{E.2}$$

where

$$G(x) = \frac{1}{V} \sum_{n\in\mathbb{Z}} \left(1 - \delta^{(4)}_{n,0}\right) \frac{\mathrm{e}^{\mathrm{i}px}}{p^2}, \tag{E.3a}$$

$$E(x) = G(x)/N \quad \text{(unquenched)}, \tag{E.3b}$$

$$E(x) = \frac{\alpha}{2N_\mathrm{c}} G(x) + \frac{m_0^2}{2N_\mathrm{c}} F(x) \quad \text{(quenched)}, \tag{E.3c}$$

$$F(x) = \frac{1}{V} \sum_{n\in\mathbb{Z}} \left(1 - \delta^{(4)}_{n,0}\right) \frac{\mathrm{e}^{\mathrm{i}px}}{p^4}. \tag{E.3d}$$

The integration over the spatial volume simplifies the expressions and it is convenient to introduce the functions $h_1(\tau)$ and $h_2(\tau)$ with $\tau = x_0/T$,

$$\int \mathrm{d}^3 G(x) = T h_1(\tau), \qquad h_1(\tau) \equiv \frac{1}{2}\left[\left(\tau - \frac{1}{2}\right)^2 - \frac{1}{12}\right], \tag{E.4a}$$

$$\int \mathrm{d}^3 F(x) = -T^3 h_2(\tau) \qquad h_2(\tau) \equiv \frac{1}{24}\left[\tau^2 (\tau-1)^2 - \frac{1}{30}\right], \tag{E.4b}$$

For higher orders in ϵ also the function g_1 is needed,

$$g_1(\tau) \equiv \left[h_1(\tau)\right]^2 + \sum_{\vec{n}\neq 0} \left[\frac{\cosh\left(p(\tau - 1/2)\right)}{2p \sinh\left(p/2\right)}\right]^2, \qquad p = 2\pi \frac{T}{L}\left[\sum_{i=1}^{3} n_i^2\right]^{1/2}. \tag{E.5}$$

The non-trivial part in the computation are the zero mode integral which must be performed exactly. For the LO result on $\mathcal{J}^1\mathcal{P}$ only the most basic integral is needed. The following results are published in [114].

In the non-singlet case one can use the completeness relation for the generators T^a of SU(N) to obtain $\mathrm{Tr}(T^a U_0' T^a) = \frac{1}{2N}\mathrm{Tr}(U_0')$. For the integral one gets

$$\left\langle \mathrm{Tr}(U_0') \right\rangle_\nu^\mu = N\left[\sigma_\nu(\mu) - \frac{\nu}{\mu}\right] \overset{\mu\to 0}{\approx} \frac{N}{\mu}\left(|\nu| - \nu\right), \tag{E.6}$$

with σ_ν defined in Eq. (3.22). For the complex conjugate of U_0' the result is the same up to a sign in ν, $\nu \to -\nu$. Therefore the real part amounts to

$$\mathrm{Re}\left\langle \mathrm{Tr}\left(U_0'\right)\right\rangle_\nu^\mu = \frac{1}{2}N\left[\sigma_\nu(\mu) + \sigma_{-\nu}(\mu)\right] \overset{\mu\to 0}{\approx} \frac{N}{\mu}|\nu|. \tag{E.7}$$

E.2 NNLO Expressions for the PP-Correlator

As stated in Section 7.1 is is necessary to consider the time derivatives of the correlators $\mathcal{A}$ and $\tilde{\mathcal{A}}$ to obtain non-trivial results. One gets [114]

$$\begin{aligned} F^2 A'(x_0) = 2|\nu|\Bigg[&\left(|\nu| + \frac{\alpha}{2N_\mathrm{c}} - \frac{\beta_1}{F^2\sqrt{\overline{V}}}\right) h_1'(\tau) \\ &+ \frac{T^2}{F^2 V}\left(2\nu^2 + \frac{7}{3} - 2\left\langle\nu^2\right\rangle\right) h_2'(\tau) + \frac{T^2}{2F^2V} g_1'(\tau)\Bigg], \end{aligned} \tag{E.8a}$$

$$\begin{aligned} F^2 \tilde{A}'(x_0) = -2|\nu|\Bigg[&\left(1 + |\nu|\left(+\frac{\alpha}{2N_\mathrm{c}} - \frac{\beta_1}{F^2\sqrt{\overline{V}}}\right)\right) h_1'(\tau) \\ &+ \frac{T^2}{F^2 V}\left(\frac{13}{3}|\nu| - 2|\nu|\left\langle\nu^2\right\rangle\right) h_2'(\tau) + \frac{T^2}{2F^2V} g_1'(\tau)\Bigg], \end{aligned} \tag{E.8b}$$

with $\tau = x_0/T$. The functions h_1, h_2 are defined in Eq. (E.4) and g_1 in Eq. (E.5). The expressions depend also on the *singlet coupling* α which was introduced in Eq. (3.4). The expectation value $\left\langle v^2\right\rangle$ of the squared topological charge appears because the singlet mass m_0 has been exchanged according to the Witten-Veneziano relation $m_0^2 F^2 = 4N_\mathrm{c}\left\langle\nu^2\right\rangle/V$. The additional quenched LECs which show up complicate the analysis. In the full theory the result depends on F only at this order [114].

Bibliography

[1] K. G. Wilson, *Confinement of Quarks*, Phys. Rev. D10 (1974) 2445–2459.

[2] M. Lüscher and P. Weisz, *Scaling Laws and Triviality Bounds in the Lattice phi**4 Theory. 1. One Component Model in the Symmetric Phase*, Nucl. Phys. B290 (1987) 25.

[3] M. Creutz, *Monte Carlo Study of Quantized SU(2) Gauge Theory*, Phys. Rev. D21 (1980) 2308–2315.

[4] H. B. Nielsen and M. Ninomiya, *No Go Theorem for Regularizing Chiral Fermions*, Phys. Lett. B105 (1981) 219.

[5] P. H. Ginsparg and K. G. Wilson, *A Remnant of Chiral Symmetry on the Lattice*, Phys. Rev. D25 (1982) 2649.

[6] K. Symanzik, *Continuum Limit and Improved Action in Lattice Theories. 1. Principles and phi**4 Theory*, Nucl. Phys. B226 (1983) 187.

[7] Y. Iwasaki, *Renormalization Group Analysis of Lattice Theories and Improved Lattice Action: Two-Dimensional Nonlinear O(N) Sigma Model*, Nucl. Phys. B258 (1985) 141–156.

[8] M. Lüscher and P. Weisz, *On-Shell Improved Lattice Gauge Theories*, Commun. Math. Phys. 97 (1985) 59.

[9] K. G. Wilson, *Quarks and Strings on a Lattice*, New Phenomena In Subnuclear Physics. Part A. Proceedings of the First Half of the 1975 International School of Subnuclear Physics, Erice, Sicily, July 11 - August 1, 1975, ed. A. Zichichi, Plenum Press, New York, 1977, p. 69, CLNS-321.

[10] M. Bochicchio, L. Maiani, G. Martinelli, G. C. Rossi and M. Testa, *Chiral Symmetry on the Lattice with Wilson Fermions*, Nucl. Phys. B262 (1985) 331.

[11] B. Sheikholeslami and R. Wohlert, *Improved Continuum Limit Lattice Action for QCD with Wilson Fermions*, Nucl. Phys. B259 (1985) 572.

[12] ALPHA Collaboration, R. Frezzotti, P. A. Grassi, S. Sint and P. Weisz, *Lattice QCD with a Chirally Twisted Mass Term*, JHEP 08 (2001) 058 [`hep-lat/0101001`].

[13] R. Frezzotti and G. C. Rossi, *Chirally Improving Wilson Fermions. I: O(a) Improvement*, JHEP 08 (2004) 007 [`hep-lat/0306014`].

[14] J. B. Kogut and L. Susskind, *Hamiltonian Formulation of Wilson's Lattice Gauge Theories*, Phys. Rev. D11 (1975) 395.

[15] L. Susskind, *Lattice Fermions*, Phys. Rev. D16 (1977) 3031–3039.

[16] E. Marinari, G. Parisi and C. Rebbi, *Monte Carlo Simulation of the Massive Schwinger Model*, Nucl. Phys. B190 (1981) 734.

[17] MILC Collaboration, C. Aubin *et. al.*, *Light Pseudoscalar Decay Constants, Quark Masses, and Low Energy Constants from Three-Flavor Lattice QCD*, Phys. Rev. D70 (2004) 114501 [hep-lat/0407028].

[18] B. Bunk, M. Della Morte, K. Jansen and F. Knechtli, *Locality with Staggered Fermions*, Nucl. Phys. B697 (2004) 343–362 [hep-lat/0403022].

[19] S. Dürr, C. Hoelbling and U. Wenger, *Staggered Eigenvalue Mimicry*, Phys. Rev. D70 (2004) 094502 [hep-lat/0406027].

[20] S. Dürr, *Theoretical Issues with Staggered Fermion Simulations*, PoS LAT2005 (2005) 021 [hep-lat/0509026].

[21] Y. Shamir, *Locality of the Fourth Root of the Staggered-Fermion Determinant: Renormalization-Group Approach*, Phys. Rev. D71 (2005) 034509 [hep-lat/0412014].

[22] M. Lüscher, *Exact Chiral Symmetry on the Lattice and the Ginsparg- Wilson Relation*, Phys. Lett. B428 (1998) 342–345 [hep-lat/9802011].

[23] P. Hasenfratz, V. Laliena and F. Niedermayer, *The Index Theorem in QCD with a Finite Cut-Off*, Phys. Lett. B427 (1998) 125–131 [hep-lat/9801021].

[24] M. F. Atiyah and I. M. Singer, *The Index of Elliptic Operators. 5*, Annals Math. 93 (1971) 139–149.

[25] H. Neuberger, *Exactly Massless Quarks on the Lattice*, Phys. Lett. B417 (1998) 141–144 [hep-lat/9707022].

[26] H. Neuberger, *More about Exactly Massless Quarks on the Lattice*, Phys. Lett. B427 (1998) 353–355 [hep-lat/9801031].

[27] P. Hernández, K. Jansen and M. Lüscher, *Locality Properties of Neuberger's Lattice Dirac Operator*, Nucl. Phys. B552 (1999) 363–378 [hep-lat/9808010].

[28] M. Golterman, Y. Shamir and B. Svetitsky, *Mobility Edge in Lattice QCD*, Phys. Rev. D71 (2005) 071502 [hep-lat/0407021].

[29] D. B. Kaplan, *A Method for Simulating Chiral Fermions on the Lattice*, Phys. Lett. B288 (1992) 342–347 [hep-lat/9206013].

[30] V. Furman and Y. Shamir, *Axial Symmetries in Lattice QCD with Kaplan Fermions*, Nucl. Phys. B439 (1995) 54–78 [hep-lat/9405004].

[31] Y. Shamir, *Chiral Fermions from Lattice Boundaries*, Nucl. Phys. B406 (1993) 90–106 [hep-lat/9303005].

[32] S. Aoki, T. Izubuchi, Y. Kuramashi and Y. Taniguchi, *Domain Wall Fermions in Quenched Lattice QCD*, Phys. Rev. D62 (2000) 094502 [hep-lat/0004003].

[33] UKQCD Collaboration, D. J. Antonio *et. al.*, *Light Meson Masses and Decay Constants in 2+1 Flavour Domain Wall QCD*, PoS LAT2005 (2005) 080 [hep-lat/0512009].

[34] P. Hasenfratz and F. Niedermayer, *Perfect Lattice Action for Asymptotically Free Theories*, Nucl. Phys. B414 (1994) 785–814 [hep-lat/9308004].

[35] Y. Aoki *et. al.*, *Lattice QCD with Two Dynamical Flavors of Domain Wall Fermions*, Phys. Rev. D72 (2005) 114505 [hep-lat/0411006].

[36] A. Hasenfratz, P. Hasenfratz and F. Niedermayer, *Simulating Full QCD with the Fixed Point Action*, Phys. Rev. D72 (2005) 114508 [hep-lat/0506024].

[37] A. D. Kennedy, *Algorithms for Lattice QCD with Dynamical Fermions*, Nucl. Phys. Proc. Suppl. 140 (2005) 190–203 [hep-lat/0409167].

[38] HPQCD Collaboration, C. T. H. Davies *et. al.*, *High-Precision Lattice QCD Confronts Experiment*, Phys. Rev. Lett. 92 (2004) 022001 [hep-lat/0304004].

[39] M. Lüscher, *Schwarz-Preconditioned HMC Algorithm for Two-Flavour Lattice QCD*, Comput. Phys. Commun. 165 (2005) 199–220 [hep-lat/0409106].

[40] C. Urbach, K. Jansen, A. Shindler and U. Wenger, *HMC Algorithm with Multiple Time Scale Integration and Mass Preconditioning*, Comput. Phys. Commun. 174 (2006) 87–98 [hep-lat/0506011].

[41] S. Schaefer and T. A. DeGrand, *Dynamical Overlap Fermions: Simulations and Physics Results*, PoS LAT2005 (2005) 140 [hep-lat/0508025].

[42] H. Fukaya, S. Hashimoto, T. Hirohashi, K. Ogawa and T. Onogi, *Topology Conserving Gauge Action and the Overlap-Dirac Operator*, Phys. Rev. D73 (2006) 014503 [hep-lat/0510116].

[43] G. I. Egri, Z. Fodor, S. D. Katz and K. K. Szabo, *Topology with Dynamical Overlap Fermions*, JHEP 01 (2006) 049 [hep-lat/0510117].

[44] CP-PACS Collaboration, S. Aoki *et. al.*, *Light Hadron Spectrum and Quark Masses from Quenched Lattice QCD*, Phys. Rev. D67 (2003) 034503 [hep-lat/0206009].

[45] CP-PACS Collaboration, T. Ishikawa *et. al.*, *Light Hadron Spectrum and Quark Masses in 2+1 Flavor QCD*, PoS LAT2005 (2005) 057 [hep-lat/0509142].

[46] J. Goldstone, *Field Theories with 'Superconductor' Solutions*, Nuovo Cim. 19 (1961) 154–164.

[47] S. Weinberg, *Nonlinear Realizations of Chiral Symmetry*, Phys. Rev. 166 (1968) 1568–1577.

[48] J. Gasser and H. Leutwyler, *Chiral Perturbation Theory to One Loop*, Ann. Phys. 158 (1984) 142.

[49] C. W. Bernard and M. F. L. Golterman, *Chiral Perturbation Theory for the Quenched Approximation of QCD*, Phys. Rev. D46 (1992) 853–857 [hep-lat/9204007].

[50] J. Bijnens, *Chiral Perturbation Theory Beyond One Loop*, hep-ph/0604043.

[51] ALPHA Collaboration, J. Heitger, R. Sommer and H. Wittig, *Effective Chiral Lagrangians and Lattice QCD*, Nucl. Phys. B588 (2000) 377–399 [hep-lat/0006026].

[52] G. Rupak and N. Shoresh, *Chiral perturbation theory for the wilson lattice action*, Phys. Rev. D66 (2002) 054503 [hep-lat/0201019].

[53] G. Münster and C. Schmidt, *Chiral Perturbation Theory for Lattice QCD with a Twisted Mass Term*, Europhys. Lett. 66 (2004) 652–656 [hep-lat/0311032].

[54] W.-J. Lee and S. R. Sharpe, *Partial flavor symmetry restoration for chiral staggered fermions*, Phys. Rev. D60 (1999) 114503 [hep-lat/9905023].

[55] C. Aubin and C. Bernard, *Pion and Kaon Masses in Staggered Chiral Perturbation Theory*, Phys. Rev. D68 (2003) 034014 [hep-lat/0304014].

[56] J. Gasser and H. Leutwyler, *Spontaneously Broken Symmetries: Effective Lagrangians at Finite Volume*, Nucl. Phys. B307 (1988) 763.

[57] H. Leutwyler and A. Smilga, *Spectrum of Dirac Operator and Role of Winding Number in QCD*, Phys. Rev. D46 (1992) 5607–5632.

[58] F. C. Hansen, *Finite Size Effects in Spontaneously Broken SU(N) x SU(N) Theories*, Nucl. Phys. B345 (1990) 685–708.

[59] W. Bietenholz, T. Chiarappa, K. Jansen, K. I. Nagai and S. Shcheredin, *Axial Correlation Functions in the epsilon-Regime: A Numerical Study with Overlap Fermions*, JHEP 02 (2004) 023 [hep-lat/0311012].

[60] T. DeGrand and S. Schaefer, *Improving Meson Two-Point Functions in Lattice QCD*, Comput. Phys. Commun. 159 (2004) 185–191 [hep-lat/0401011].

[61] L. Giusti, P. Hernández, M. Laine, P. Weisz and H. Wittig, *Low-energy Couplings of QCD from Current Correlators near the Chiral Limit*, JHEP 04 (2004) 013 [hep-lat/0402002].

[62] L. Giusti, P. Hernández, M. Laine, P. Weisz and H. Wittig, *A Strategy to Study the Role of the Charm Quark in Explaining the Delta(I) = 1/2 Rule*, JHEP 11 (2004) 016 [hep-lat/0407007].

[63] M. Gell-Mann, R. J. Oakes and B. Renner, *Behavior of Current Divergences under SU(3) x SU(3)*, Phys. Rev. 175 (1968) 2195–2199.

[64] L. Giusti, F. Rapuano, M. Talevi and A. Vladikas, *The QCD Chiral Condensate from the Lattice*, Nucl. Phys. B538 (1999) 249–277 [hep-lat/9807014].

[65] P. Hernández, K. Jansen and L. Lellouch, *Finite-size Scaling of the Quark Condensate in Quenched Lattice QCD*, Phys. Lett. B469 (1999) 198–204 [hep-lat/9907022].

[66] T. Blum *et. al.*, *Quenched Lattice QCD with Domain Wall Fermions and the Chiral Limit*, Phys. Rev. D69 (2004) 074502 [hep-lat/0007038].

[67] MILC Collaboration, T. DeGrand, *A Variant Approach to the Overlap Action*, Phys. Rev. D63 (2001) 034503 [hep-lat/0007046].

[68] L. Giusti, C. Hoelbling and C. Rebbi, *Light Quark Masses with Overlap Fermions in Quenched QCD*, Phys. Rev. D64 (2001) 114508 [hep-lat/0108007].

[69] P. Hasenfratz, S. Hauswirth, T. Jörg, F. Niedermayer and K. Holland, *Testing the Fixed-point QCD Action and the Construction of Chiral Currents*, Nucl. Phys. B643 (2002) 280–320 [hep-lat/0205010].

[70] D. Bećirević and V. Lubicz, *Estimate of the Chiral Condensate in Quenched Lattice QCD*, Phys. Lett. B600 (2004) 83–90 [hep-ph/0403044].

[71] C. McNeile, *An Estimate of the Chiral Condensate from Unquenched Lattice QCD*, Phys. Lett. B619 (2005) 124–128 [hep-lat/0504006].

[72] E. V. Shuryak and J. J. M. Verbaarschot, *Random Matrix Theory and Spectral Sum Rules for the Dirac Operator in QCD*, Nucl. Phys. A560 (1993) 306–320 [hep-th/9212088].

[73] J. J. M. Verbaarschot and I. Zahed, *Spectral density of the qcd dirac operator near zero virtuality*, Phys. Rev. Lett. 70 (1993) 3852–3855 [hep-th/9303012].

[74] J. J. M. Verbaarschot, *The Spectrum of the QCD Dirac Operator and Chiral Random Matrix Theory: The Threefold Way*, Phys. Rev. Lett. 72 (1994) 2531–2533 [hep-th/9401059].

[75] L. Giusti, M. Lüscher, P. Weisz and H. Wittig, *Lattice QCD in the epsilon-Regime and Random Matrix Theory*, JHEP 11 (2003) 023 [hep-lat/0309189].

[76] J. J. M. Verbaarschot and I. Zahed, *Random Matrix Theory and QCD in Three-Dimensions*, Phys. Rev. Lett. 73 (1994) 2288–2291 [hep-th/9405005].

[77] P. H. Damgaard and S. M. Nishigaki, *Distribution of the k-th Smallest Dirac Operator Eigenvalue*, Phys. Rev. D63 (2001) 045012 [hep-th/0006111].

[78] L. Giusti, C. Hoelbling, M. Lüscher and H. Wittig, *Numerical Techniques for Lattice QCD in the epsilon- Regime*, Comput. Phys. Commun. 153 (2003) 31–51 [hep-lat/0212012].

[79] Y. Saad, *Iterative Methods for Sparse Linear Systems*. SIAM, second ed., 2003. First edition available at http://www-users.cs.umn.edu/~saad/books.html.

[80] C. Pena and J. Wennekers, *Testing the Efficiency of Low Mode Averaging*, unpublished notes (2004).

[81] J. Wennekers and H. Wittig, *On the Renormalized Scalar Density in Quenched QCD*, JHEP 09 (2005) 059 [hep-lat/0507026].

[82] M. Lüscher, R. Narayanan, P. Weisz and U. Wolff, *The Schrödinger Functional: A Renormalizable Probe for non-Abelian Gauge Theories*, Nucl. Phys. B384 (1992) 168–228 [hep-lat/9207009].

[83] S. Sint, *On the Schrödinger Functional in QCD*, Nucl. Phys. B421 (1994) 135–158 [hep-lat/9312079].

[84] K. Jansen *et. al.*, *Non-Perturbative Renormalization of Lattice QCD at all Scales*, Phys. Lett. B372 (1996) 275–282 [hep-lat/9512009].

[85] Y. Taniguchi, *Schrödinger Functional Formalism with Ginsparg-Wilson Fermion*, JHEP 12 (2005) 037 [hep-lat/0412024].

[86] S. Sint, *The Schrödinger Functional with Chirally Rotated Boundary Conditions*, PoS LAT2005 (2005) 235 [hep-lat/0511034].

[87] M. Lüscher, *The Schrödinger Functional in Lattice QCD with Exact Chiral Symmetry*, hep-lat/0603029.

[88] P. Hernández, K. Jansen, L. Lellouch and H. Wittig, *Non-perturbative Renormalization of the Quark Condensate in Ginsparg-Wilson Regularizations*, JHEP 07 (2001) 018 [hep-lat/0106011].

[89] ALPHA and UKQCD Collaboration, J. Garden, J. Heitger, R. Sommer and H. Wittig, *Precision Computation of the Strange Quark's Mass in Quenched QCD*, Nucl. Phys. B571 (2000) 237–256 [hep-lat/9906013].

[90] C. Alexandrou, E. Follana, H. Panagopoulos and E. Vicari, *One-loop Renormalization of Fermionic Currents with the Overlap-Dirac Operator*, Nucl. Phys. B580 (2000) 394–406 [hep-lat/0002010].

[91] G. Martinelli, C. Pittori, C. T. Sachrajda, M. Testa and A. Vladikas, *A General Method for Nonperturbative Renormalization of Lattice Operators*, Nucl. Phys. B445 (1995) 81–108 [hep-lat/9411010].

[92] QCDSF Collaboration, M. Gürtler *et. al.*, *Non-perturbative Renormalisation for Overlap Fermions*, PoS LAT2005 (2005) 125 [hep-lat/0510045].

[93] R. Sommer, *A New Way to Set the Energy Scale in Lattice Gauge Theories and its Applications to the Static Force and alpha-s in SU(2) Yang-Mills Theory*, Nucl. Phys. B411 (1994) 839–854 [hep-lat/9310022].

[94] S. Necco and R. Sommer, *The N(f) = 0 Heavy Quark Potential from Short to Intermediate Distances*, Nucl. Phys. B622 (2002) 328–346 [hep-lat/0108008].

[95] S. Capitani and L. Giusti, *Perturbative Renormalization of Weak-Hamiltonian Four-Fermion Operators with Overlap Fermions*, Phys. Rev. D62 (2000) 114506 [hep-lat/0007011].

[96] G. P. Lepage and P. B. Mackenzie, *On the Viability of Lattice Perturbation Theory*, Phys. Rev. D48 (1993) 2250–2264 [hep-lat/9209022].

[97] S. Dürr, C. Hoelbling and U. Wenger, *UV-filtered Overlap Fermions*, Proc. Sci. LAT2005 (2005) 144 [hep-lat/0509111].

[98] UKQCD Collaboration, C. R. Allton *et. al.*, *Gauge Invariant Smearing and Matrix Correlators using Wilson Fermions at Beta = 6.2*, Phys. Rev. D47 (1993) 5128–5137 [hep-lat/9303009].

[99] Particle Data Group Collaboration, S. Eidelman *et. al.*, *Review of Particle Physics*, Phys. Lett. B592 (2004) 1.

[100] L. Maiani and M. Testa, *Final State Interactions from Euclidean Correlation Functions*, Phys. Lett. B245 (1990) 585–590.

[101] C. W. Bernard, T. Draper, A. Soni, H. D. Politzer and M. B. Wise, *Application of Chiral Perturbation Theory to $K \to 2$ Pi Decays*, Phys. Rev. D32 (1985) 2343–2347.

[102] R. C. Brower, G. Maturana, M. Belen Gavela and R. Gupta, *Calculation of Weak Transitions in Lattice QCD*, Phys. Rev. Lett. 53 (1984) 1318.

[103] ALPHA Collaboration, P. Dimopoulos *et. al.*, *A Precise Determination of B(K) in Quenched QCD*, hep-ph/0601002.

[104] C. Dawson, *Progress in Kaon Phenomenology from Lattice QCD*, PoS LAT2005 (2005) 007.

[105] M. A. Shifman, A. I. Vainshtein and V. I. Zakharov, *Light Quarks and the Origin of the Delta I = 1/2 Rule in the Nonleptonic Decays of Strange Particles*, Nucl. Phys. B120 (1977) 316.

[106] L. Lellouch and M. Lüscher, *Weak Transition Matrix Elements from Finite-volume Correlation Functions*, Commun. Math. Phys. 219 (2001) 31–44 [hep-lat/0003023].

[107] L. Giusti, P. Hernández, M. Laine, C. Pena, J. Wennekers and H. Wittig, *Correlation Functions at Small Quark Masses with Overlap Fermions*, Nucl. Phys. Proc. Suppl. 140 (2005) 417–419 [hep-lat/0409031].

[108] L. Giusti, P. Hernández, M. Laine, C. Pena, P. Weisz, J. Wennekers and H. Wittig, *On the Determination of Low-energy Constants for Delta(S) = 1 Transitions*, PoS LAT2005 (2005) 344 [hep-lat/0510033].

[109] L. Del Debbio, L. Giusti and C. Pica, *Topological Susceptibility in the SU(3) Gauge Theory*, Phys. Rev. Lett. 94 (2005) 032003 [hep-th/0407052].

[110] P. Dimopoulos, L. Giusti, P. Hernández, F. Palombi, C. Pena, A. Vladikas, J. Wennekers and H. Wittig, *Non-perturbative Renormalization of Left-Left Four-Fermion Operators with Overlap Fermions*, in preparation.

[111] P. Weisz unpublished notes (2002).

[112] L. Giusti, P. Hernández, M. Laine, C. Pena, J. Wennekers and H. Wittig, *On $K \to \pi\pi$ Amplitudes with a Light Charm Quark*, in preparation.

[113] T. Hambye, S. Peris and E. de Rafael, *Delta(I) = 1/2 and epsilon'/epsilon in large-N(c) QCD*, JHEP 05 (2003) 027 [hep-ph/0305104].

[114] L. Giusti, P. Hernández, M. Laine, P. Weisz and H. Wittig, *Low-Energy Couplings of QCD from Topological Zero-Mode Wave Functions*, JHEP 01 (2004) 003 [hep-lat/0312012].

[115] P. Hernández, *Low Energy Couplings from Topological Zero Mode Wave Functions*, . Talk at Lattice 2006, Dublin, unpublished.

[116] N. Cabibbo and E. Marinari, *A New Method for Updating SU(N) Matrices in Computer Simulations of Gauge Theories*, Phys. Lett. B119 (1982) 387–390.

[117] S. L. Adler, *An Overrelaxation Method for the Monte Carlo Evaluation of the Partition Function for Multiquadratic Actions*, Phys. Rev. D23 (1981) 2901.

[118] F. R. Brown and T. J. Woch, *Overrelaxed Heat Bath and Metropolis Algorithms for Accelerating Pure Gauge Monte Carlo Calculations*, Phys. Rev. Lett. 58 (1987) 2394.

[119] M. Creutz, *Overrelaxation and Monte Carlo Simulation*, Phys. Rev. D36 (1987) 515.

[120] I. Montvay and G. Münster, *Quantum Fields on a Lattice*, . Cambridge, UK: Univ. Pr. (1994) 491 p. (Cambridge monographs on mathematical physics).

[121] UKQCD Collaboration, C. R. Allton *et. al.*, *Gauge Invariant Smearing and Matrix Correlators Using Wilson Fermions at Beta = 6.2*, Phys. Rev. D47 (1993) 5128–5137 [hep-lat/9303009].

[122] C. Best *et. al.*, *Pion and Rho Structure Functions from Lattice QCD*, Phys. Rev. D56 (1997) 2743–2754 [hep-lat/9703014].

[123] A. J. Buras and P. H. Weisz, *QCD Nonleading Corrections to Weak Decays in Dimensional Regularization and 't Hooft-Veltman Schemes*, Nucl. Phys. B333 (1990) 66.

[124] S. M. Nishigaki, P. H. Damgaard and T. Wettig, *Smallest Dirac Eigenvalue Distribution from Random Matrix Theory*, Phys. Rev. D58 (1998) 087704 [hep-th/9803007].

[125] P. Weisz unpublished notes (2003).

[126] M. Lüscher, *Lattice QCD with Light Wilson Quarks*, PoS LAT2005 (2005) 002 [hep-lat/0509152].

Acknowledgements

Here I would like to thank some people that helped me in one way or the other over the last few years. I want to thank

- Hartmut for the enjoyable time we have spent working together, for his advice and help,
- the other members of the $K \to \pi\pi$-club: Carlos, Leonardo, Miho, Mikko, Peter, Pilar, Silvia and Yoshiaki for the fruitful collaboration and enthusiastic discussions,
- the computer centres at DESY, FZ Jülich and LRZ München for the possibility to use their resources,
- my colleagues at DESY for the nice and relaxed atmosphere in the theory group,
- my office mates Maik, Markus and Toffi for my daily dose of tea, cookies, Skat and silliness (in ascending order),
- Bernd and Elisabeth for their unconditional support,
- Judith for being wonderful and for preventing my transformation into a weird scientist.